UNIVERSITÄT BONN

Spindown and envelope inflation of massive main sequence stars in the Milky Way

Kaila Nathaniel

Masterarbeit in Astrophysik
angefertigt im Argelander-Institut für Astronomie

vorgelegt der
Mathematisch-Naturwissenschaftlichen Fakultät
der
Rheinischen Friedrich-Wilhelms-Universität Bonn

Mai 2022

I hereby declare that the work presented here was formulated by myself and that no sources or tools other than those cited were used.

Bonn, 12 May, 2022
Date

Kaila Nathaniel
Signature

1. Gutachter: Prof. Dr. Norbert Langer
2. Gutachter: Prof. Dr. Cristiano Porciani

Abstract

Massive stars are powerful cosmic engines, and their strong stellar winds, high luminosities, and violent deaths have been shaping the evolution of the Universe since before the formation of galaxies. Despite their importance, we still lack a complete understanding of their evolution, even on the main sequence. This thesis aims to better understand the process of stellar spindown and the impact of envelope inflation on stellar evolution. We use evolutionary models and population synthesis of single rotating stars at Galactic metallicity to investigate stellar spindown and envelope inflation in massive main sequence stars. We then compare our results to a selection of stars from the IACOB project, a long term spectroscopic study of Galactic OB stars. We find that the most luminous IACOB stars spin down less than our models and their effective temperature distribution is consistent with envelope inflation. We discuss the consequences of our findings for the evolution and fate of massive stars.

Acknowledgements

First and foremost, I would like to thank my advisor, Prof. Dr. Norbert Langer, for his inexhaustible patience and kindness with which he has guided me over the past year, especially in regards to the challenges of completing a thesis in a foreign country in the midst of a pandemic. I have learned much more than stellar physics over the course of this project and the experience has been invaluable.

I am very thankful to the many people I have met at the Argelander Institut für Astronomie, especially those in the stellar group. A special thanks goes to Abel Schootemeijer, Koushik Sen and Ben Hastings for the countless hours they have spent helping me, and to Elisabeth Kramer for her assistance in the many administrative matters that go along with science. My studies would not have been possible without the support of the Bonn-Cologne Graduate School of Physics and Astronomy and I am very grateful for their confidence in me.

The observations from the IACOB project are a key part of this thesis, so I would like to thank its members for both the observational sample and the many fruitful discussions. Hopefully one day we will meet in person!

Last, but certainly not least, I would like to thank my friends and family on both sides of the Atlantic for their endless support. I would especially like to thank my Gramps, Dr. Hugh R. Rugge, whose own career in space science inspired me to pursue this path. I would not have ended up in Germany without the lucky twist of fate that put Casey and I together as random roommates our freshman year at Virginia Tech, and I am forever grateful for her friendship. Ich habe viel Liebe für die Freunde, die ich in Deutschland gewonnen habe und die diese vergangenen Jahre zu einem wunderbaren Abenteuer gemacht haben.

Chapter 1

Introduction

1.1 Motivation

Massive stars are extraordinary objects. With their large luminosities, strong winds, and spectacular explosions they heat up and enrich surrounding gas clouds (Burbidge et al., 1957; Chiappini et al., 2011; Kasen et al., 2017), trigger star formation (Crowther, 2019; Gritschneder et al., 2006; Mac Low and Klessen, 2004), and drive the chemical evolution of galaxies (de Rossi et al., 2010; Kajino et al., 2019; Pignatari et al., 2010; Thielemann et al., 2011). Massive stars are even thought to have played a role in reionizing the universe before galaxies existed (Bromm et al., 2009), making them a crucial building block of the universe as we know it. When massive stars explode they produce supernovae (Burrows and Vartanyan, 2021; Burrows et al., 1995), neutron stars (Baym et al., 2018; Heger et al., 2003), and black holes (Celotti et al., 1999; Miller-Jones et al., 2021; Remillard and McClintock, 2006; Webster and Murdin, 1972); which can then merge in dramatic collisions, producing gravitational waves (Abbott et al., 2017, 2019, n.d.; Abbott et al., 2021). Massive stars are not common, however, and make up a relatively small proportion of any given stellar population, e.g., only one $50\,M_\odot$ star is born for every $\sim$10 000 $1\,M_\odot$ stars (Salpeter, 1955). In addition, massive stars have lifespans of only $\sim$1 Myr to $\sim$10 Myr, while a $1\,M_\odot$ star can live for over 10 billion years. Though rare and short-lived, massive stars have an outsize impact on our universe.

Despite their importance, we still do not have a full understanding of how massive stars evolve, even on the main sequence, which comprises $\sim$90 % of a star's life. We know that processes such as mass loss, rotation, convection, mixing, and the internal transport of energy and angular momentum play a vital role in stellar evolution, but we do not fully know how they work. We study these processes by modeling them with stellar evolution codes and comparing our results with observations.

In particular, rotation and internal energy transport can have a critical effect on a star's evolution, from the very beginning to the formation of stellar end products (Langer, 2012). This thesis focuses on spindown, i.e., the process by which stars slow their rotation rate, and envelope inflation, which is tied to the efficiency of internal energy transport.

A star's rotation rate can affect its evolution as strongly as its initial mass and

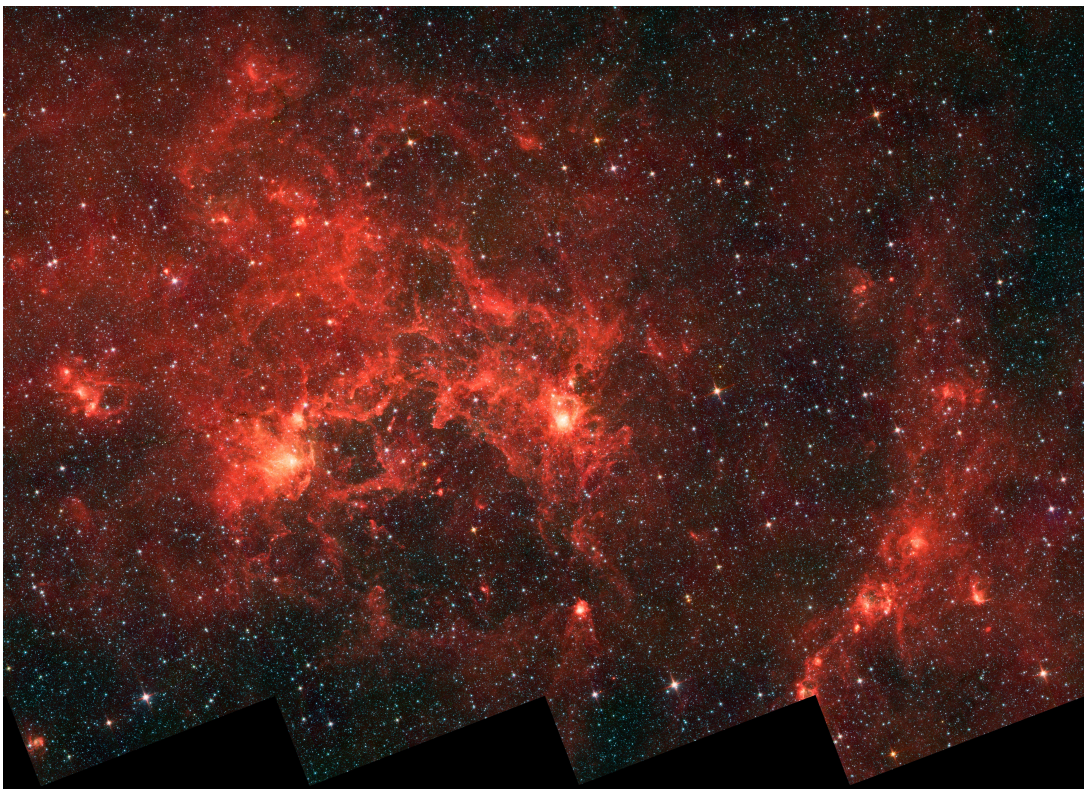

Figure 1.1: An infrared image of the Dragonfish nebula in the Milky Way, taken with the NASA Spitzer Space Telescope (Benjamin et al., 2003). This massive star-forming region is home to some of the most luminous OB-type stars in our galaxy. Credit: NASA, JPL-Caltech, University of Toronto

metallicity (Meynet and Maeder, 2000). Stars can develop instabilities as a result of rotation, which can then transport quantities such as matter, energy, and angular momentum. Rotationally induced mixing changes the chemical composition of a star, and in extreme cases can lead to chemically homogeneous evolution (Martins et al., 2013), which changes a star's luminosity, temperature, and evolutionary channel. Energy transport moves the energy generated in the inner regions of the star to the outer layers, keeping the star in hydrostatic and radiative equilibrium. Angular momentum transport keeps stars rigidly rotating and prevents the stellar core from reaching critical rotation and flying apart (Langer, 2012). Studying how a star spins down can help us understand all these processes and more.

Spindown, however, is not just a useful probe for other stellar processes. We can use knowledge of spindown to estimate initial rotation rates, as well as the likelihood of past events in stars' history changing the spin rate. Spindown also helps us look ahead and see how a star will evolve through the MS, TAMS, and post-supernova. Knowing how rapidly a star is spinning before core-collapse helps us to constrain the

rotation rate of the resulting compact object.

Envelope inflation has similarly wide-ranging consequences. If a star's radiative pressure force becomes greater than its gravitational force, and it cannot efficiently transport energy to the surface, its outer layers will inflate to form a huge, low density envelope. This can affect the star's temperature, rotation rate, mass loss rate, and more (Sanyal et al., 2015, 2017). Characterizing how and when stars inflate helps us to constrain the extent of the main sequence in the Hertzsprung-Russell diagram, a crucial tool for understanding stellar evolution. Envelope inflation could also help us settle long-standing questions about the cause of the discrepancies in radii between observed and modeled Wolf-Rayet and Luminous Blue Variable star (Gräfener et al., 2012).

We study spindown and envelope inflation with evolutionary models and population synthesis. We first describe the physics behind these processes, the assumptions made in our models, and our implementation of population synthesis. We then compare our results to a sample of observed stars from the IACOB project and discuss our findings and their implications.

1.2 Evolution of massive stars

We use the Hertzsprung-Russell, or HR, diagram when discussing the evolution of stars. This diagram was developed independently by both Ejnar Hertzsprung and Henry Russell in the early 1900s (Hertzsprung, 1911; Russell, 1914), after which Sir Arthur Eddington quickly realized that it could be used to represent the stellar life cycle (Eddington, 1920). The HR diagram shows the relationship between luminosity and effective temperature of a star, which means each stellar evolutionary stage occupies a distinct region. Stars cool as they age, so effective temperature increases from right to left to keep the passage of time running left to right. Luminosity has the usual behavior and increases from bottom to top.

Another version of this diagram uses the spectroscopic luminosity, which is defined as

$$\mathcal{L} = \frac{1}{4\pi\sigma G}\frac{L}{M} = \frac{{T_{\rm eff}}^4}{g}, \tag{1.1}$$

with G as the gravitational constant, σ as the Stefan-Boltzmann constant, L as the bolometric luminosity, M as the mass, $T_{\rm eff}$ as the effective temperature and g as the stellar surface gravity. This spectroscopic HR diagram is a useful tool for investigating observed stars, as it is distance and reddening independent, both of which can be difficult to constrain. Due to the fact that the spectroscopic luminosity is proportional to the luminosity-to-mass ratio, there is a maximum possible value. For Galactic composition stars, this limit is $\log(\mathcal{L}/\mathcal{L}_\odot) = 4.6$ (Langer and Kudritzki,

2014). We use the spectroscopic HR diagram in this thesis because our sample of observed stars does not currently have reliable distance measurements (Holgado et al., 2020).

The lifecycle of a massive star can be summarized as follows. A star is formed when a molecular cloud collapses and its core reaches a high enough temperature to ignite hydrogen. This point is called the zero-age main sequence (ZAMS) and marks the beginning of the main sequence (MS). The MS continues until the hydrogen core has been completely burnt to helium, known as the terminal-age main sequence (TAMS). The star then undergoes gravitational contraction to raise the core temperature so that the hydrogen shell around the helium core can ignite. While this is going on, the stellar surface is cooling and the envelope is expanding. When the star completes hydrogen shell burning, it begins to burn the helium core. This cycle of core and shell burning continues with the CNO-cycle, silicon, and finally iron. Nuclear fusion stops when the star has an iron core and after a short period of contraction it explodes in a supernova (Pols, 2011).

Chapter 2

Theoretical background

2.1 Convective energy transport

Convection is a stellar mixing process between hotter and cooler layers, in a star or elsewhere, by "blobs" of material moving in a dynamically unstable region. The process requires a temperature gradient and thusly depends on buoyancy forces, e.g., hotter blobs are less dense and rise, while cooler blobs are denser and descend.

The stability of a layer against convection depends on the radiative and adiabatic temperature gradients. The radiative temperature gradient is defined as

$$\nabla_{\mathrm{rad}} = \frac{3}{16\pi acG}\frac{\kappa l P}{m T^4}, \tag{2.1}$$

where a is the radiation constant, c is the speed of light, G is the gravitational constant, κ is the opacity, l is the luminosity, P is the pressure, m is the mass coordinate, and T is the temperature. In simple terms, the radiative temperature gradient is the rate of temperature change as a function of depth, which is expressed as pressure in this equation.

The adiabatic temperature gradient can be written as

$$\nabla_{\mathrm{ad}} = \frac{P}{\rho T c_P}\frac{\chi_{\mathrm{T}}}{\chi_\rho}, \tag{2.2}$$

where c_P is the specific heat with constant pressure and χ_{T} and χ_ρ are defined as

$$\chi_{\mathrm{T}} = \frac{T}{P}\left(\frac{\partial P}{\partial T}\right)_{\rho,X_i} \qquad \chi_\rho = \frac{\rho}{P}\left(\frac{\partial P}{\partial \rho}\right)_{T,X_i}, \tag{2.3}$$

respectively (Pols, 2011). The X_i subscripts mean that composition is held constant.

The adiabatic temperature gradient represents the rate of temperature change in an adiabatic blob due to pressure, meaning blobs do not exchange any heat with their surroundings. For massive MS stars, the adiabatic temperature gradient can have a

value between 0.25 for a radiation pressure dominated gas and 0.4 for a gas pressure dominated gas (Kippenhahn and Weigert, 1990).

In order for a layer to be stable against convection, its adiabatic temperature gradient must be greater than its radiative temperature gradient. In other words, blobs follow the steeper temperature gradient, and if that gradient allows them to rise and fall without exchanging heat, then they will do so and the layer will not become convective. This can be shortened to the Schwarzschild criterion,

$$\nabla_{\rm rad} < \nabla_{\rm ad}. \tag{2.4}$$

The Schwarzschild criteria is only valid in layers that do not have a mean molecular weight gradient ∇_μ, i.e., chemically homogeneous layers. For layers in which the mean molecular weight gradient does not equal zero, there is the Ledoux criteria,

$$\nabla_{\rm rad} < \nabla_{\rm ad} - \frac{\chi_\mu}{\chi_T}\nabla_\mu, \tag{2.5}$$

where $\chi_\mu = (\partial \log P/\partial \log \mu)_{\rho,\rm T}$ and μ is the mean molecular weight.

2.1.1 Mixing length theory

The Schwarzschild and Ledoux criteria state the conditions that must be violated for a layer to be convective, but the question of how convection occurs still remains. Answering this question fully requires a detailed theory of convection, which is an active research area in astrophysics. While it is possible to simulate stellar convection with three-dimensional hydrodynamic codes, it is extremely complex and computationally expensive, and thus is currently not included in standard calculations of stellar evolution (Lamers et al., 2017). We approximate convection with the one-dimensional mixing length theory (MLT).

In the MLT, the buoyancy forces in dynamically unstable layers cause blobs to moving radially. Blobs move until they have traveled a distance ℓ, at which point they dissolve and either release their excess heat or absorb their heat deficit, becoming an indistinguishable part of their environment (Kippenhahn and Weigert, 1990). Due to the density of stellar interiors, this process can be a very efficient method of heat transfer and can also contribute to the dredge-up of nuclear burning products (Pols, 2011).

There is not a known process to calculate ℓ, but it is assumed to be on the order of the pressure scale height $\lambda_{\rm P}$ and so can be defined as the pressure scale height multiplied by a constant,

$$\ell \equiv \alpha_{\rm MLT}\, \lambda_{\rm P}, \quad \lambda_{\rm P} = \frac{P}{\rho g}, \tag{2.6}$$

with $\alpha_{\rm MLT}$ as the constant, P as pressure, ρ as density, g as gravity. The pressure scale height is the radial height over which the pressure changes by a factor of e. This assumption is based on the fact that rising gas blobs expand and therefore if a convective region is evenly split between rising and descending blobs, the rising blobs will begin to cover most of the surface area of the layer after rising over one or two times the pressure scale height (Pols, 2011).

2.2 Inflation

A star's maximum luminosity is known as the Eddington luminosity and it is the luminosity at which the outward radiation pressure force is exactly balanced with the inward gravitational force. It is defined as

$$L_{\rm Edd} = \frac{4\pi GMc}{\kappa}, \tag{2.7}$$

with κ as the opacity. If we only consider opacity due to e^- scattering, we can take κ as $\kappa_{\rm e}$, which is defined as

$$\kappa_{\rm e} = 0.2(1+X)\ {\rm cm}^2\, {\rm g}^{-1}, \tag{2.8}$$

where X is the surface mass fraction of hydrogen. The Eddington luminosity is usually expressed in terms of the Eddington factor,

$$\Gamma_{\rm Edd} = \frac{L}{L_{\rm Edd}} < 1. \tag{2.9}$$

A star reaches the Eddington limit when its Eddington factor equals one. Using e^- scattering as the sole source of opacity is a common approximation to make, as $\kappa_{\rm e}$ is usually the dominant source of opacity in massive stellar envelopes. This approximation fails, however, when we consider inflation. Other sources of opacity begin to have a non-negligible impact when a star is near the Eddington limit, especially those dependent on metallicity. At a temperature of $\sim 2 \times 10^5\,{\rm K}$, the stellar envelope is only partially ionized, meaning that the bound-bound and bound-free transitions of iron-group elements cause an opacity peak, typically known as the Fe-bump (Iglesias and Rogers, 1996). The Fe-bump causes the most opacity enhancement, but hydrogen recombination and helium ionization also contribute via their own opacity bumps (Sanyal et al., 2015). There is currently no analytic

method to find the total opacity including these enhancements, but the OPAL project (Iglesias and Rogers, 1996) provides tables of Rosseland mean opacity values, which are widely used instead.

These additions to the opacity lower the Eddington luminosity, making it easier for stars to reach the Eddington limit. Kato (1986) found that it is still possible for stars to reach the Eddington limit using only e^- scattering opacity, but stars with metallicities similar to those considered in this thesis require a minimum mass of $\sim 10^6\,M_\odot$, which is far outside the mass range considered here.

When a star's Eddington factor exceeds 1, it is no longer in hydrostatic equilibrium, i.e., the gravitational and radiative pressure forces are no longer balanced. If this occurs at the surface of the star, then the radiation pressure force will just blow material into space. Inside the envelope, however, the radiative pressure force pushes against the layers above it. In order to restore the balance, the star must either decrease L or increase L_{Edd}. Stellar envelopes have low densities, causing convective energy transport to be inefficient, which makes any meaningful decrease of L unlikely. Instead, the stellar envelope begins to inflate, as the radiative pressure force is now greater than the gravitational force. This expansion decreases the density and hence opacity, increasing the Eddington luminosity (Sanyal et al., 2015). This process continues until the Eddington luminosity is large enough that the star's Eddington factor is below one, at which point the star is again in hydrostatic equilibrium.

We can challenge our assumption of inefficient convective energy transport, however, by considering the MLT. As discussed in Section 2.1.1, the mixing length determines the distance a convective blob of gas can travel before dissolving and either releasing or absorbing energy. A longer mixing length means that the energy flux can travel a greater distance, resulting in more efficient transportation of convective energy. This brings more energy to the surface of the star, reducing the radiative pressure force. It also means that stars with a greater mixing length are hotter at a given luminosity. The opacity bumps from Fe, H, and He are dependent on temperature, so a high temperature in the envelope minimizes their contribution. The end result is that stars with a longer mixing length are less likely to reach the Eddington limit and inflate their envelopes.

2.3 Spindown

As discussed in the introduction, star formation starts when a molecular cloud reaches the Jeans mass and collapses under its own gravity. Conservation of angular momentum causes the net rotation, however small, to increase as the cloud collapses, forming a rotating accretion disk (Pols, 2011). Thus, all stars are born spinning and can be approximated as rigid rotators, at least while on the MS (Maeder and Meynet, 2005). As stars evolve, however, mass loss causes them to spin down. Depending on

a star's evolutionary stage, mass, and multiplicity, it can lose mass via stellar winds, mass transfer, and mass ejection events. This thesis focuses on single stars, which mainly lose mass via radiation-driven stellar winds.

If a star is sufficiently hot and luminous, radiation pressure will induce an outward acceleration on ionized atoms (Pols, 2011). This stellar wind strips material off the star, causing it to lose both mass and angular momentum, defined as $J = I\omega$, with I as the moment of inertia and ω as the angular velocity. Less mass means the gravitational force is weaker, so the star expands its surface layers in order to keep hydrostatic equilibrium. Local conservation of angular momentum causes these expanded layers to spin down, i.e., the star is differentially rotating. Angular momentum transport reestablishes rigid rotation, slowing down the core and speeding up the outer layers. The total amount of angular momentum has decreased, however, so the star's new angular velocity is lower. While stellar winds can induce mass loss rates as high as $10^{-5}\,\mathrm{M}_\odot\,\mathrm{yr}^{-1}$ (Lamers et al., 2017), the dominant effect is angular momentum loss, due to the fact that $\dot{J}/J$ is an order of magnitude greater than $\dot{M}/M$ (Langer, 1998).

This is a highly simplified picture, as phenomena such as turbulence, magnetic fields, and surface inhomogeneities can all impact spindown. However, we limit ourselves to the discussion of angular momentum transport, as a detailed explanation of all these phenomena is outside the scope of this thesis. There are several different mechanisms that can transport angular momentum inside a star, including Eddington-Sweet circulation currents, shear mixing, pulsations, and magnetic torques. While all these processes contribute to angular momentum transport, the last is the most efficient and therefore dominant.

Magnetic torques transport angular momentum via a process known as the Tayler-Spruit dynamo, which is the result of differential rotation inside a star. If a star's angular velocity profile is not constant, it can develop instabilities in its magnetic field, which cause blobs of material to be displaced inside the star. Magnetic torques displace the blobs both vertically and horizontally, transporting angular momentum out of the more rapidly rotating core into the slower outer layers of the star. The end result is a star that is again rigidly rotating with a constant angular velocity profile that is lower than before the introduction of instabilities (Spruit, 1999, 2002).

Chapter 3

Methods

3.1 Stellar models

In this thesis we use the Galactic single star evolutionary models created by Brott et al. (2011), in addition to calculating a new grid of models in order to test the effect of varying the mixing length. Both grids were calculated with one-dimensional stellar codes and the same physics assumptions. Brott et al. (2011) grid (hereby known as the Brott grid) was calculated with the stellar code described in Heger et al. (2000), Petrovic et al. (2005), and Yoon and Langer (2005), while we used the stellar code MESA (Paxton et al., 2011, 2013, 2015, 2018, 2019), version r8845, for the new models. MESA is an open-source, one-dimensional stellar code that has been in active development since 2007. We utilized input, composition, and nuclear network files from Marchant (2016a,b), which calculates MESA models with the same physics assumptions as the Brott grid, with some small changes to composition.

The major physics assumptions are as follows. Mixing and angular momentum transport are treated as diffusive processes. Convection uses the standard MLT as described by Cox and Giuli (1968) and is modeled with the Ledoux criterion. Semi-convection is included as in Langer et al. (1983) using an efficiency parameter of $\alpha_{\rm SEM} = 1$.

Due to magnetic fields, the stars keep near rigid rotation while on the MS, which suppresses shear mixing between layers. Mass loss due to stellar winds is calculated according to the prescriptions of Vink et al. (2000, 2001), which is based on the method described by Koter et al. (1997), as well as the recipes from Hamann et al. (1995) and Nieuwenhuijzen and de Jager (1990). These two prescriptions predict strong mass loss at the bi-stability jumps found at $T_{\rm eff} \sim 22\,{\rm kk}$ and $T_{\rm eff} \sim 12.5\,{\rm kk}$. The overshooting parameter is calibrated using data from the VLT-FLAMES Survey of Massive Stars (Evans et al., 2005) and set at $\alpha = 0.335$.

Rapid rotation can deform stars, causing deviations from spherical symmetry. In order to account for this three-dimensional effect with one-dimensional stellar codes, the stellar structure equations and stellar properties are calculated on isobaric mass shells. This enforces the shellular approximation, which assumes that the angular velocity is constant on isobaric surfaces, which then correspond with mass shells. We use the methods of Endal and Sofia (1976) and Kippenhahn and Thomas (1970) for

the effect of centrifugal acceleration. The critical velocity is calculated as

$$v_{\text{crit}} = \sqrt{\frac{GM}{r}\,(1 - \Gamma_{\text{Edd}})}, \tag{3.1}$$

The Brott grid chemical composition was tailored to the Galactic sample of the FLAMES survey (Evans et al., 2005) using the standard OPAL project (Iglesias and Rogers, 1996) opacity tables. We set the MESA grid chemical composition according to the Brott grid, but used custom opacity tables from the OPAL project instead of the standard tables. The initial mass fractions for both grids are in Table 3.1.

Table 3.1: The initial mass fractions of hydrogen (X), helium (Y), and metals (Z) in both stellar grids.

Grid	X_i	Y_i	Z_i
Brott grid	0.7274	0.2638	0.0088
MESA grid	0.7256	0.2651	0.0092

The beginning of the MS is defined as when a star's hydrogen core ignites. While real stars move smoothly from the protostar phase to the ZAMS, stellar models undergo a numerical process known as a "relaxation loop," which is when the software adjusts its initial prediction of the stellar structure in order to reach hydrostatic equilibrium. These adjustments can alter the values of parameters such as effective temperature, luminosity, and rotation rate. We exclude relaxation loop data from our analysis by defining the ZAMS as when 5 % of the initial core hydrogen mass fraction has been burned.

During the MS, a star gets cooler and more luminous, moving up and to the right across the HR diagram. The MS ends when a star has finished burning through the hydrogen in the stellar core. Without the radiation pressure from nuclear fusion, the gravitational force causes the star to contract until the core temperature rises enough to ignite the now helium core (Pols, 2011). This makes the star reverse direction on the HR diagram as it heats up due to contraction. When the core is hot enough to ignite helium contractions stops and the star reverses on the HR diagram again and repeats the process of slowly cooling as it burns helium. The initial turnback point at the end of core hydrogen burning, called the MS hook, can be used to mark the end of the MS. For stellar models of 35 $\mathrm{M}_\odot$ and below, this is the point we chose as the TAMS.

However, this MS hook is not present in all the stellar models. Models above 35 $\mathrm{M}_\odot$ do not show a clear MS hook. Higher mass stars lose mass much more rapidly while on the MS and lose their envelopes before completing hydrogen core burning. Once the envelope has been stripped, the hot inner layers of the star are at the surface and the star turns around on the HR diagram before the end of the MS. The star still

undergoes core contraction when it finishes hydrogen core burning, but as the star has already turned around on the MS, it just moves further to the left. For stars like these, without a clear MS hook, we set the TAMS as the point at which the mass fraction of core hydrogen drops to 0.03.

The Brott grid has an initial mass range from $3\,M_\odot$ to $100\,M_\odot$, with initial equatorial rotational velocities ranging from $0\,km\,s^{-1}$ to $550\,km\,s^{-1}$. Our new MESA grid has an initial mass range from $12\,M_\odot$ to $200\,M_\odot$ and an initial equatorial velocity of $150\,km\,s^{-1}$. We set the mixing length parameter α_{MLT} to 0.5, 1.5, and 5.0.

3.1.1 Angular momentum loss

The Brott models calculate angular momentum loss from stellar winds by integrating the specific angular momentum profile, $j(m)$, from the surface to the amount of mass lost (dm). This is calculated as

$$dJ = \int_{M_* - dm}^{M_*} j(m)\, dm. \tag{3.2}$$

The specific angular momentum profile decreases monotonically inwards for rigidly rotating stars, so inner layers have less specific angular momentum than layers at the surface. The problem becomes clear when we remember that real stars are continuously adjusting and do not evolve in discrete steps. If we remove a small amount of angular momentum from the surface of a star, it will immediately readjust so that its angular momentum profile and radius remains nearly the same (Langer, 1998). Therefore, calculating dJ by integrating over $j(m)$ may underestimate the angular momentum lost.

A more accurate approximation assumes that the model's readjustment time scale is shorter than the assumed time interval between models and thus only considers the value of the specific angular momentum at the surface of the star. The amount of angular momentum lost is calculated simply as the surface specific angular momentum, j_{surf}, multiplied by the mass loss rate and integrated over the time interval,

$$dJ = \int_{t}^{t+dt} j_{surf}\, \dot{M} dt. \tag{3.3}$$

This approach assumes that mass loss is independent of latitude and that j_{surf} is averaged over the latitude (Heger et al., 2000). We can see the difference between the two angular momentum loss prescriptions in Figure 3.1, which illustrates the amount of angular momentum removed by both prescriptions. If the amount of mass lost is tiny enough, corresponding to an infinitesimally small change in radius, the two prescriptions will remove the same amount of angular momentum. If the

change in radius is not infinitesimally small, however, then the prescription originally implemented in the Brott grid will underestimate the amount of angular momentum to remove.

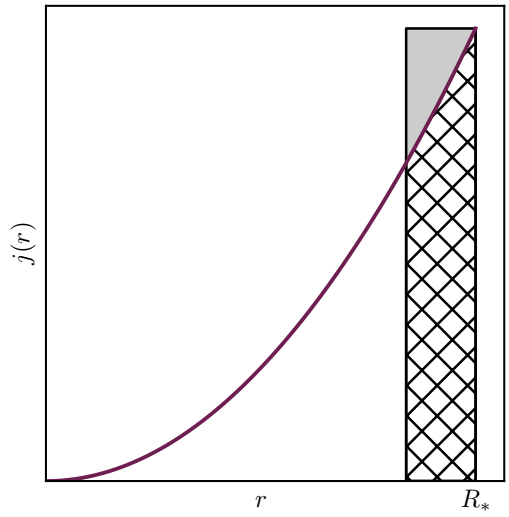

Figure 3.1: A schematic diagram of a model's specific angular momentum profile as a function of radius, illustrating the original and corrected angular momentum loss prescriptions. The width of the hatched rectangle shows the change in radius caused by removing mass from the model. The prescription implemented in the Brott grid removes the angular momentum represented by the hatched area. The new prescription removes the hatched area and the shaded area.

As discussed in Section 2.3, angular momentum loss has a strong impact on spindown, i.e., the prescription used impacts more than just angular momentum. We used the new prescription to recalculate the rate of angular momentum loss in the Brott grid and used the results to compute corrected values for J, $j_{\rm surf}$, and $v_{\rm rot}$ (Hastings, 2021).

3.2 Population synthesis

Population synthesis is a method of modeling large populations of stars. Hydrodynamic stellar codes can also be used to model several hundreds of thousands of stars, but the process is computationally expensive and requires large amounts of digital storage space. Population synthesis uses the results from hydrodynamic codes to generate large populations cheaply with much less storage overhead. This method works by interpolating between previously generated evolutionary models, thereby skipping over the computationally expensive step of calculating the stellar structure equations.

We developed the population synthesis algorithm Hōkū (the Hawaiian word for *star*) in order to study the statistical properties of MS single stars given a specified initial mass function (IMF), initial rotational velocity (or velocity distribution), and star formation rate (SFR).

Using a designated grid of evolutionary stellar models, Hōkū interpolates simulated stars with an initial mass (m_i), rotational velocity at the ZAMS ($v_{\rm ZAMS}$), and age

(τ_*) taken from the appropriate probability distribution functions (PDFs). Each simulated star is calculated from these initial parameters, (m_i, $v_{\rm ZAMS}$, τ_*), which Hōkū uses to select four evolutionary tracks from the model grid. These tracks are then used to interpolate the desired stellar parameters using a three-dimensional linear interpolation algorithm.

For any given simulated star, Hōkū works as follows. First, it takes m_i and determines the two closest masses above and below in the model grid. Next, for each of the two masses, the program finds the two models with ZAMS velocities just above and below $v_{\rm ZAMS}$. These four selected evolutionary tracks will be used to interpolate the simulated star's parameters. As discussed in Section 3.1, a model's velocity can change between the simulation beginning and the chosen ZAMS point, which is why Hōkū uses ZAMS velocities, rather than initial. This change in velocity also means that the model with the lower initial mass may not have the same ZAMS velocity as the model with the higher initial mass, even if they have the same initial velocity. For this reason, Hōkū interpolates first in velocity and then in mass.

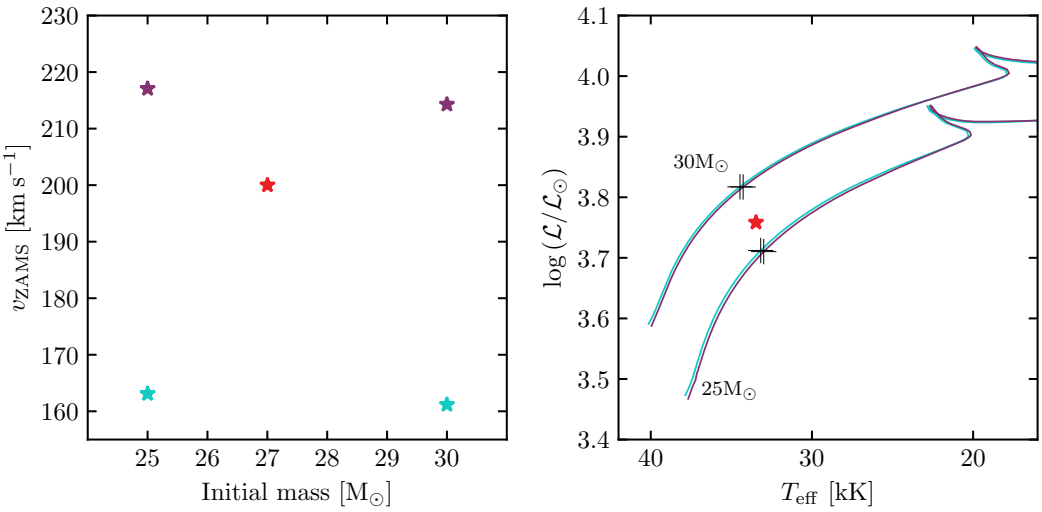

Figure 3.2: Visual representation of the interpolation process using the Brott grid. The left panel shows the initial masses and ZAMS velocities of four grid models, along with the initial mass and ZAMS velocity of the simulated star. Turquoise indicates the models with the lower ZAMS velocity, purple indicates the models with the higher ZAMS velocity, and red marks the interpolated data. The right panel shows the evolution of the four grid models and the location of the simulated star in the spectroscopic HR diagram. The black plus signs mark the points that were used for the interpolation. The interpolated data is in Table 3.2.

A star's MS lifetime is dependent on its initial mass and velocity, meaning that two stars of the same age but with different initial parameters can be in very different evolutionary stages. This fact means we cannot use τ_* in years as our time

interpolation variable. Instead, we use the fractional MS age, which is the current age in years divided by years spent on the MS. For the simulated star, Hōkū interpolates an expected MS lifetime, $\tau_{\rm MS}$, from the MS lifetimes of the model stars and uses this to compute $f_{\rm MS} = \tau_*/\tau_{\rm MS}$.

Hōkū can now interpolate the simulated star's stellar parameters from the four chosen model stars. This process is then repeated for every set of $(m_i,\ v_{\rm ZAMS}, \tau_*)$. If, however, a simulated star's $f_{\rm MS}$ is greater than one, it is thrown out and Hōkū moves to the next initial parameter set. This is why a flat IMF and continuous SFR still results in a population biased towards young, low-mass simulated stars. Figure 3.2 shows a visual representation of this process and Table 3.2 has the resulting interpolated data. With slight adjustment, Hōkū can also calculate evolutionary tracks at a given m_i and $v_{\rm ZAMS}$, as seen in Figure 3.3; or isochrones at a given τ_*, as seen in Figure A.1.

Table 3.2: Data from in Figure 3.2. The initial mass, $v_{\rm ZAMS}$, and age from the *Interpolated* row are taken from distribution functions and the $T_{\rm eff}$, $\log(\mathcal{L}/\mathcal{L}_\odot)$, and $\tau_{\rm MS}$ values are interpolated.

Model	M_i [$\mathrm{M}_\odot$]	$v_{\rm ZAMS}$ [$\mathrm{km\,s^{-1}}$]	τ_* [Myr]	$\tau_{\rm MS}$ [Myr]	$T_{\rm eff}$ [kK]	$\mathcal{L}$ [$\mathcal{L}_\odot$]
Grid	25	163	4.75	6.77	33.2	$10^{3.71}$
	25	217	4.80	6.84	33.0	$10^{3.71}$
	30	161	4.01	5.72	34.5	$10^{3.82}$
	30	214	4.08	5.79	34.3	$10^{3.82}$
Interpolated	27	200	4.46	6.35	33.5	$10^{3.76}$

3.2.1 Initial distribution functions

Hōkū uses a flat initial mass function (IMF) and assumes continuous star formation. Each simulated star also has an inclination angle, which is taken from a PDF that assumes random orientation in space. The velocity distribution function is described below.

We derived a velocity distribution function by fitting a double Gaussian to the observed projected rotational velocity distribution of observed stars seen in Figure 4.2. First, we fit a Gaussian, $G_{\rm fast}$, to the peak at the higher $v \sin i$ value. We then removed all stars to the right of the Gaussian's mean value, $\mu_{\rm fast}$, and subtracted an equal number from the data to the left of $\mu_{\rm fast}$, assuming both symmetry and that all stars to the right of $\mu_{\rm fast}$ are part of $G_{\rm fast}$. We used this revised data, assumed to be free of any contribution from $G_{\rm fast}$, to fit the second Gaussian to the peak at the slower $v \sin i$ value, $G_{\rm slow}$. We added the two Gaussians together to form a single function, shown in Figure 5.3. The velocities output by this function still contain a projection

factor, so as a final step Hōkū divides the output velocity by $\sin i$, with i as the inclination angle, and takes that as the simulated star's v_{ZAMS} value.

3.2.2 Synthetic populations

We used Hōkū to generate synthetic populations of hundreds of thousands of massive MS single stars. We used the populations interpolated from the Brott grid to study spindown and the populations interpolated from the MESA grid to study envelope inflation.

Hōkū interpolated two synthetic populations from the Brott grid. Both have a mass range from $3\,\mathrm{M}_\odot$ to $100\,\mathrm{M}_\odot$ (the full mass range of the grid). One of the populations has a single initial velocity, $v_{\mathrm{ZAMS}} = 200\,\mathrm{km\,s^{-1}}$, and the other uses the velocity distribution function described in Section 3.2.1. We refer to the population with $v_{\mathrm{ZAMS}} = 200\,\mathrm{km\,s^{-1}}$ as the Brott single v_{ZAMS} population and the population with the v_{ZAMS} distribution as the Brott distributed v_{ZAMS} population.

We used the MESA grid to interpolate three synthetic populations, one for each of the different mixing length parameter values. We refer to these α_{MLT} populations individually as the $\alpha_{0.5}$, $\alpha_{1.5}$, and $\alpha_{5.0}$ populations, respectively. Hōkū interpolated them in mass from $12\,\mathrm{M}_\odot$ to $200\,\mathrm{M}_\odot$. The MESA grid has a single initial rotational velocity of $v_i = 150\,\mathrm{km\,s^{-1}}$, so this is also the initial rotational rate of the simulated stars.

3.3 Probability density functions and bias factors of observed stars

Comparing distributions of observables for simulated stars is easy, as we can just look for simulated stars with the desired parameters or location on the HR diagram. Our populations are large enough that any reasonable selection criteria will still result in a sample of thousands. For observed stars, however, we do not know their central abundances, and uncertainties mean we can only ever estimate their location on the HR diagram. While selecting simulated stars requires only the ability to sift through data, observed stars require a little more effort.

We can still construct distributions for chosen areas of the HR diagram, but rather than selecting a subset of the stars in our sample, we use the entire sample and weight each star's contribution by the probability that it is located in the chosen area. We do this by computing a PDF for each star in the sample, using a normalized multivariate Gaussian over an effective temperature range of 7.5 kK to 53 kK and a spectroscopic luminosity range of $10^{2.2}\mathcal{L}_\odot$ to $10^{4.6}\mathcal{L}_\odot$. Integrating a star's PDF over an arbitrary shape on the spectroscopic HR diagram will give the probability that the star is located in that shape. We can also combine the individual PDFs to get a

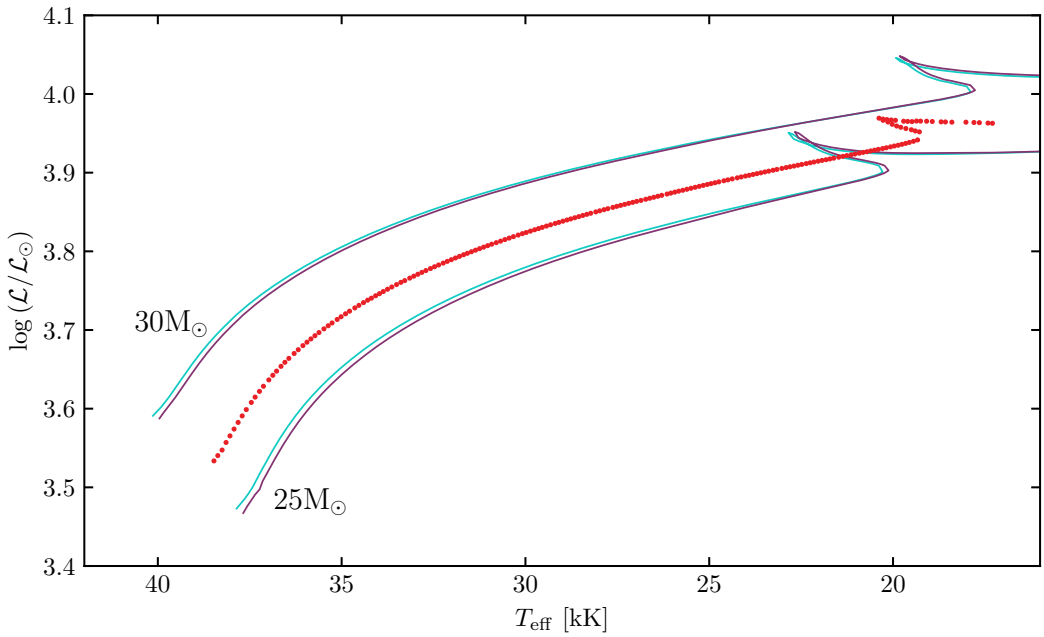

Figure 3.3: An evolutionary track of a $27\,M_\odot$, $v_{ZAMS} = 200\,km\,s^{-1}$ star interpolated with Hōkū using the Brott grid, shown in the spectroscopic HR diagram. This interpolated track was allowed to evolve past the TAMS. As in Figure 3.2, the turquoise marks the tracks with the lower ZAMS velocity and purple marks the tracks with higher ZAMS velocity. The red dotted line is the simulated star.

PDF for the sample as a whole, which can show us at which effective temperatures and spectroscopic luminosities our stars are concentrated.

While every star is considered when constructing distributions, the size of any given star's contribution will vary based on its weighting factor. Summing the unnormalized distribution therefore gives a number, not necessarily an integer, to which the data can be considered equivalent. E.g., a distribution that sums to 10 could be made up of 5 stars that all have a 20 % probability of being found in the chosen area, or 100 stars that each have a 10 % chance of being found in the area.

While our PDF method takes uncertainties into account, observational bias can still affect our analysis. Our simulated star populations cover the whole MS, while the observed sample has gaps. We cannot remove the gaps, but we can attempt to compensate for them by assuming that the bias is locally consistent. If this assumption holds, then a bias factor calculated from data in one area of the spectroscopic HR diagram should give consistent results when applied to data from a nearby area.

We calculate the bias factor by first plotting the distributions of effective temperature at a fixed spectroscopic luminosity range for both the observed and simulated stars.

We take the ratio between the two distributions as the bias factor. We then plot the distributions of effective temperature for another fixed spectroscopic luminosity range and multiply the simulated stars' distribution by the bias factor. If the bias is consistent, then this altered distribution is a valid comparison to the distribution of observed stars.

Chapter 4

The IACOB project

The IACOB project[1] (P.I. Simón-Díaz, Spain) is an ambitious, long term observational project at the Instituto de Astrofísica de Canarias (IAC) in Tenerife, Spain with a goal of compiling a large, homogeneous database of high-resolution, multi-epoch spectra of Galactic OB stars. The overall project objective is to create a comprehensive empirical characterization of the physical properties of a statistically significant sample of OB stars with the expectation that such information will give new insights into theories of stellar atmospheres, winds, interiors, and massive star evolution. The database currently contains spectra for over 1000 Galactic O- and B-type stars up to B = 9 mag. These spectra provide new estimates on stellar wind parameters, rotational velocities, and abundances, as well as information on phenomena that can affect the spectra, such as binarity/multiplicity, pulsations, rotational modulation, and wind variability (Simón-Díaz et al., 2011, 2020).

The IACOB project initially focused on stars observable from the Northern Hemisphere, but in 2012 they established a collaboration with the OWN (Barbá et al., 2017) project, which is a high-resolution spectroscopic monitoring survey of Galactic O- and WN-type stars in the Southern Hemisphere. The IACOB database is currently comprised of mid B- to early O-type dwarfs and giants in the first half of the MS and O- and B-type supergiants in the second half of the MS and beyond. While the IACOB project has been working extensively in the past decade to obtain a magnitude limited sample for the whole covered domain of the HR diagram, there are still some incomplete regions that are affected by observational biases, which we discuss in Section 8.3.1.

4.1 The sample

This thesis uses a selection of 921 stars from the above IACOB+OWN collaboration, referred to as the IACBO sample. The sample includes likely single stars and single-line spectroscopic binaries (SB1). We exclude double-line spectroscopic binaries (SB2), as the spectroscopic analysis is more complex and thus the IACOB project has chosen to postpone the analysis to a later date (Holgado et al., 2020). Figure 4.1 shows the probability density function of the stars, calculated as explained in Section 3.3.

[1] research.iac.es/proyecto/iacob/

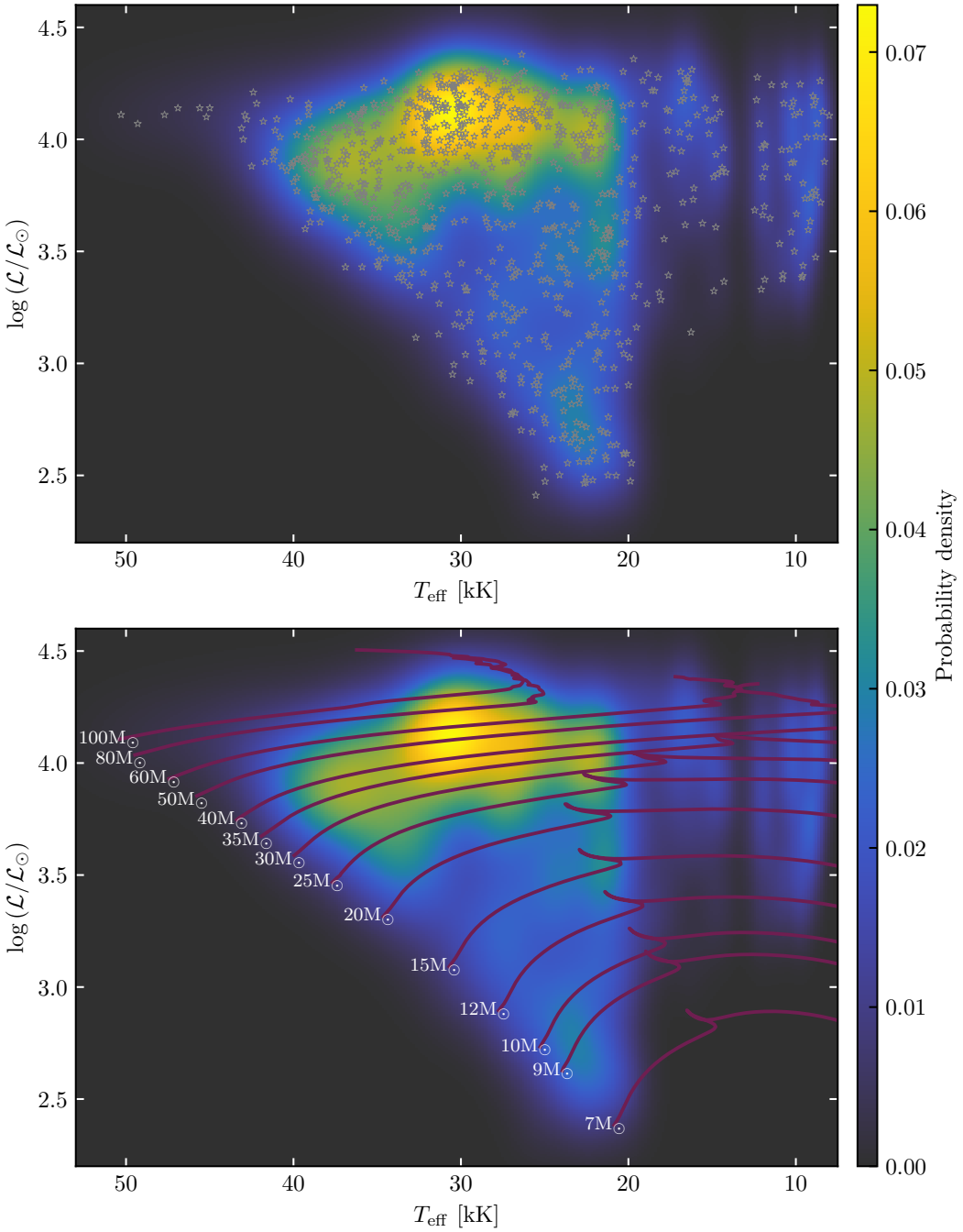

Figure 4.1: Both panels show the Gaussian probability density function of 921 stars from the IACOB project in the spectroscopic HR diagram. The top panel overplots the IACOB stars in gray. The bottom panel overplots evolutionary tracks from the Brott grid. The Brott tracks shown cover initial masses from $7\,M_\odot$ to $100\,M_\odot$ and have $v_{\rm ZAMS} \approx 218\,{\rm km\,s^{-1}}$.

We can see that the IACOB stars are concentrated at high masses, with a slight increase in number at the $\sim 9\,M_\odot$ model's ZAMS point. The brightest region, at $\sim 30\,kK$, $\sim 10^{4.0}\mathcal{L}_\odot$, is home to both O-type stars and B-type supergiants. There are a few stars present in the Hertzsprung gap, with a narrow empty region at $\sim 15\,kK$. The sample covers the majority of the MS, with only two empty regions, namely the second half of the MS for low mass stars and the ZAMS for high mass stars. For our spindown analysis, we consider IACOB stars on the MS, defined by the ZAMS and TAMS lines of the Brott tracks. For our envelope inflation analysis, we consider all IACOB stars with with $\log(\mathcal{L}/\mathcal{L}_\odot) \geq 3.7$.

4.2 Projected rotational velocity

As a star rotates, its spectral line profile undergoes Doppler broadening. By comparing this broadened profile with the line's known, unbroadened profile, we can obtain information about the star's projected rotational velocity. This method, however, assumes that all line-broadening is due to rotation, which is not the case. There are two main sources of line broadening in rotating stars. If a star's atmosphere has a small scale turbulent velocity field, known as microturbulence, then line-broadening can occur. In addition, OB stars have been observed to have a second source of turbulence, commonly called macroturbulence. This effect was initially thought to be due to large scale turbulent motion in the stellar atmosphere, but it has been theorized to be instead caused by stellar oscillations (Simón-Díaz et al., 2010). Both of these effects must be accounted for when determining projected rotational velocities.

The IACOB stars' projected rotational velocity, $v \sin i$, was derived with `iacob-broad`, an IDL program designed to characterize OB-type spectra (Simón-Díaz and Herrero, 2014). The program uses a combination of Fourier transform (FT) and goodness-of-fit methods to determine $v \sin i$. The FT method, introduced by Carroll (1933) and expanded upon by Gray (1976, 2005), works by identifying the first zero in the FT transform of the line profile. The zero point represents the overall mean of the signal, as frequency is the inverse of the period and $1/0$ is undefined, i.e., an infinite period. The frequency at the zero, σ_1, can be directly translated into the projected rotational velocity with

$$\frac{\lambda}{c}\sigma_1 v \sin i = 0.660, \tag{4.1}$$

where λ is the central line wavelength and c is the speed of light. This FT method allows separate determination of $v \sin i$ and the broadening due to macroturbulence, v_m, but it can still be affected by microturbulence.

The GoF method is based on line-fitting, in which the intrinsic profile of a line is

convolved with the relevant line-broadening profiles and compared to the observed profile, using a χ^2 formalism to determine best fit (Simón-Díaz and Herrero, 2014). This approach allows full characterization of line-broadening effects from rotation and macroturbulence, but not microturbulence. Consequently, the GOF method assumes all line-broadening not due to rotation can be incorporated into v_m. The `iacob-broad` program calculates $v \sin i$ using both the FT and GoF methods. If the results do not agree, then a user must use the provided information to choose the correct value (Simón-Díaz and Herrero, 2014).

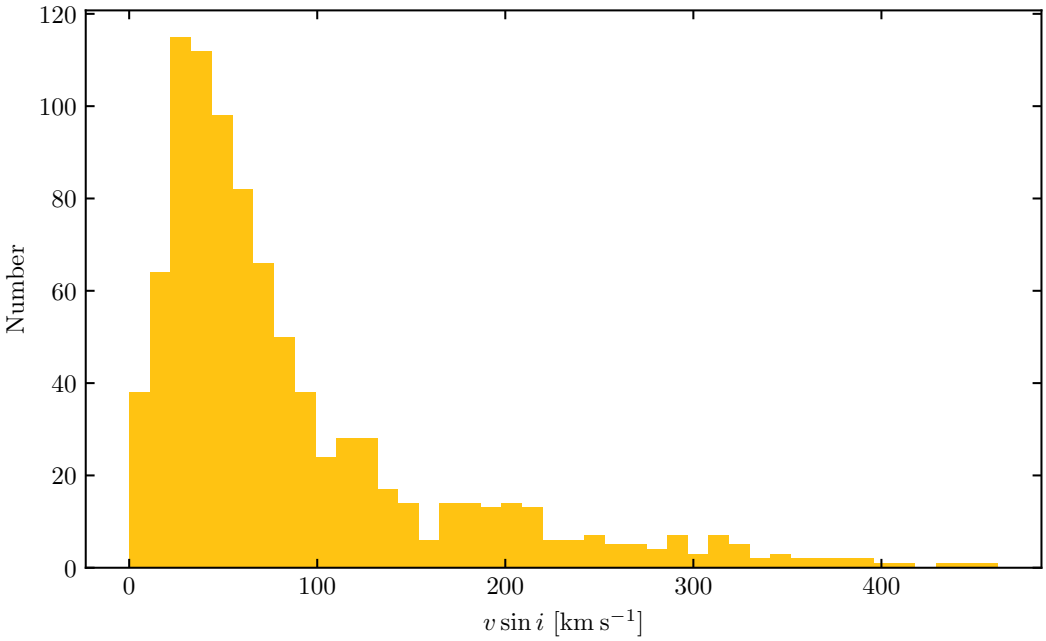

Figure 4.2: The distribution of projected rotational velocities for the IACOB stars, shown as a histogram with 11 km s^{-1} wide bins. Figure contains data from al 921 stars in the IACOB sample.

Figure 4.2 shows the distribution of projected rotational velocity, calculated with `iacob-broad`, for all 921 stars in our sample. We can see that the IACOB stars seem to have a bimodal distribution, seen by the a slow peak at ∼40 km s^{-1} and a fast peak at ∼180 km s^{-1}. While over a third of the 921 stars in the sample have a velocity between 0 km s^{-1} to 40 km s^{-1}, only 88 have a velocity below 20 km s^{-1}. The bimodal distribution dips down at ∼160 km s^{-1} before rising again for the fast peak. Most of the IACOB stars are contained in the slow peak, with only 143 stars with $v \sin i > 160$ km s^{-1}. There are not many rapid rotaters in the sample, with only 123 stars having $v \sin i > 180$ km s^{-1}, but the tail of the distribution extends out to ∼450 km s^{-1}.

Chapter 5

Model results

5.1 Brott synthetic populations

Section 3.1.1 discussed the error in the angular momentum loss calculation in the Brott grid and Figure 5.1 shows the result of applying the corrections to a Brott grid model. Figure 5.1b confirms that the model has a higher rate of angular momentum loss and Figure 5.1a confirms that the model loses more angular momentum overall. At ∼3.5 Myr the original data briefly shows a higher $\dot{J}$, which corresponds with the sudden decrease in total and surface angular momentum, seen in Figures 5.1a and 5.1c, and the rapid spindown seen in Figure 5.1d.

Conservation of angular momentum dictates that the total amount of angular momentum can only go down, but the proportions contained in different layers of the star can change. The original data in Figure 5.1c shows the model's surface angular momentum increasing before the loss rate sharply increases. This unexpected result means that angular momentum transport is briefly more efficient than the stellar winds. This feature disappears in the corrected data. The angular momentum transport may still be very efficient at this stage, but it is not enough to overpower the rate of mass loss and instead just stabilizes the surface angular momentum rate of change.

While Figures 5.1a and 5.1c show that the model loses much more angular momentum with the corrections, Figure 5.1d shows that the model still completely spins down by the end of its life, both before and after the corrections. The difference is in the spindown evolution, which occurs in two distinct phases in the original data, shifting from a shallow to steep slope at ∼3.5 Myr. The corrected data shows the model losing rotational velocity at a steady rate, although more rapidly than in the corrected data. There is a small increase in spindown rate at the same ∼3.5 Myr point, but since the model has already spun down so much it has minimal influence.

Overall, the corrections increase the amount of angular momentum lost, thereby reducing the impact of angular momentum transport and smoothing the rate of spindown. We expect that the effect of the corrections will decrease for lower masses and increase for higher masses, in accordance with the mass loss rate.

As discussed in Section 3.1, numerical processes can cause the rotation rate of a model

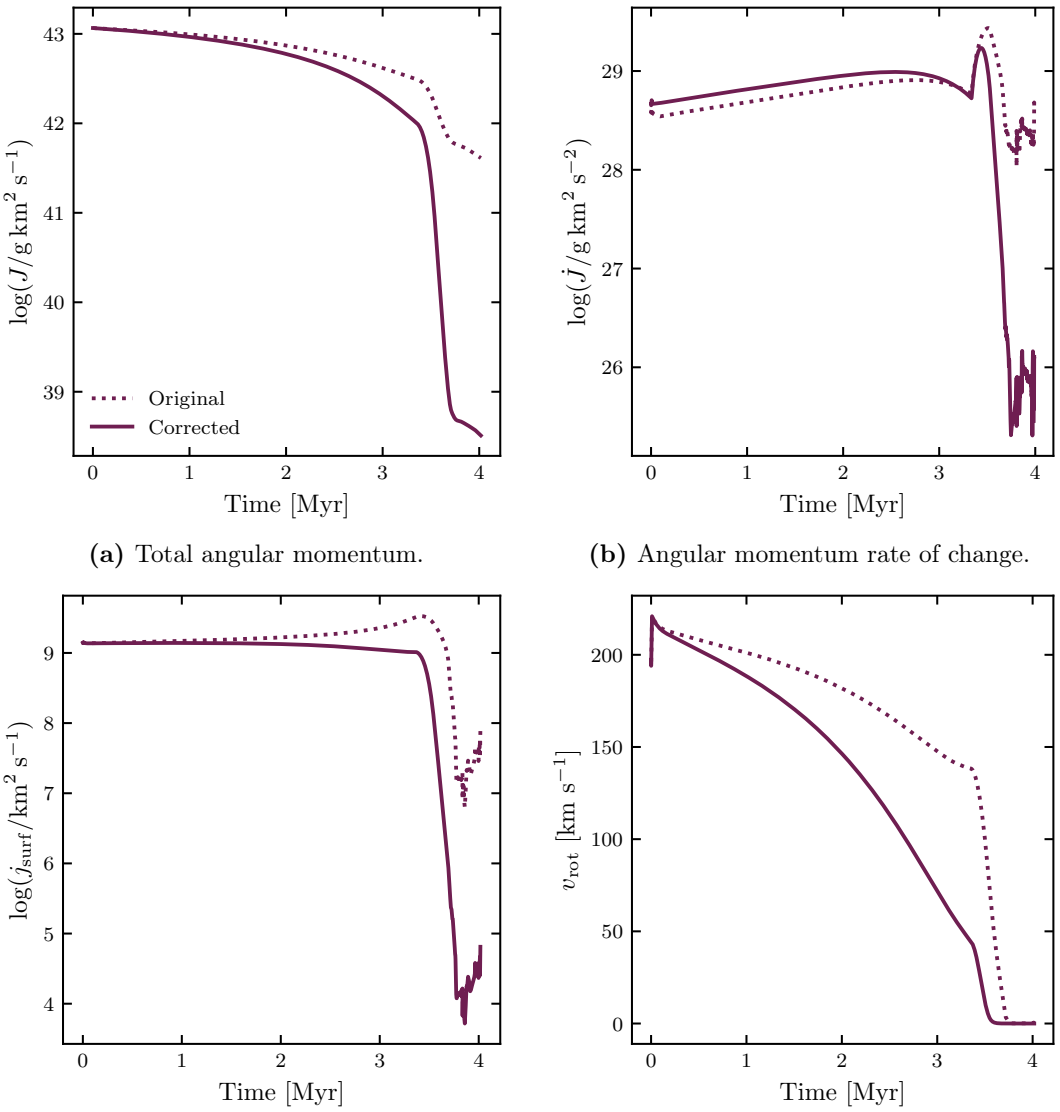

(a) Total angular momentum.

(b) Angular momentum rate of change.

(c) Surface specific angular momentum.

(d) Rotational velocity.

Figure 5.1: Total angular momentum, total angular momentum rate of change, surface specific angular momentum, and rotational velocity of a star with an initial mass of $50\,M_\odot$ and $v_i = 200\,\mathrm{km\,s^{-1}}$ from the Brott grid. The dotted line shows the original data and the solid line shows the recalculated data following the procedure outlined in Section 3.1.1.

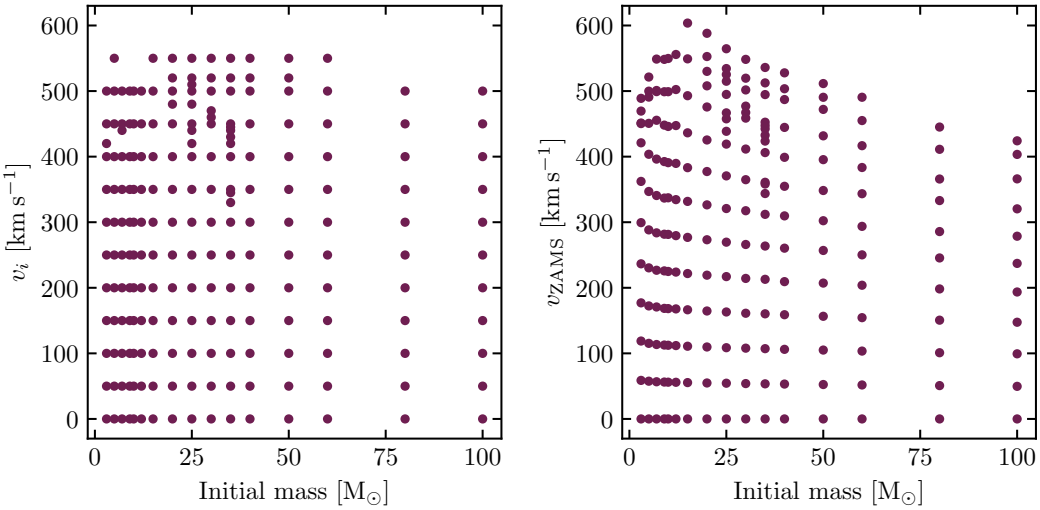

Figure 5.2: The parameter space of the Brott grid. Left panel shows the initial masses and rotational velocities of the models, as set in the stellar code. Right panel shows the initial masses and rotational velocities at the ZAMS, which is defined in this thesis as when 5% of the initial core hydrogen has been burned.

to change between the start of a simulation and the ZAMS. In addition, physical spindown can occur in the period between core hydrogen ignition and our chosen ZAMS point. The left panel of Figure 5.2 shows the initial mass and velocity of each model in the Brott grid, while the right panel shows the initial mass and the velocity at the ZAMS. For lower mass models, the values are very similar, with some even having a small increase in rotation rate. For higher mass models, however, the ZAMS velocity is markedly lower than the initial velocity, with a difference of up to 15 %. When interpolating simulated stars with a given $v_{\rm ZAMS}$, it is therefore important to pick the appropriate stellar models based on the true ZAMS velocity and not the initial velocity.

Our derived velocity PDF and the IACOB distribution of projected rotational velocity are plotted in Figure 5.3. The fitting process is described in Section 3.2.1. There is relatively good agreement between the derived PDF and the observed distribution and the large-scale structure is preserved, even if the amplitudes of the peaks are too low. The second peak is more prominent in the IACOB distribution, as the contribution from the larger peak's Gaussian smooths out the second peak in the PDF. In terms of this PDF's use as an initial velocity distribution, it is important to remember that it was fitted to a distribution of current velocities and as such is just an estimation to be used experimentally.

Figure 5.4 shows the Brott single $v_{\rm ZAMS}$ population in a spectroscopic HR diagram. The Brott grid evolutionary tracks used for interpolation are plotted on top of

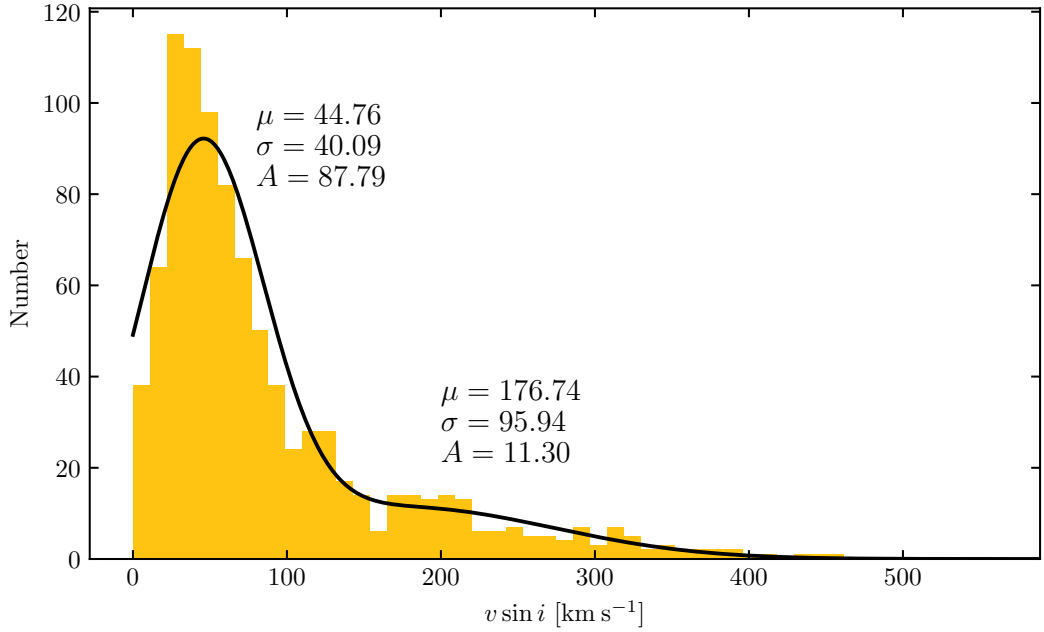

Figure 5.3: The histogram of the IACOB stars' projected rotational velocity, the same as Figure 4.2, except now with the addition of the fitted function from Section 3.2.1. The μ, σ, and A next to each peak are the parameters used in each Gaussian.

the simulated stars, as well as lines dividing the MS into quarters based on what percentage of the initial center hydrogen mass fraction has been burned. The figure is formatted as a two-dimensional histogram, meaning that the color indicates the number of simulated stars located in that pixel.

As expected, the majority of simulated stars are young and low-mass. The number of simulated stars in any given pixel then decreases as we move across the MS. We expect this same behavior as we move up in initial mass, but the number of simulated stars per pixel stops decreasing and begins to increase after the $50\,M_\odot$ track. This does not mean that the number of simulated stars as a function of initial mass is increasing; instead, this is a side effect of our flat IMF and due to the relationship between spectroscopic luminosity and mass. The spectroscopic luminosity can be approximated as $\mathcal{L} \sim L/M$ (Langer and Kudritzki, 2014), which can be combined with the standard luminosity-mass relation of $L \propto M^{3.8}$ (Pols, 2011) to obtain $\mathcal{L} \sim M^{2.8}$, an exponential relationship. As an example, there are 114 625 simulated stars with initial masses between $10\,M_\odot$ to $30\,M_\odot$, versus only 33 423 between $80\,M_\odot$ to $100\,M_\odot$. The vertical space these simulated stars occupy, however, is not proportionate to their number. The difference between the $\log(\mathcal{L}_{\rm ZAMS}/\mathcal{L}_\odot)$ values of the $10\,M_\odot$ and $30\,M_\odot$ models is 0.85 dex, while the $80\,M_\odot$ and $100\,M_\odot$ have a spacing of only 0.07 dex. There are ∼70 % fewer simulated stars in the higher mass

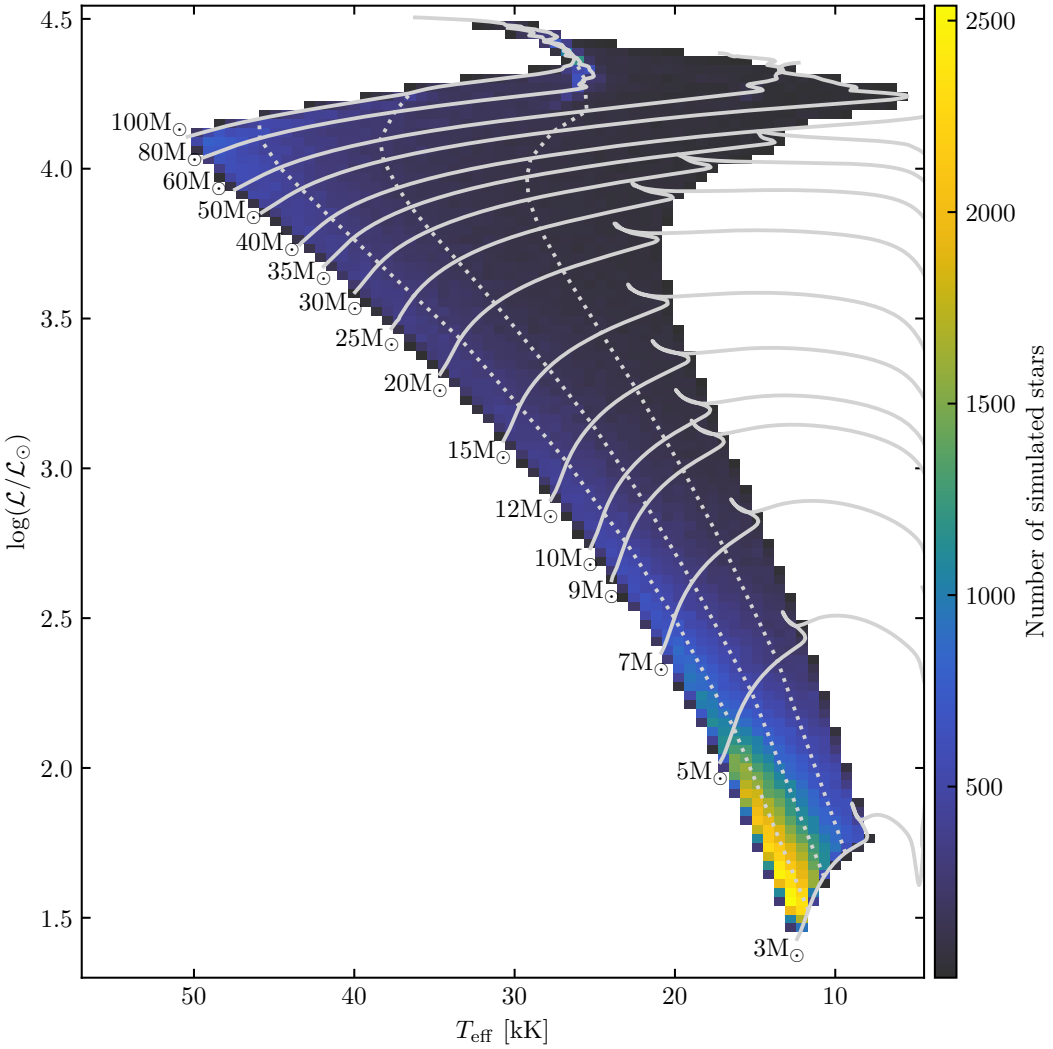

Figure 5.4: The Brott single v_{ZAMS} population, shown in a spectroscopic HR histogram. The color indicates how many simulated stars are located in a pixel. The figure contains data from 619 724 simulated stars. The initial mass range is from $3\,\mathrm{M}_\odot$ to $100\,\mathrm{M}_\odot$ with a $v_{\mathrm{ZAMS}} = 200\,\mathrm{km\,s^{-1}}$. The solid gray lines are evolutionary tracks from the Brott grid, here with $v_i = 200\,\mathrm{km\,s^{-1}}$. The dotted gray lines divide the MS into four quarters. The first line marks when 25 % of the initial core hydrogen has been burnt, the second marks when 50 % of the initial core hydrogen has been burnt, the third marks when 75 % of the initial core hydrogen has been burnt. The interpolated data ends at the TAMS.

range, but they are occupying an order of magnitude less vertical space.

There is another high-mass bright area in the upper right, where the evolutionary tracks of the 80 $M_\odot$ and the 100 $M_\odot$ overlap. This area has a similar explanation, as all simulated stars interpolated between these two tracks are located in the same small area of the spectroscopic HR diagram.

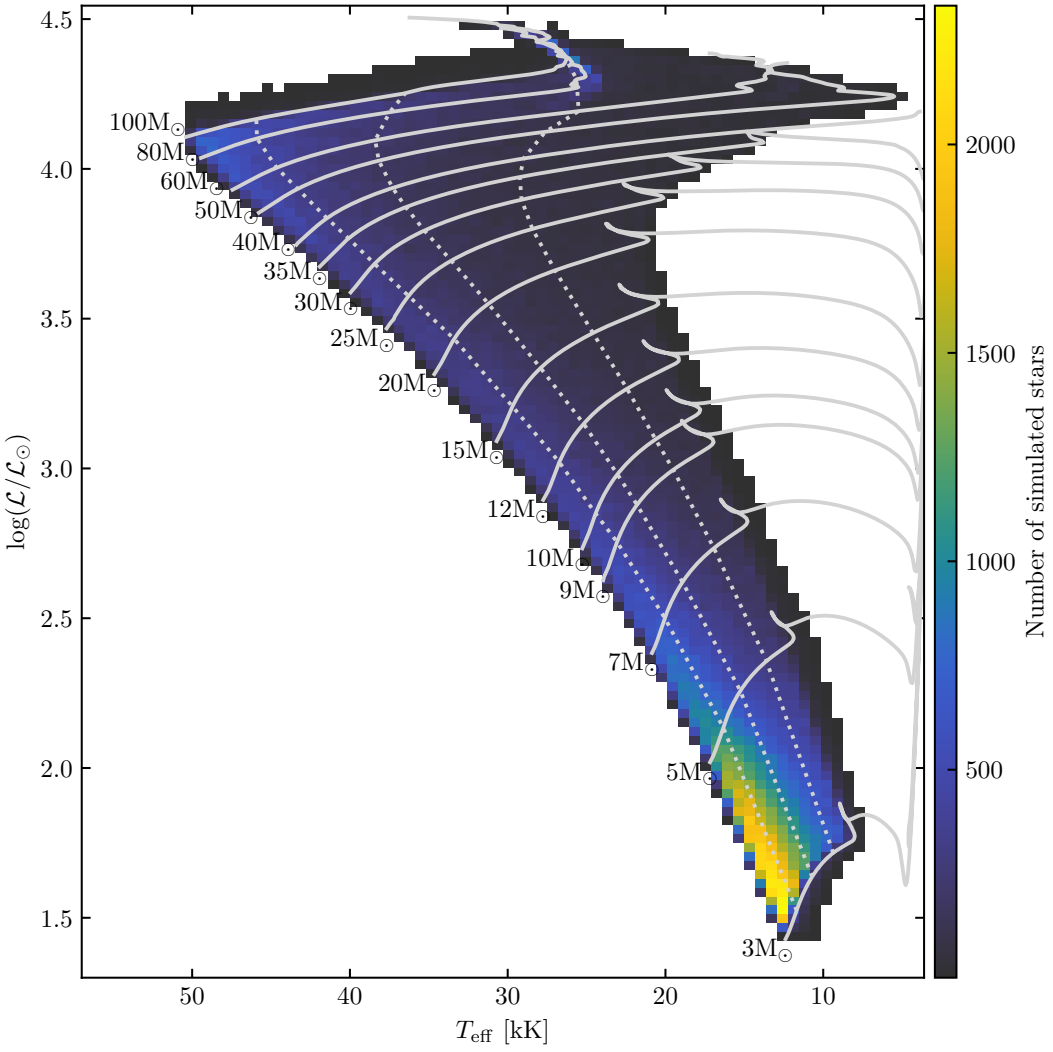

Figure 5.5: The Brott distribution v_{ZAMS} population, shown in a spectroscopic HR histogram of the same format as Figure 5.4. The initial mass range is from 3 $M_\odot$ to 100 $M_\odot$ and the ZAMS velocity distribution uses the PDF described in Section 3.2.1. The solid gray lines are the same Brott grid evolutionary tracks as in Figure 5.4 and the dotted gray lines are the same MS divisions. The figure contains data from 600 522 simulated stars.

The Brott distributed v_{ZAMS} population is shown in Figure 5.5, in the same format

as Figure 5.4. This population was not interpolated with a constant v_{ZAMS}, instead using the velocity PDF described in Section 3.2.1. Rotational velocity can affect spectral luminosity and effective temperature, especially for rapidly rotating stars, so this spectroscopic HR diagram covers a greater area than that of Figure 5.4. This is why there are dark areas of low density along the ZAMS and TAMS lines, as well as along the evolutionary tracks of the $3\,\mathrm{M}_{\odot}$ and $100\,\mathrm{M}_{\odot}$ models. These low density areas contain simulated stars that were interpolated with v_{ZAMS} values close to the upper and lower limits of the velocity PDF.

5.1.1 Application of angular momentum corrections

Figure 5.1 showed the consequences of the angular momentum corrections on a single evolutionary model. We now discuss the consequences for the entire mass range of the Brott grid, using the Brott single v_{ZAMS} population.

Effect on rotational velocity

Figure 5.6 shows the distribution of rotational velocities in the Brott single v_{ZAMS} population before and after the angular momentum corrections. The population is divided into six mass bins, each of which are then split into four bins for the four quarters of the MS, as described earlier in Figure 5.4. This method allows us to see how rotational velocity evolves with both mass and time.

Initial mass of $3\,\mathrm{km\,s^{-1}}$ to $15\,\mathrm{km\,s^{-1}}$ Low mass stars do not have strong stellar winds, which means their angular momentum loss and spindown are both small. Thus, the angular momentum corrections should have a negligible effect on simulated stars in the lowest mass bin. Additionally, spindown should be limited for both the original and corrected data. The top left panel of Figure 5.6, simulated stars with an initial mass between $3\,\mathrm{M}_{\odot}$ to $15\,\mathrm{M}_{\odot}$, agrees with these expectations. The angular momentum corrections did not change the spindown of these simulated stars and the spindown itself is minimal. Even in the last quarter of the MS, neither the original nor corrected data shows any simulated stars with a velocity below $130\,\mathrm{km\,s^{-1}}$.

Initial mass of $15\,\mathrm{km\,s^{-1}}$ to $30\,\mathrm{km\,s^{-1}}$ The angular momentum corrections do cause changes in the $15\,\mathrm{M}_{\odot}$ to $30\,\mathrm{M}_{\odot}$ bin, but they are very slight. The original data shows the simulated stars experiencing very little spindown in the first half of the MS. The third quarter has some spindown, with some simulated stars reaching $\sim$$165\,\mathrm{km\,s^{-1}}$. Most of the spindown occurs in the fourth quarter of the MS, which has an almost completely flat distribution, although nearly all the simulated stars are rotating above $\sim$$150\,\mathrm{km\,s^{-1}}$.

In contrast, the corrected data shows that the simulated stars start spinning down in the first quarter of the MS. The slowest simulated stars in the second quarter of the

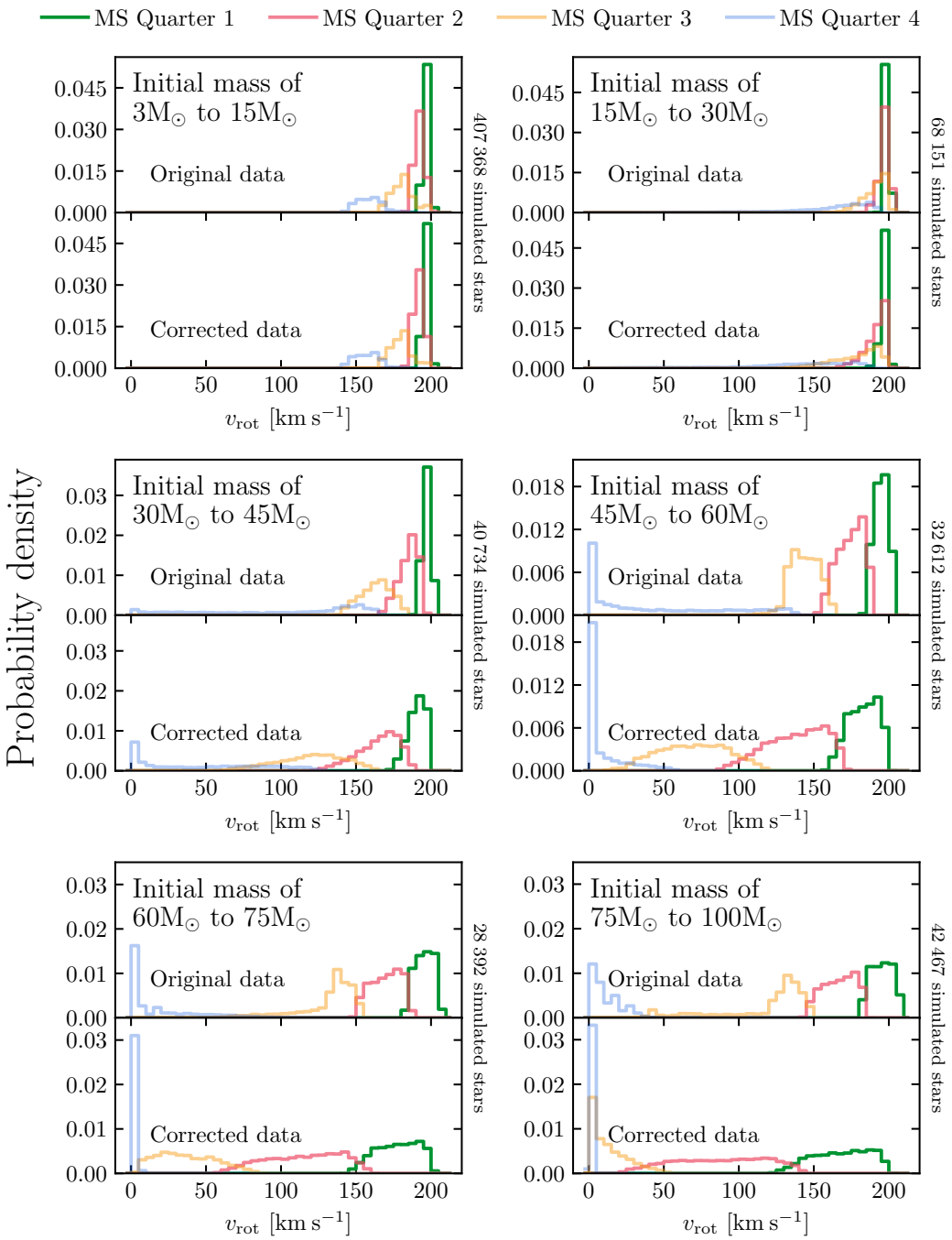

Figure 5.6: Distributions of rotational velocity from the Brott single $v_{\rm ZAMS}$ population before and after the angular momentum corrections discussed in Section 3.1.1. Each panel shows the data for an initial mass range with the original data above and the corrected data below. The MS quarter is indicated by color, as explained in Figure 5.4. The plots are normalized so that the sum of integrating over all four histograms is 1.

MS are already at $\sim$165 km s^{-1} and the third quarter contains simulated stars as slow as $\sim$130 km s^{-1}. The fourth quarter histogram is more similar to that of the original data, as they are both very extended and flat. The corrected data, however, shows that nearly half of the simulated stars in this quarter have spun down to velocities below $\sim$150 km s^{-1}.

Initial mass of 30 km s^{-1} to 45 km s^{-1} The 30 M$_\odot$ to 45 M$_\odot$ bin has greater changes between the original and corrected data, as higher mass stars lose more angular momentum. Despite this, the original data shows the simulated stars in the first quarter of the MS still clustered at $v_{\rm ZAMS}$, with the slowest simulated stars only at $\sim$195 km s^{-1}. There is more spindown evolution in the second quarter of the MS, which has simulated stars between $\sim$165 km s^{-1} to $\sim$196 km s^{-1}. The spindown continues in the third quarter of the MS, although the slowest simulated stars are still at $\sim$139 km s^{-1}. Most of the spindown still occurs in the fourth quarter of the MS, which goes from 0 km s^{-1} to $\sim$167 km s^{-1}.

The corrected data shows the simulated stars spinning down significantly in the first quarter of the MS, with some reaching $\sim$173 km s^{-1}. The spindown rate increases in the second quarter, and simulated stars spin down to rates as slow as $\sim$122 km s^{-1}. The distribution is very broad for both the third and fourth quarters, showing that most of the spindown takes place in the second half of the MS. There is a small peak at 0 km s^{-1} in the fourth quarter of the MS, so some simulated stars have completely spun down.

Initial mass of 45 km s^{-1} to 60 km s^{-1} We can see significant spindown in the original and corrected data for the 45 M$_\odot$ to 60 M$_\odot$ bin. The original data shows the simulated stars in the first quarter of the MS have begun to spin down, although most spindown still takes place in the fourth quarter of the MS. It takes the first three quarters of the MS for the simulated stars to spin down from $\sim$200 km s^{-1} to $\sim$100 km s^{-1}, but only one quarter for them to spin down to 0 km s^{-1}, although some fourth quarter simulated stars are still rotating as rapidly as $\sim$138 km s^{-1}. This rapid fourth quarter spindown is because between 40 M$_\odot$ to 50 M$_\odot$ is the point where the Brott grid models lose their envelopes while still on the MS. Thus, the majority of simulated stars that are considered here become Wolf-Rayet (WR) stars in the final quarter of the MS. WRs have very strong stellar winds and high mass loss rates, and as a result spin down rapidly (Pols, 2011).

The corrected data shows much more consistent spindown, with no long extended tails in any of the distributions. Simulated stars already begin to slow significantly in the first quarter of the MS, with some down to $\sim$160 km s^{-1}. Even more spindown takes place in the second quarter of the MS, which contains simulated stars with velocities between $\sim$85 km s^{-1} to $\sim$170 km s^{-1}. The most spindown, however, occurs in the third quarter of the MS, with some simulated stars spinning as rapidly as

$\sim$120 km s^{-1} and others as slowly as $\sim$10 km s^{-1}. As discussed earlier, the high number of completely spun down simulated stars in the fourth quarter of the MS is due to many becoming WRs. By the time the simulated stars reach the fourth quarter of the MS, however, they have completed the majority of their spindown, with the fastest stars only reaching $\sim$60 km s^{-1}.

Initial mass of 60 km s^{-1} to 75 km s^{-1} The 60 M$_\odot$ to 75 M$_\odot$ bin is where significant mass loss begins as early as the third quarter of the MS, which causes equally significant spindown. The original data shows simulated stars spinning down to $\sim$54 km s^{-1} by the third quarter of the MS, although the majority of simulated stars in the first three quarters of the MS are above $\sim$125 km s^{-1}. While some simulated stars in the fourth quarter of the MS are still rotating at $\sim$108 km s^{-1}, most have spun down nearly completely.

The corrected data again has more consistent spindown and none of the distributions for the first three quarters of the MS have clear peaks. Simulated stars in the first quarter span $\sim$200 km s^{-1} to $\sim$145 km s^{-1}, while the second quarter goes from $\sim$161 km s^{-1} to $\sim$57 km s^{-1}. Simulated stars in the third quarter do not have quite as wide range, going from $\sim$86 km s^{-1} to $\sim$3 km s^{-1}. Nearly all the spindown takes place in the first three quarters of the MS, as the simulated stars in the fourth quarter have a maximum velocity of $\sim$9 km s^{-1}.

Initial mass of 75 km s^{-1} to 100 km s^{-1} The highest mass bin, 75 km s^{-1} to 100 km s^{-1}, contains simulated stars that lose their envelopes while still in the third quarter of the MS. The original data still shows only limited spindown in the first half of the MS, with the slowest simulated stars at $\sim$144 km s^{-1}. The increased third quarter mass loss is reflected by the long tail of the third quarter distribution, which extends to $\sim$31 km s^{-1}. The spindown is mostly complete by the fourth quarter of the MS, as the maximum velocity for stars in this quarter is $\sim$50 km s^{-1}

The corrected data does not show the phased of spindown and instead shows the simulated stars slowing down throughout the MS. Some simulated stars in the first quarter of the MS have already spun down to $\sim$122 km s^{-1}, but most of the spindown takes place in the second quarter of the MS, which ranges from $\sim$20 km s^{-1} to $\sim$144 km s^{-1}. The stronger spindown in the corrected data means that the third quarter of the MS already has some simulated stars that are completely spun down and all of the simulated stars in the fourth quarter of the MS are completely spun down.

Effect on surface angular momentum

Figure 5.7 shows the distributions of surface specific angular momentum, $j_{\rm surf}$, for the same simulated stars shown in Figure 5.6. We can immediately see that the

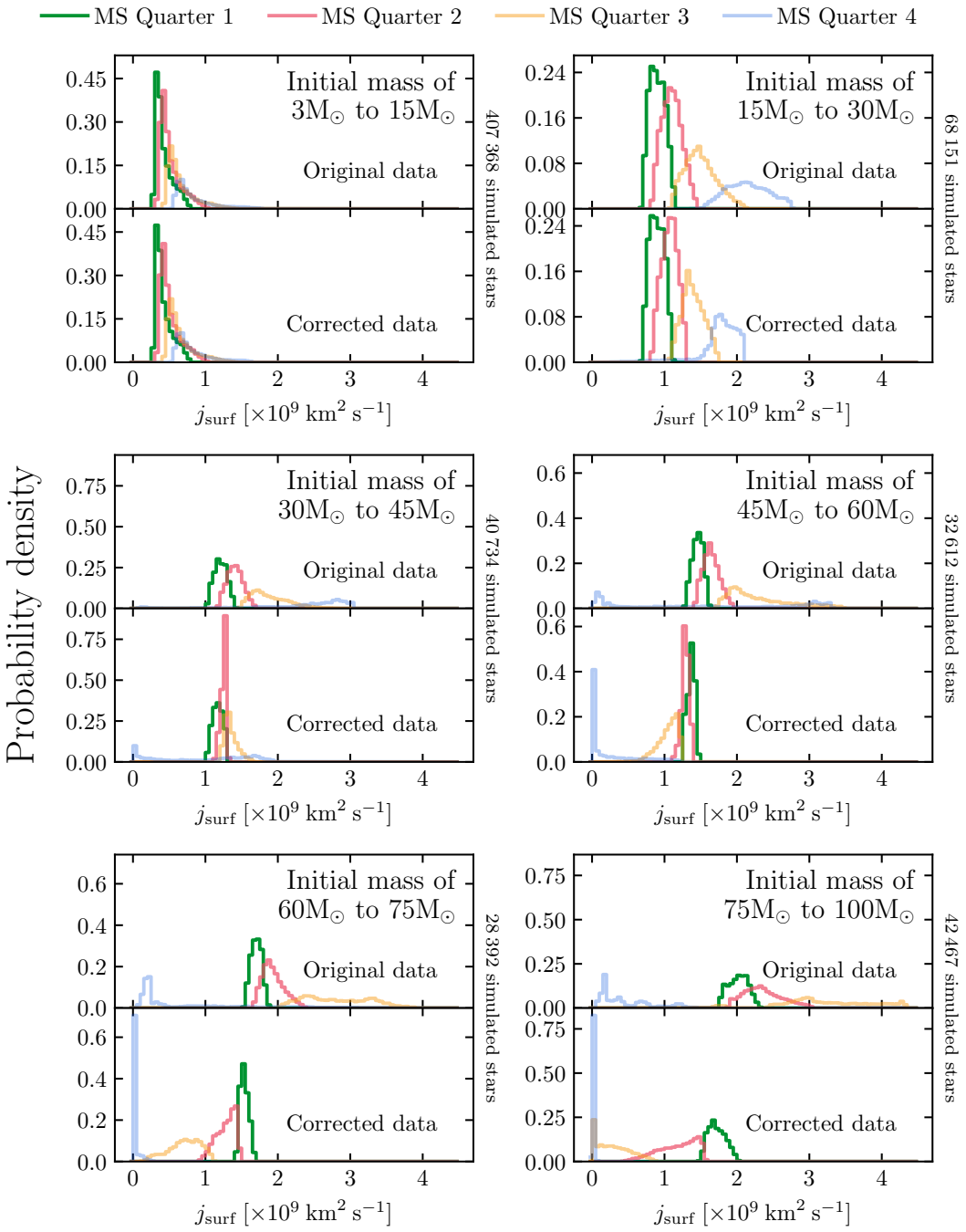

Figure 5.7: Distributions of surface specific angular momentum from the Brott single v_{ZAMS} population before and after the angular momentum corrections discussed in Section 3.1.1. The figure is formatted in the same way as Figure 5.6.

original data has a much larger maximum j_{surf} value than the corrected data in every mass bin, with the difference increasing as we go up in mass. In the final mass bin, simulated stars with an initial mass between $75\,M_\odot$ to $100\,M_\odot$, the original data has a maximum value of $\sim 4.3 \times 10^9\,\text{km}^2\,\text{s}^{-1}$, while the corrected data's highest value is less than half that at $\sim 2.0 \times 10^9\,\text{km}^2\,\text{s}^{-1}$. This agrees with Figure 5.1, which showed that the Brott model star's original data had greater J and j_{surf} values, and even increased j_{surf}.

Initial mass of $3\,\text{km}\,\text{s}^{-1}$ to $15\,\text{km}\,\text{s}^{-1}$ As in Figure 5.6, the lowest mass range, $3\,M_\odot$ to $15\,M_\odot$, does not show any change between the original and corrected data. The maximum j_{surf} value in each quarter of the MS keeps increasing and the minimum value keeps decreasing, showing that the angular momentum transport processes are so efficient that these simulated stars gain j_{surf} throughout the MS. Any net j_{surf} loss must occur after the TAMS. Since low mass stars have very limited mass loss, angular momentum transport does not need an unrealistically high efficiency to be able to replenish j_{surf} faster than it can be lost.

Initial mass of $15\,\text{km}\,\text{s}^{-1}$ to $30\,\text{km}\,\text{s}^{-1}$ The $15\,M_\odot$ to $30\,M_\odot$ bin shows small changes between the original and corrected data, mostly in the second half of the MS. The first half of the MS is the same for both the original and corrected data, and just shows the simulated stars gaining j_{surf}. The original data shows that simulated stars in the third quarter of the MS have a maximum j_{surf} value of $\sim 2.14 \times 10^9\,\text{km}^2\,\text{s}^{-1}$, increasing to $\sim 2.76 \times 10^9\,\text{km}^2\,\text{s}^{-1}$ in the fourth quarter of the MS.

The simulated stars gain j_{surf}, but not as much. The maximum value in the third quarter of the MS is $\sim 1.75 \times 10^9\,\text{km}^2\,\text{s}^{-1}$, $\sim 20\,\%$ lower than in the original data. The simulated stars in the fourth quarter of the MS have a maximum j_{surf} of $\sim 2.11 \times 10^9\,\text{km}^2\,\text{s}^{-1}$, less than the maximum value in the third quarter for the original data.

Initial mass of $30\,\text{km}\,\text{s}^{-1}$ to $45\,\text{km}\,\text{s}^{-1}$ The $30\,M_\odot$ to $45\,M_\odot$ bin shows significant change between the original and corrected data. The original data shows the simulated stars gaining some j_{surf} in the first half of the MS, but then a large increase in the second half of the MS. Simulated stars in the fourth quarter reach j_{surf} values up to $\sim 3.05 \times 10^9\,\text{km}^2\,\text{s}^{-1}$. This large increase in j_{surf} occurs at the same point that the rate of spindown is increasing, which is inconsistent with our understanding of angular momentum transport and spindown.

The corrected data shows that the simulated stars gain j_{surf} through the first three quarters of the MS, and some of the fourth quarter, before beginning to lose it. The simulated stars in the third quarter have a very narrow distribution compared to those in the first and third quarter. The fourth quarter has a very broad distribution,

ranging from $0\,\mathrm{km^2\,s^{-1}}$ to $\sim 1.96 \times 10^9\,\mathrm{km^2\,s^{-1}}$, as some of these simulated stars are completely spun down.

Initial mass of $45\,\mathrm{km\,s^{-1}}$ to $60\,\mathrm{km\,s^{-1}}$ The $45\,\mathrm{M_\odot}$ to $60\,\mathrm{M_\odot}$ bin is where the behavior shown in the original and corrected data completely diverges. The original data shows the simulated stars gaining j_{surf} throughout the first three quarters of the MS, reaching values of $\sim 3.51 \times 10^9\,\mathrm{km^2\,s^{-1}}$. The simulated stars do lose j_{surf} in the fourth quarter of the MS, and some have lost all their j_{surf}, but there are still simulated stars with j_{surf} values up to $\sim 3.36 \times 10^9\,\mathrm{km^2\,s^{-1}}$.

The corrected data no longer shows any j_{surf} gain on the MS. The simulated stars lose a limited amount of j_{surf} in the first three quarters of the MS, but the majority still have j_{surf} values above $\sim 0.55 \times 10^9\,\mathrm{km^2\,s^{-1}}$. Simulated stars in the fourth quarter of the MS have j_{surf} values between $0\,\mathrm{km^2\,s^{-1}}$ to $\sim 1.23 \times 10^9\,\mathrm{km^2\,s^{-1}}$, with most in the peak at $0\,\mathrm{km^2\,s^{-1}}$, reflecting the fact that these simulated stars are rotating below $\sim 50\,\mathrm{km\,s^{-1}}$ and some have completely spun down.

Initial mass of $60\,\mathrm{km\,s^{-1}}$ to $75\,\mathrm{km\,s^{-1}}$ The $60\,\mathrm{M_\odot}$ to $75\,\mathrm{M_\odot}$ bin contains simulated stars that spin down significantly in both the original and corrected data. The original data, however, still keeps the same overall structure as in the previous mass bin. The simulated stars gain j_{surf} in the first three quarters of the MS, and the maximum value increases to $\sim 3.91 \times 10^9\,\mathrm{km^2\,s^{-1}}$. They do lose j_{surf} in the fourth quarter of the MS, although a tiny minority still reach $\sim 3.42 \times 10^9\,\mathrm{km^2\,s^{-1}}$. The majority have lost nearly all their j_{surf}, however, and the distribution peaks at $\sim 0.23\,\mathrm{km^2\,s^{-1}}$.

The corrected data shows that the first quarter of the MS has a very similar j_{surf} distribution as in the previous mass bin, but the second and third quarters show significantly more evolution. The j_{surf} loss across the MS has the same structure as the spindown, with the majority of simulated stars losing all their j_{surf} by the third quarter of the MS. The fourth quarter of the MS peaks at $0\,\mathrm{km^2\,s^{-1}}$ and has a maximum value of only $\sim 0.28 \times 10^9\,\mathrm{km^2\,s^{-1}}$, corresponding with the nearly complete spindown we see in this quarter.

Initial mass of $75\,\mathrm{km\,s^{-1}}$ to $100\,\mathrm{km\,s^{-1}}$ The highest mass bin, $75\,\mathrm{M_\odot}$ to $100\,\mathrm{M_\odot}$, contains simulated stars with very high rates of MS mass loss. The original data, however, still shows j_{surf} gain. The maximum value increases again, reaching $\sim 4.34 \times 10^9\,\mathrm{km^2\,s^{-1}}$ in the third quarter. This rapid increase in j_{surf} is matched by an equally rapid decrease in the fourth quarter of the MS. These simulated stars have j_{surf} values ranging from $\sim 0.88 \times 10^9\,\mathrm{km^2\,s^{-1}}$ to $\sim 1.88 \times 10^9\,\mathrm{km^2\,s^{-1}}$. These simulated stars do not increase their rotation rate while on the MS, but they do increase j_{surf}.

The corrected data shows much more even j_{surf} loss in the first three quarters of the MS than in previous bins, and the three distributions all have similar maximum heights. Similar to the spindown, these simulated stars lose most of their j_{surf} while in the first half of the MS, with values ranging from $\sim 0.42 \times 10^9\,\text{km}^2\,\text{s}^{-1}$ to $\sim 2.03 \times 10^9\,\text{km}^2\,\text{s}^{-1}$. The simulated stars that spin down completely in the third quarter are located in the small peak at $0\,\text{km}^2\,\text{s}^{-1}$. The simulated stars have lost all their j_{surf} by the fourth quarter, which consists of a single peak at $0\,\text{km}^2\,\text{s}^{-1}$.

The angular momentum corrections have little to no effect for simulated stars below $30\,\text{M}_\odot$. By $45\,\text{M}_\odot$, however, the changes between the original and corrected data are significant. The corrected data shows the simulated stars spinning down more consistently and more rapidly than in the original data, as well as losing j_{surf} rather than gaining it. For masses above $60\,\text{M}_\odot$, the corrected data shows that the simulated stars have nearly all completely spun down and lost their j_{surf} by the fourth quarter of the MS. This is not seen in the original data, which shows the simulated stars gaining j_{surf} throughout the MS, even as they are spinning down. This behavior is not consistent with our understanding of angular momentum transport's role in spindown.

5.2 MESA models and synthetic populations

We calculated the MESA models and synthetic populations as described in Sections 3.1 and 3.2. The $12\,\text{M}_\odot$ models did not show any signs of inflation on the MS, so we did not show them and excluded them from analysis. Additionally, the $\alpha_{5.0}$ grid showed marked differences to the $\alpha_{0.5}$ and $\alpha_{1.5}$ grids at low initial masses where the α_{MLT} value is not expected to have an effect. We did not see signs of inflation in these models' density profiles and the cause of this abnormality is unknown. We assume that this behavior is due to MESA numerics and these lower mass $\alpha_{5.0}$ models are also excluded from analysis and interpolation.

Figure 5.8 shows the three MESA grids, one plot for each α_{MLT} value. The three plots in the figure have the same boundaries, making it easy to see that the grids have a higher maximum spectroscopic luminosity as the α_{MLT} value increases. This is partially because some of the higher mass models in the $\alpha_{0.5}$ and $\alpha_{1.5}$ grids terminate before reaching the TAMS, so the tracks do not extend as far. This does not fully explain the difference, however, and the plots show that models with a higher mixing length parameter increase their spectroscopic luminosity more rapidly. As discussed in Section 2.2, models with a higher mixing length parameter have more efficient heat transfer and are hotter. Spectroscopic luminosity is dependent on effective temperature to the fourth power (Equation 1.1), so even a small increase in effective temperature will have a large effect on the spectroscopic luminosity.

The point at which the different α_{MLT} values begin to have an effect varies as a

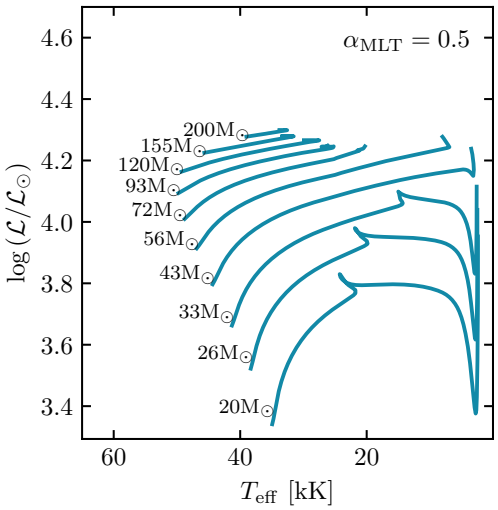

(a) MESA models with $\alpha_{\rm MLT} = 0.5$.

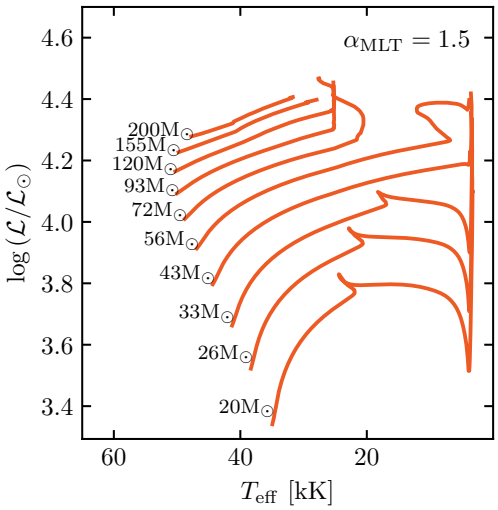

(b) MESA models with $\alpha_{\rm MLT} = 1.5$.

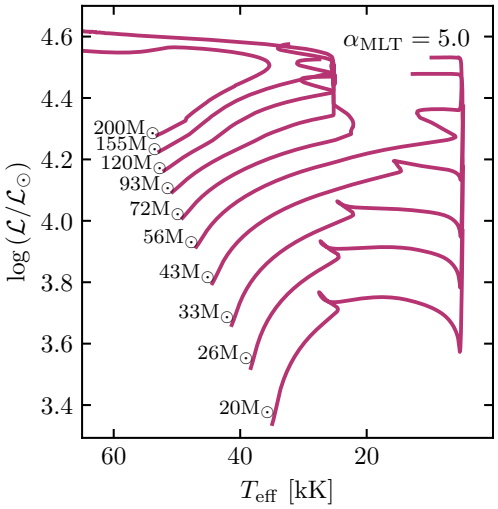

(c) MESA models with $\alpha_{\rm MLT} = 5.0$.

Figure 5.8: Evolutionary tracks of stellar models from the MESA grid, shown in the spectroscopic HR diagram for three different values of the mixing length parameter $\alpha_{\rm MLT}$. The initial masses are from 20 $M_\odot$ to 200 $M_\odot$ and the initial rotational velocity is 150 km s^{-1}.

function of initial mass and point on the MS, which can be seen in Figure 5.9. Models with a greater $\alpha_{\rm MLT}$ parameter can reach hotter effective temperatures for a given luminosity and have a higher Eddington luminosity. This effect only matters for stars that are near the Eddington limit, however, and at the ZAMS only the models with an initial mass of 72 $M_\odot$ and above fulfill this criteria. Moving to the midpoint of the MS shows the three $\alpha_{\rm MLT}$ lines start to diverge as early as 56 $M_\odot$ and by the TAMS the lines are diverging at 26 $M_\odot$.

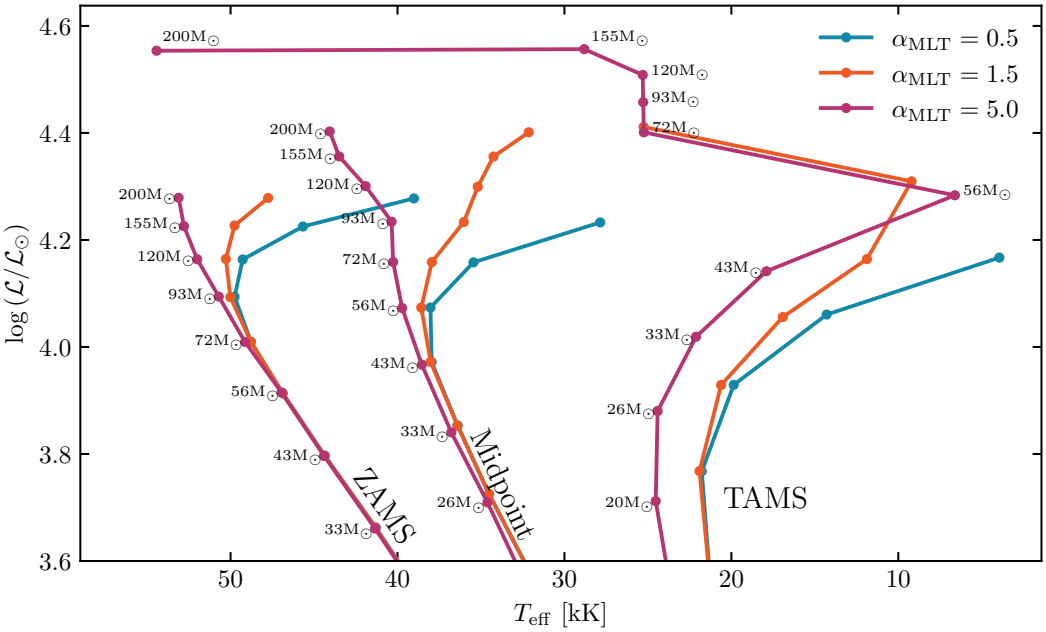

Figure 5.9: The ZAMS, MS halfway point, and TAMS lines of the MESA grid stellar models for three different mixing length parameter values, shown in the spectroscopic HR diagram. The midpoint is defined as when half of the initial core hydrogen has been burnt. The ZAMS line begins at $33\,M_\odot$ and goes to the highest initial mass calculated, $200\,M_\odot$. The midpoint and TAMS lines begin at $26\,M_\odot$ and $20\,M_\odot$, respectively, and are shortened based on when simulations failed to converge. The $\alpha_{MLT} = 0.5$ models did not reach the midpoint past an initial mass of $93\,M_\odot$ and did not reach the TAMS past an initial mass of $43\,M_\odot$. The $\alpha_{MLT} = 1.5$ models did not reach the TAMS past an initial mass of $93\,M_\odot$. The $\alpha_{MLT} = 5.0$ models all reached the midpoint and the TAMS.

The effect of a higher mixing length parameter is clear in Figure 5.10. While the different mixing length parameter values do not have a large effect on the spectroscopic luminosities at the ZAMS, the temperatures vary widely between the three α_{MLT} lines. The $\alpha_{5.0}$ line (in purple) is nearly linear and only slightly deviates from linearity above $120\,M_\odot$. The $\alpha_{1.5}$ and $\alpha_{0.5}$ lines (in orange and turquoise, respectively) are linear at lower masses but start bending above $72\,M_\odot$ and have switched their slopes from negative to positive by the end of the lines. Models with a higher α_{MLT} are constantly bringing heat to the surface by virtue of their higher heat transfer efficiency, slowing the rate at which they cool. The models with the lower α_{MLT} values, however, have inefficient convection in their envelopes and are limited in the amount of heat they can bring from the center to the surface, causing them to cool faster.

The populations we interpolated with the MESA grids are shown in Figure 5.11 as normalized two-dimensional spectroscopic HR histograms in the same format as

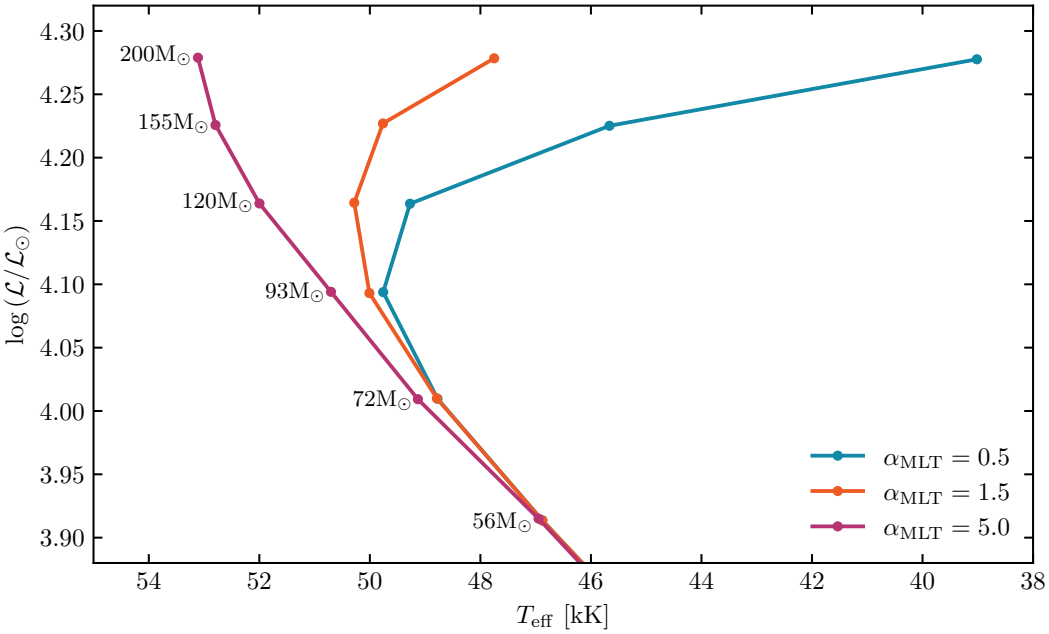

Figure 5.10: The ZAMS lines from Figure 5.9, magnified to only show the region where the different mixing length parameters have an effect.

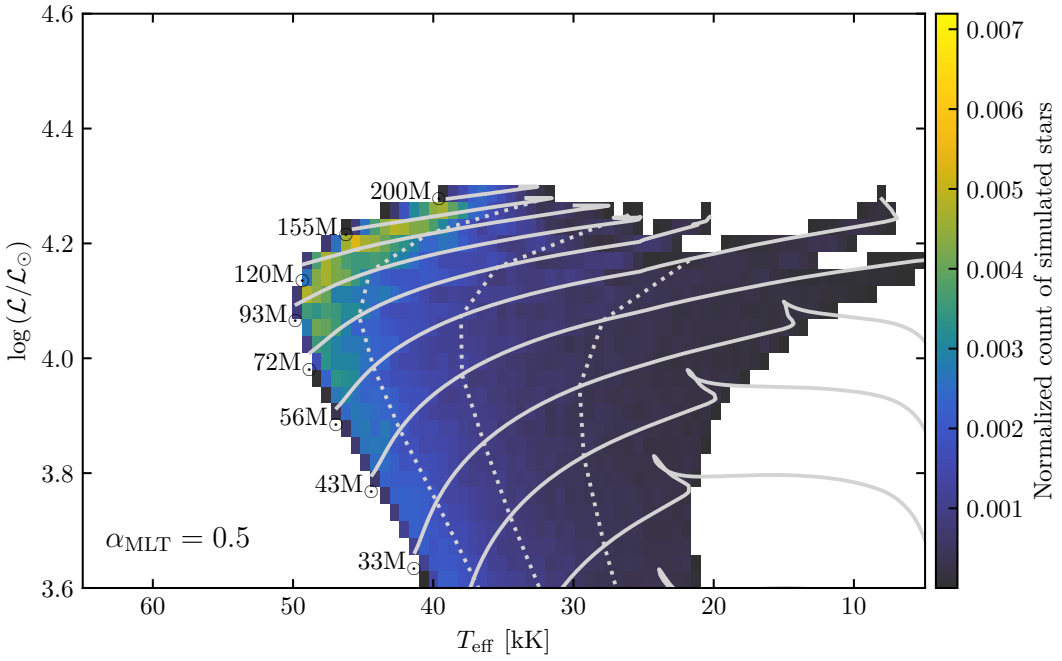

(a) The $\alpha_{0.5}$ population of 271 628 simulated stars, shown in a spectroscopic HR diagram.

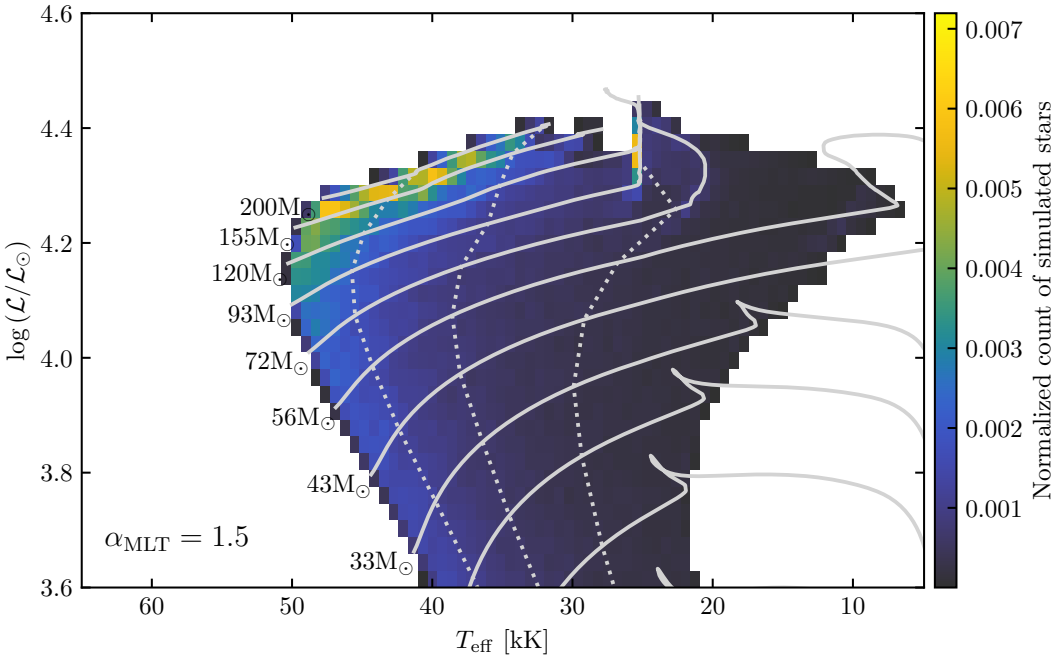

(b) The $\alpha_{1.5}$ population of 401 970 simulated stars, shown in the spectroscopic HR diagram.

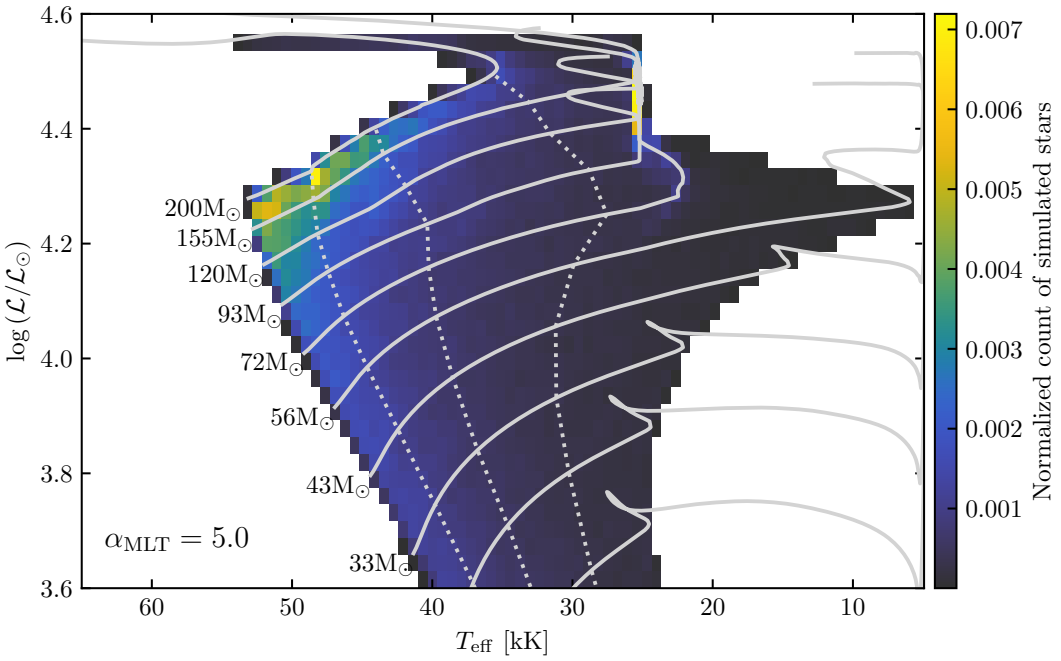

(c) The $\alpha_{5.0}$ population of 460 035 simulated stars, shown in the spectroscopic HR diagram.

Figure 5.11: The $\alpha_{0.5}$, $\alpha_{1.5}$, and $\alpha_{5.0}$ populations, each shown in a spectroscopic HR histogram in the same format as Figure 5.4, normalized so that the pixel counts sum to one. The MESA grid evolutionary tracks are plotted as solid gray lines. The vertical dotted gray lines divide the MS into quarters as described previously.

Figure 5.4. The three plots have the same boundaries and colorbar scales. The most immediate difference is how the ZAMS line bends redward for the $\alpha_{0.5}$ and $\alpha_{1.5}$ populations, the same as in the models. The number of simulated stars in each population also increases with $\alpha_{\rm MLT}$ value, with the $\alpha_{5.0}$ population having almost twice as many simulated stars as the $\alpha_{0.5}$ population. This is due to the same reason discussed earlier for the MESA grids, namely the early termination of some high mass-low $\alpha_{\rm MLT}$ models. As in Figure 5.4, the luminosity-mass relation and some overlapping evolutionary tracks causes an increase in density of simulated stars with high initial masses, even though the number of these stars is less than that those with lower initial masses.

Chapter 6

Spindown in IACOB and simulated stars

We compared the projected rotational velocity of the IACOB stars and two Brott populations by dividing the data into mass bins and quarters of the MS, as discussed earlier. The IACOB stars do not have initial mass estimates and naturally we do not know the center abundances. Therefore, we estimated these values by comparing the location of the IACOB stars to the Brott grid tracks with $v_i = 200\,\mathrm{km\,s^{-1}}$. As previously mentioned, the spectroscopic HR diagram of the IACOB stars has some unpopulated areas, namely the ZAMS line above $40\,\mathrm{M_\odot}$ and the second half of the MS for stars below $9\,\mathrm{M_\odot}$. Therefore, we do not look at the full MS for all the mass ranges considered.

6.1 Single initial rotational velocity

As discussed in Section 4, the IACOB sample is not complete for B-type stars, which is why we only look at the first two quarters of the MS for the $7\,\mathrm{M_\odot}$ to $9\,\mathrm{M_\odot}$ bin, seen in Figure 6.1. These first two quarters already only have the equivalent of ∼10 stars each, and the third and fourth quarters have ∼2 and 0 stars, respectively. The simulated stars do not undergo any significant spindown between the first and second quarter of the MS and neither do the IACOB stars. Most of the IACOB stars are slow-rotators, while the opposite is true for the simulated stars. Figure 4.2 shows a tail of rapidly rotating stars with $v \sin i$ values up to $\sim 450\,\mathrm{km\,s^{-1}}$, but this mass range does not have any IACOB stars with $v \sin i \gtrsim 320\,\mathrm{km\,s^{-1}}$.

There are more IACOB stars present in the $9\,\mathrm{M_\odot}$ to $30\,\mathrm{M_\odot}$ bin, so we are able to consider the full MS, which is shown in Figure 6.2. The IACOB stars in the first quarter of the MS are concentrated at low $v \sin i$ values, as the distribution peaks between $0\,\mathrm{km\,s^{-1}}$ to $40\,\mathrm{km\,s^{-1}}$. These stars do not appear to have a bimodal distribution, but some stars in this quarter reach velocities of $\sim 450\,\mathrm{km\,s^{-1}}$, well above the maximum value of $\sim 300\,\mathrm{km\,s^{-1}}$ seen in Figure 6.1. The simulated stars in this quarter have experienced almost no spindown, so their distribution has a sharp peak at v_{ZAMS}. The IACOB stars' distribution is less extreme in the second quarter of the MS, and there are more stars with $v \sin i$ values around $\sim 100\,\mathrm{km\,s^{-1}}$. A weak second peak is visible at $\sim 200\,\mathrm{km\,s^{-1}}$ and the fast moving tail extends out to

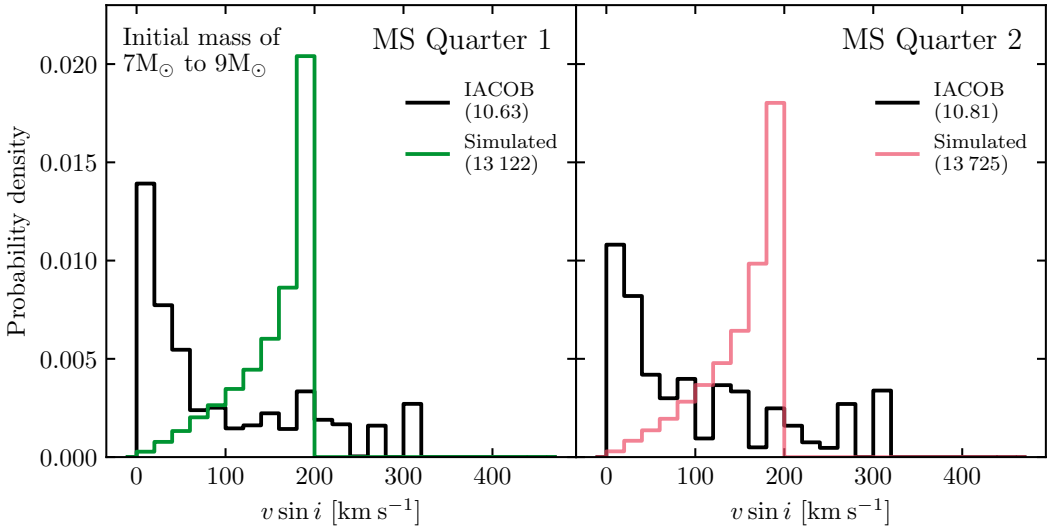

Figure 6.1: The distribution of projected rotational velocity, $v \sin i$, for the IACOB stars and the Brott single $v_{\rm ZAMS}$ population. The simulated stars have an initial mass of $7\,M_\odot$ to $9\,M_\odot$ and are divided by core hydrogen mass fraction. The IACOB stars are selected by location on the spectroscopic HR diagram. The numbers indicate the number of stars or simulated stars that the data is drawn from.

$\sim$440 km s^{-1}. The simulated stars do not have a noticeable change between quarters, as they are too low mass to experience substantial spindown. In the third quarter of the MS the simulated stars show some spindown, although the distribution still peaks at $v_{\rm ZAMS}$. The IACOB stars' distribution shows a slightly lower peak. The IACOB stars in the fourth quarter of the MS have a tall and narrow peak similar to those seen in the first two quarters, but this peak is from 20 km s^{-1} to 60 km s^{-1}, so there are fewer slow rotators. The second peak has disappeared and the number of IACOB stars per bin reduces gradually until a maximum $v \sin i$ of $\sim$450 km s^{-1}. The simulated stars experience more spindown, but the fact that the majority of the simulated stars still have $v \sin i$ values above 140 km s^{-1} shows that most of the spindown in this mass range occurs after the TAMS. The IACOB stars are similar, as the maximum $v \sin i$ stays above 400 km s^{-1}, regardless of MS quarter.

While the $30\,M_\odot$ to $50\,M_\odot$ bin only contains $\sim$9 IACOB stars in the first quarter of the MS, we still consider all four quarters, shown in Figure 6.3. The IACOB stars in the first quarter of the MS appear to have a bimodal distribution, but as this data is equivalent to only $\sim$9 stars, it is likely to be small number statistics. The distribution of simulated stars peaks at their $v_{\rm ZAMS}$ velocity, while the IACOB stars are mostly slow rotators with a fast tail extending out to $\sim$450 km s^{-1}. There are more IACOB stars present in the second quarter of the MS, and we can see that the distribution of rapid rotators has become smoother. The fast tail is still present, however, even though the simulated stars have begun to spin down. By the third

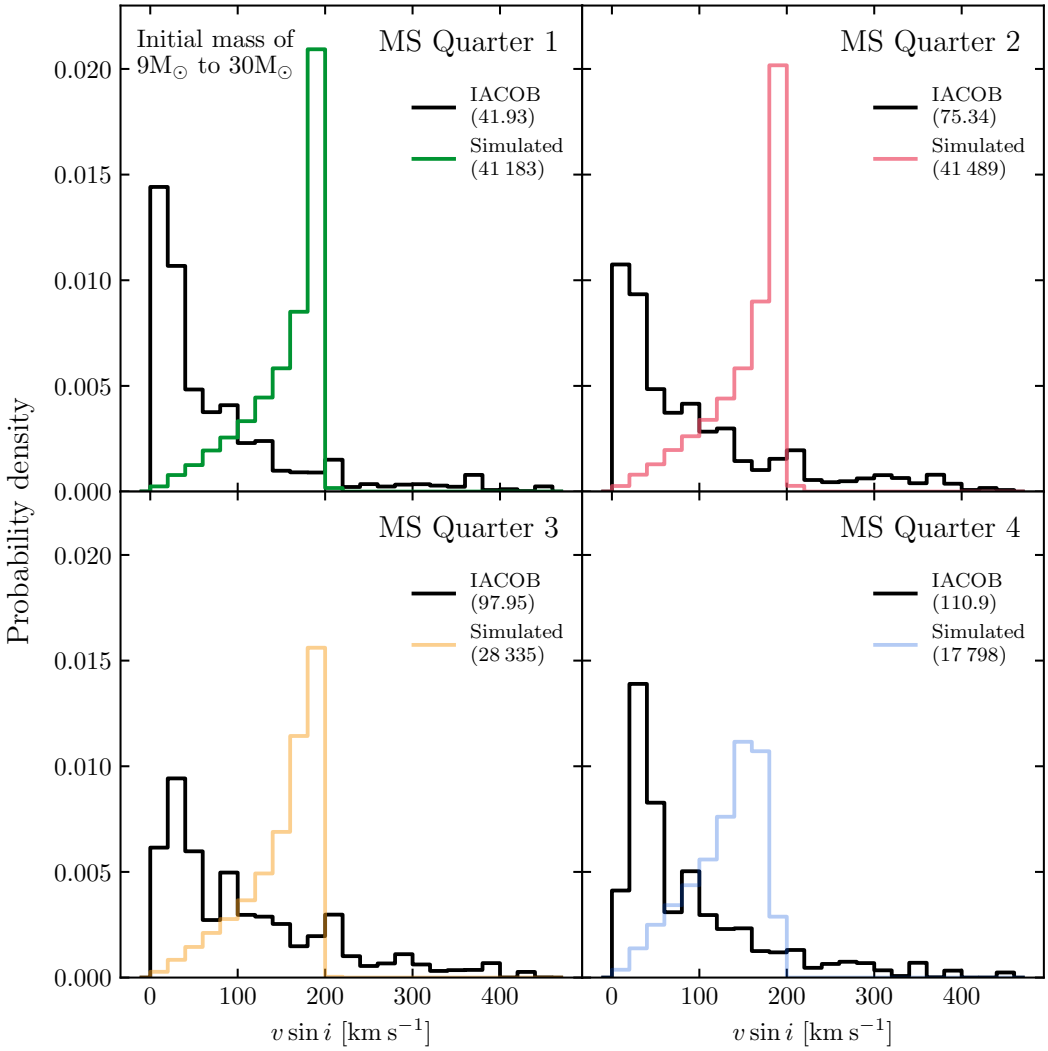

Figure 6.2: Distribution of projected rotational velocity for the IACOB stars and the Brott single v_{ZAMS} population, in the same format as Figure 6.1, except across all four quarters of the MS with an initial mass range of $9\,\mathrm{M}_\odot$ to $30\,\mathrm{M}_\odot$.

quarter of the MS, the simulated stars show clear signs of spindown, with the peak of the distribution moving to slower velocities. The IACOB stars, however, are still rotating rapidly, and the fast tail is still present. The percentage of IACOB stars with $v \sin i < 80\,\mathrm{km\,s^{-1}}$ has increased from ∼70 % to ∼80 % between the first and fourth quarters, which does show that some limited spindown does take place in the last quarter of the MS. Despite this, there are still some stars with velocities up to $\sim 360\,\mathrm{km\,s^{-1}}$. The simulated stars show strong spindown in the fourth quarter of the MS, with many already completely spun down. Overall, we can see that the IACOB stars experience very limited spindown, while the simulated stars slowly lose velocity

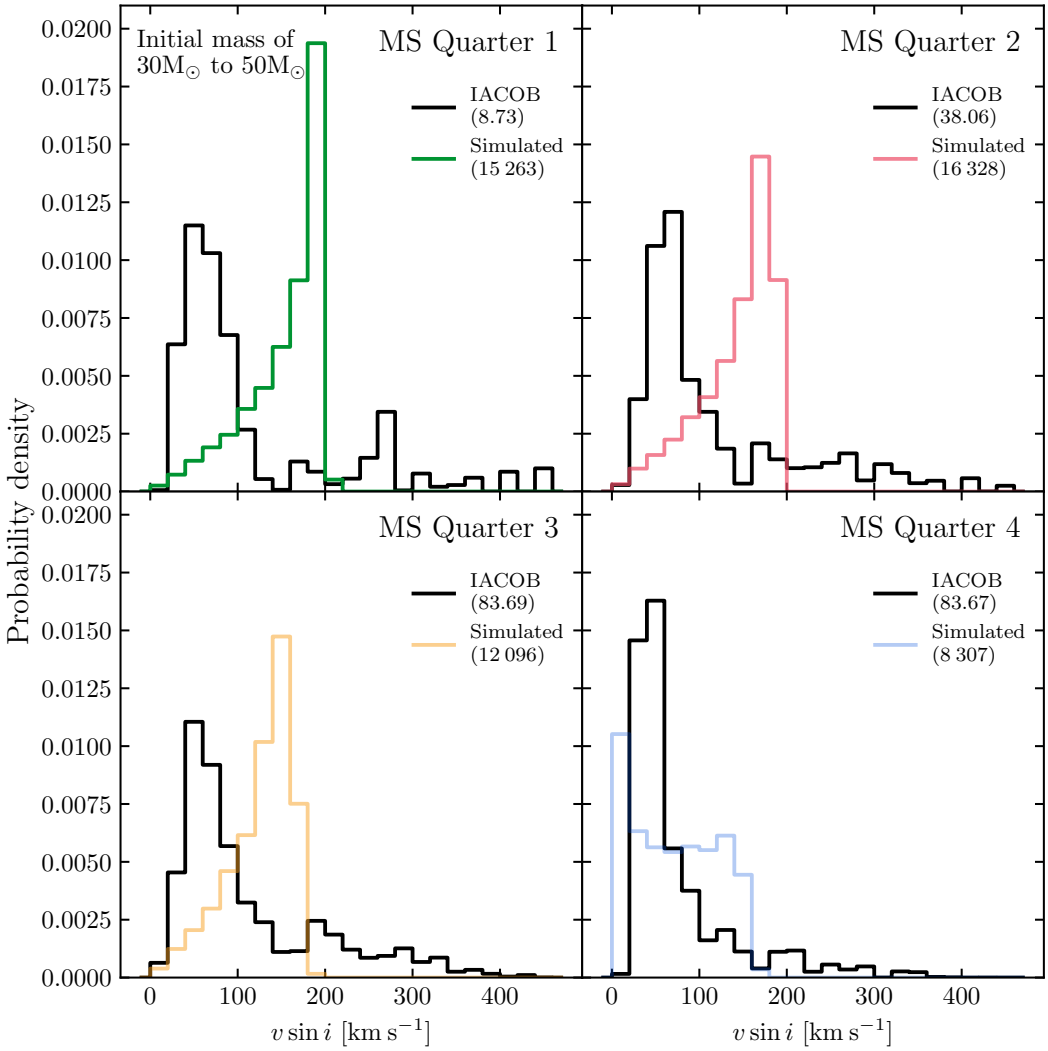

Figure 6.3: Distribution of projected rotational velocity for the IACOB stars and the Brott single v_{ZAMS} population, in the same format as Figure 6.1, except across all four quarters of the MS with an initial mass range of 30 $\mathrm{M}_{\odot}$ to 50 $\mathrm{M}_{\odot}$.

as expected.

Above 50 $\mathrm{M}_{\odot}$, the IACOB stars veer away from the ZAMS line (Holgado et al., 2020), so Figure 6.4 omits the first quarter of the MS. Simulated stars in the second quarter of the MS are already spinning down, but the distribution still peaks close to v_{ZAMS}. While most of the IACOB stars in this quarter have $v \sin i < 150\,\mathrm{km\,s^{-1}}$, there are stars with $v \sin i$ up to $\sim$350 $\mathrm{km\,s^{-1}}$. This is a higher maximum $v \sin i$ than seen in the 7 $\mathrm{M}_{\odot}$ to 9 $\mathrm{M}_{\odot}$, but still lower than the $\sim$450 $\mathrm{km\,s^{-1}}$ seen in the 30 $\mathrm{M}_{\odot}$ to 50 $\mathrm{M}_{\odot}$ bin. This tail of rapid rotators is still present in the third quarter of the MS,

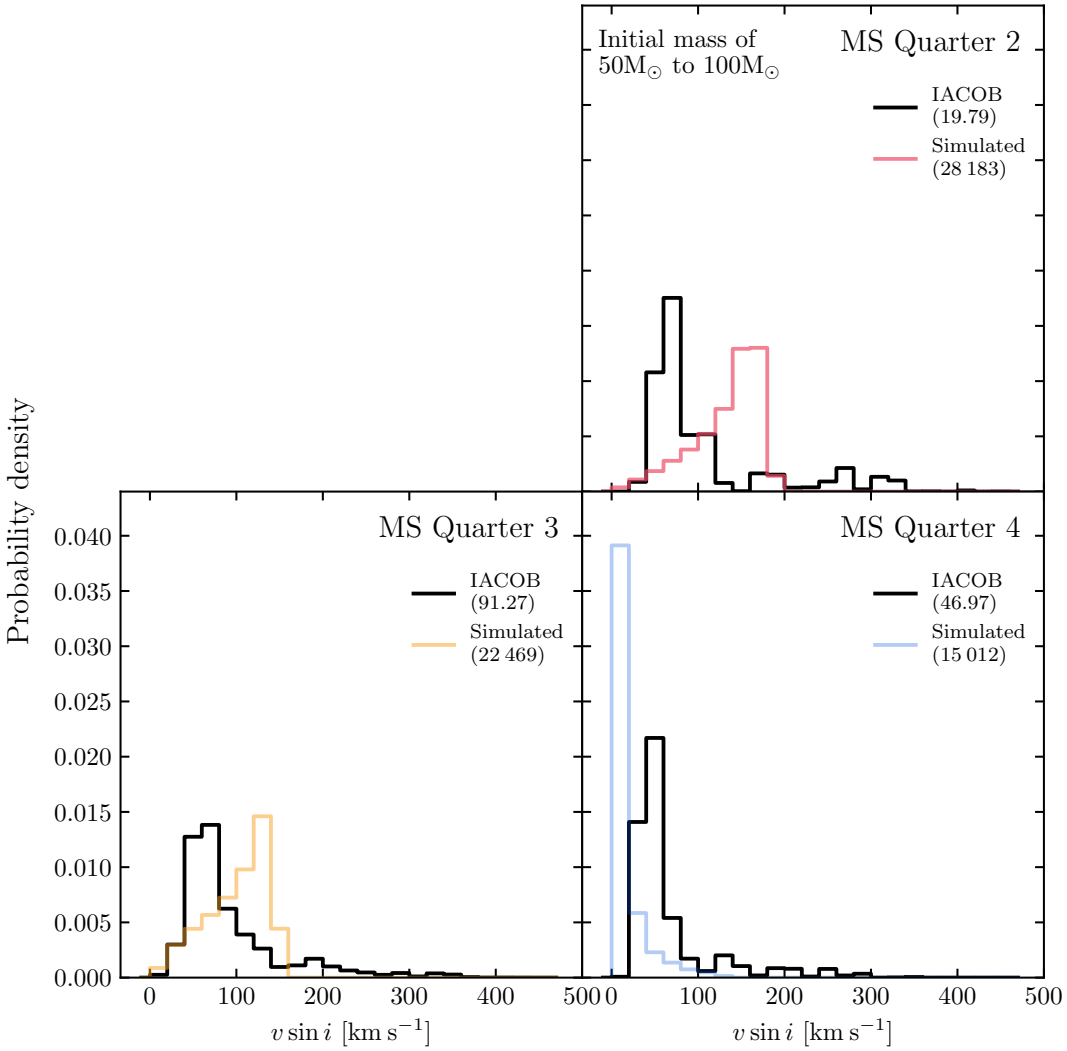

Figure 6.4: Distribution of projected rotational velocity for the IACOB stars and the Brott single v_{ZAMS} population, in the same format as Figure 6.1, except with an initial mass range of $50\,\mathrm{M}_\odot$ to $100\,\mathrm{M}_\odot$ and for the last three quarters of the MS.

although more of the IACOB stars have shifted to lower $v \sin i$ values. The simulated stars have also spun down, but there is still a gap of $\sim$40 km s^{-1} between the peaks of the two distributions. In the fourth quarter of the MS, however, the simulated stars are nearly all completely spun down, while the IACOB stars are still clustered at $\sim$50 km s^{-1}. The fast tail has reduced as well, with the maximum value now at $\sim$300 km s^{-1}, which is 20 km s^{-1} less than in Figure 6.1.

6.2 Distribution of initial rotational velocities

We discussed the characteristics of the IACOB distributions in Section 6.1, so this section will focus on the distributions of the simulated stars and their similarity to the IACOB distributions.

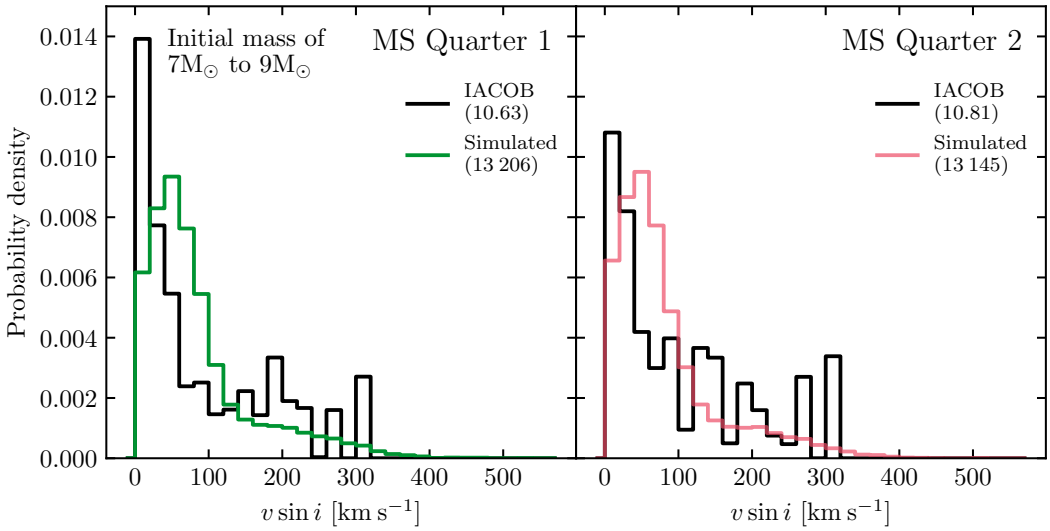

Figure 6.5: The distribution of projected rotational velocity, $v \sin i$, for the IACOB stars and the Brott distribution v_{ZAMS} population, in the same format as Figure 6.1. The initial mass range is $7\,\mathrm{M}_\odot$ to $9\,\mathrm{M}_\odot$ and the first half of the MS is shown.

Figure 6.5 shows the first two quarters of the MS for the IACOB and simulated stars in the mass range $7\,\mathrm{M}_\odot$ to $9\,\mathrm{M}_\odot$. Neither of them experience spindown in the first half of the MS. As noted before, the IACOB stars in this mass range have a maximum $v \sin i$ of $\sim$320 km s^{-1}, but the simulated stars go up to $\sim$530 km s^{-1}. While both the IACOB and simulated stars are concentrated below $\sim$100 km s^{-1}, the simulated stars still have a faster average $v \sin i$.

Figure 6.6 shows all four quarters of the MS for the mass range $9\,\mathrm{M}_\odot$ to $30\,\mathrm{M}_\odot$. Below $\sim$140 km s^{-1} the simulated stars show good agreement with IACOB across all four quarters. Although the peaks of the simulated stars' distributions are consistently lower than those of the IACOB stars, the structure is similar. The simulated star distributions change negligibly in the first three quarters of the MS, but there is spindown present in the last quarter. The maximum $v \sin i$ has also reduced to $\sim$300 km s^{-1}, from a maximum of over 400 km s^{-1} in the first quarter. The peaks of the IACOB stars' distributions shift slightly to faster velocities across the MS and the maximum $v \sin i$ stays constant at $\sim$450 km s^{-1}. We can see that the simulated stars are unable to replicate the fast moving tail in the IACOB distribution, which consistently stays at $\sim$450 km s^{-1}. Spindown clearly affects the simulated stars, while

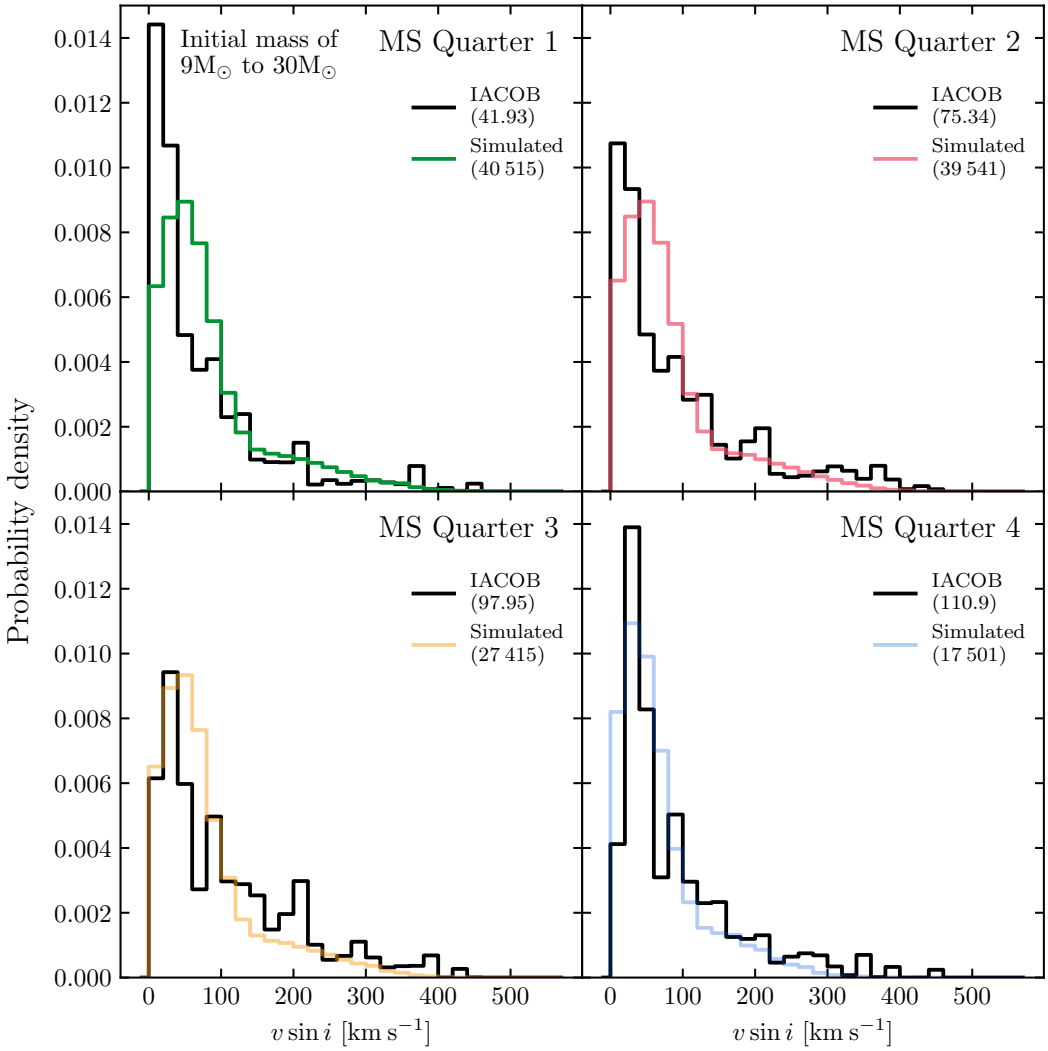

Figure 6.6: Distribution of projected rotational velocity for the IACOB stars and the Brott distribution v_{ZAMS} population, in the same format as Figure 6.1, except across all four quarters of the MS with an initial mass range of $9\,\mathrm{M}_\odot$ to $30\,\mathrm{M}_\odot$.

the IACOB stars seem to be affected only weakly, if at all.

Figure 6.7 shows the IACOB and simulated stars within the mass range $30\,\mathrm{M}_\odot$ to $50\,\mathrm{M}_\odot$. Across all quarters of the MS, the distributions of the IACOB and simulated stars with $v \sin i \lesssim 150\,\mathrm{km\,s^{-1}}$ are very similar, but the simulated stars are not able to reproduce the IACOB stars' second peak at $\sim$180 $\mathrm{km\,s^{-1}}$. In addition, the simulated stars' maximum $v \sin i$ is consistently lower than that of the IACOB stars. From the beginning, there are simulated stars with $v \sin i$ values near zero, and the simulated stars spin down throughout the MS. By the fourth quarter, none of the simulated

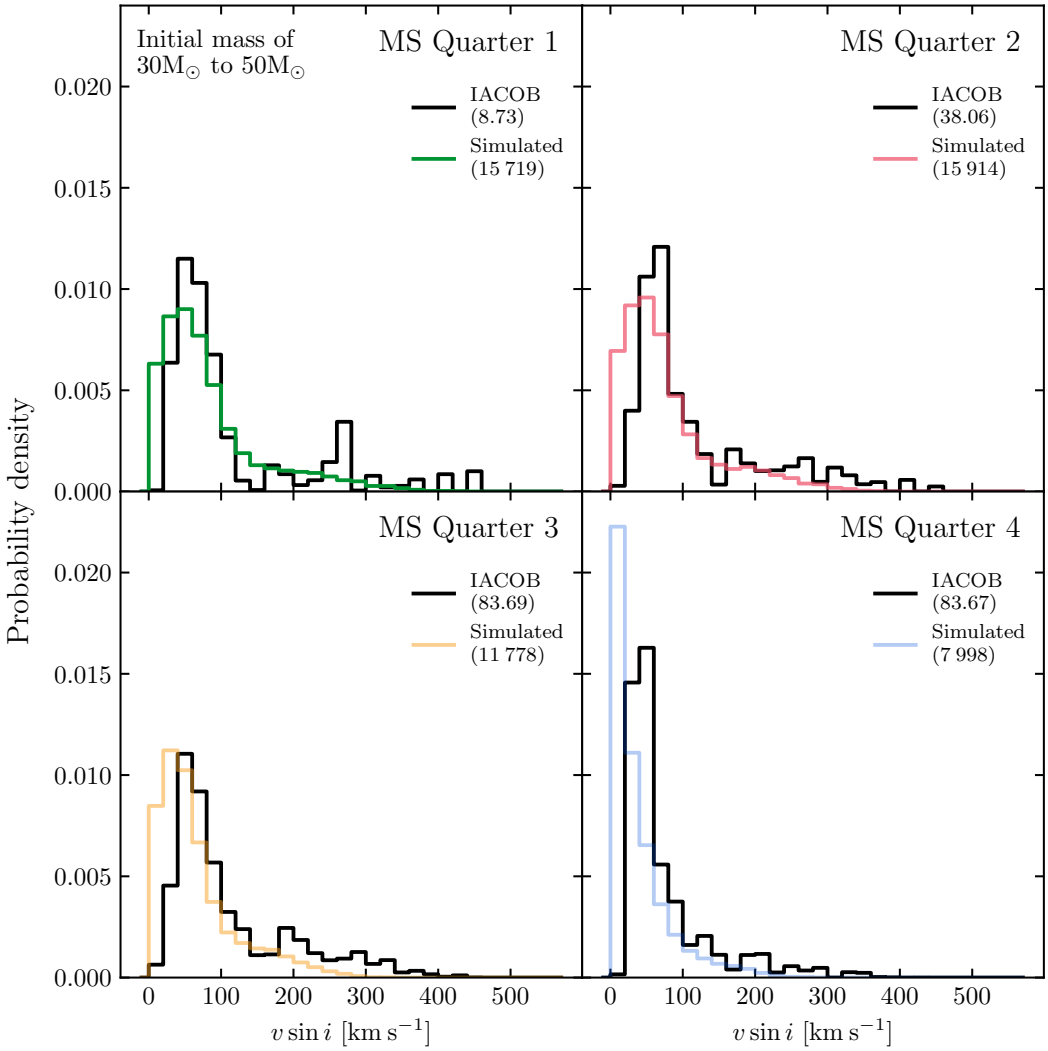

Figure 6.7: The distribution of projected rotational velocity, $v \sin i$, for the IACOB stars and the Brott distribution v_{ZAMS} population, in the same format as Figure 6.1. The initial mass range is $30\,\mathrm{M}_\odot$ to $50\,\mathrm{M}_\odot$ and the whole MS is shown.

stars have $v \sin i \gtrsim 300\,\mathrm{km\,s^{-1}}$ and $\sim$75 % have $v \sin i \lesssim 50\,\mathrm{km\,s^{-1}}$. The IACOB stars do not show this behavior, with only $\sim$15 % of stars ever reaching velocities below $\sim$20 $\mathrm{km\,s^{-1}}$. Contrary to the previous mass bins, the distributions of simulated stars consistently predict more slow rotators than seen in the IACOB distributions.

The last mass range, $50\,\mathrm{M}_\odot$ to $100\,\mathrm{M}_\odot$, is shown in Figure 6.8. These simulated stars experience strong spindown early on and they are consistently slower than the IACOB stars. The distributions for the simulated stars both peak at and extend to lower velocities than the IACOB stars, continuing what we saw in Figure 6.7.

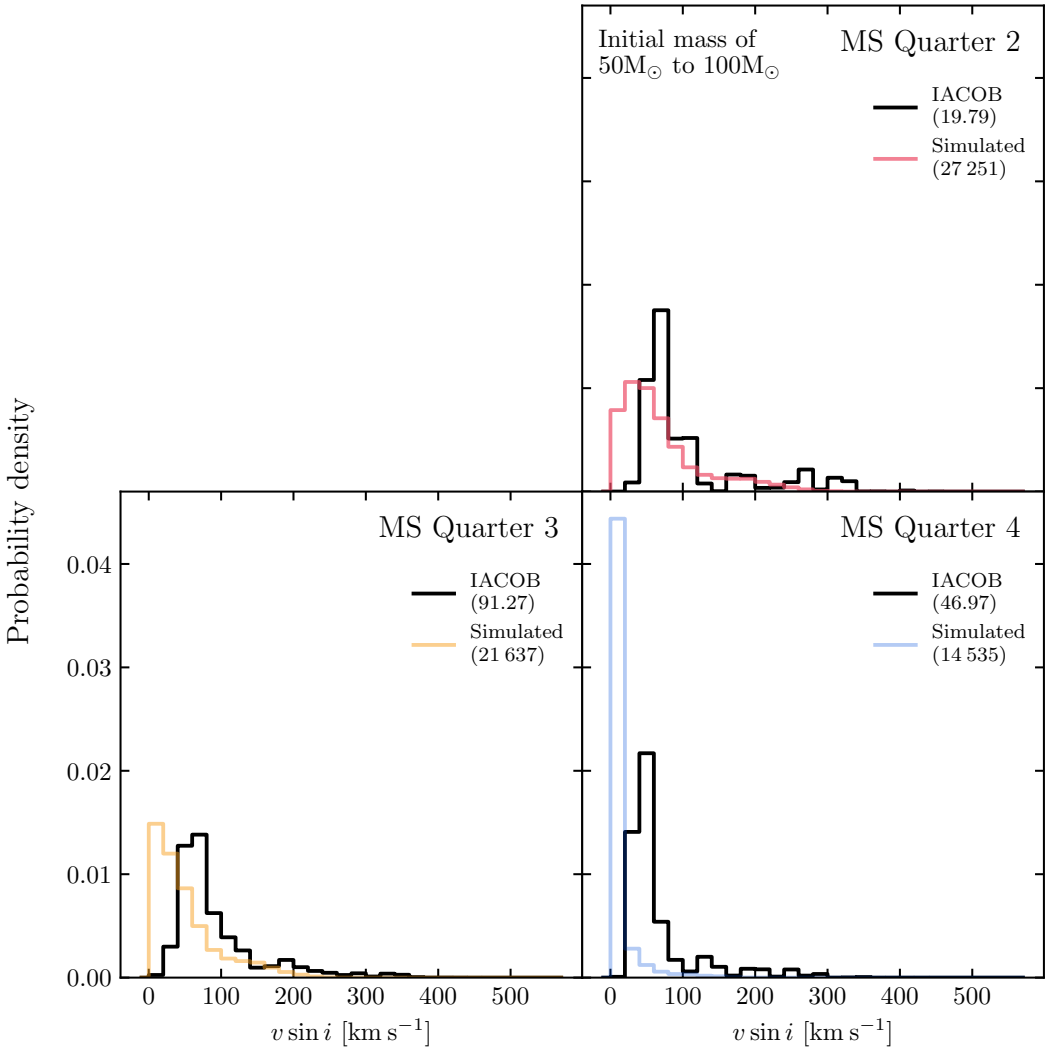

Figure 6.8: The distribution of projected rotational velocity, $v \sin i$, for the IACOB stars and the Brott distribution v_{ZAMS} population, in the same format as Figure 6.1. The initial mass range is 50 $\mathrm{M}_\odot$ to 100 $\mathrm{M}_\odot$ and the figure shows the last three quarters of the MS.

The difference is most pronounced in the fourth quarter of the MS, where ∼90 % of the simulated stars have spun down below 20 $\mathrm{km\,s^{-1}}$ and none have a $v \sin i$ above ∼200 $\mathrm{km\,s^{-1}}$. The distribution of IACOB stars, however, peaks at ∼60 $\mathrm{km\,s^{-1}}$. The tail of the IACOB distribution extends out to ∼300 $\mathrm{km\,s^{-1}}$, which is only slightly less the maximum values in the second and third quarter, which were ∼340 $\mathrm{km\,s^{-1}}$ and ∼360 $\mathrm{km\,s^{-1}}$, respectively.

From this, we can conclude that the location of the peak in the IACOB projected rotational velocity distributions seems to be moving to more rapid velocities as mass

increases. We can also see that the simulated stars have much stronger spindown and the IACOB stars in our sample do not show a strong braking mechanism, especially for high mass stars in the second half of the MS.

Chapter 7

Inflation effects in IACOB and simulated stars

We looked for possible inflation in the IACOB stars by comparing the distributions of effective temperature between the three $\alpha_{\rm MLT}$ populations and the IACOB sample. We used the procedure outlined in Section 3.3, using distributions taken from a luminosity range with width $10^{0.1}\mathcal{L}_{\odot}$ to calculate the bias factor, which we then applied to the distribution from the next highest luminosity range. E.g., we calculated a bias factor from the $10^{3.9}\mathcal{L}_{\odot}$ to $10^{4.0}\mathcal{L}_{\odot}$ distribution and applied it to the $10^{4.0}\mathcal{L}_{\odot}$ to $10^{4.1}\mathcal{L}_{\odot}$ distribution. We also overlapped the ranges to ensure that all areas of the spectroscopic HR diagram were covered. Following from our previous example, this means that the original $10^{4.0}\mathcal{L}_{\odot}$ to $10^{4.1}\mathcal{L}_{\odot}$ distribution was then used to calculate a bias factor for the $10^{4.1}\mathcal{L}_{\odot}$ to $10^{4.2}\mathcal{L}_{\odot}$ distribution. While some of the IACOB stars are clearly well past the TAMS, the simulated stars are all on the MS. Despite this, IACOB stars across the full width of the spectroscopic HR diagram are considered, even those off the MS.

The figures are formatted with the lower half of the spectroscopic luminosity range on the left, and the upper half on the right. This right half of the plot is divided in two, with the unaltered distribution on top and the distribution with bias factor applied on the bottom. Overall, we can see that the simulated star distributions peak at hot temperatures and then decrease, as there are more simulated stars at the ZAMS than the TAMS. The IACOB distributions do not show the same behavior and are more centrally peaked, reflecting the fact that there are no IACOB stars near the ZAMS above $10^{3.7}\mathcal{L}_{\odot}$.

Spectroscopic luminosity range $10^{3.7}\mathcal{L}_{\odot}$ to $10^{3.9}\mathcal{L}_{\odot}$

In the first two spectroscopic luminosity ranges, $10^{3.7}\mathcal{L}_{\odot}$ to $10^{3.8}\mathcal{L}_{\odot}$ and $10^{3.8}\mathcal{L}_{\odot}$ to $10^{3.9}\mathcal{L}_{\odot}$, we expect to only see slight differences between the three $\alpha_{\rm MLT}$ populations, because inflation effects here are small and not seen until the TAMS. The distributions in Figure 7.1 agree with this, as the only difference seen between the $\alpha_{\rm MLT}$ populations is a slightly hotter TAMS point for the $\alpha_{5.0}$ population, which is not due to inflation effects. The unaltered distributions of the simulated stars are strongly peaked at $\sim$40 kK, while the IACOB distributions are flatter without a strong peak. The effect is magnified at the $\log(\mathcal{L}/\mathcal{L}_{\odot}) = 3.8$ to 3.9 range, which has a very flat distribution

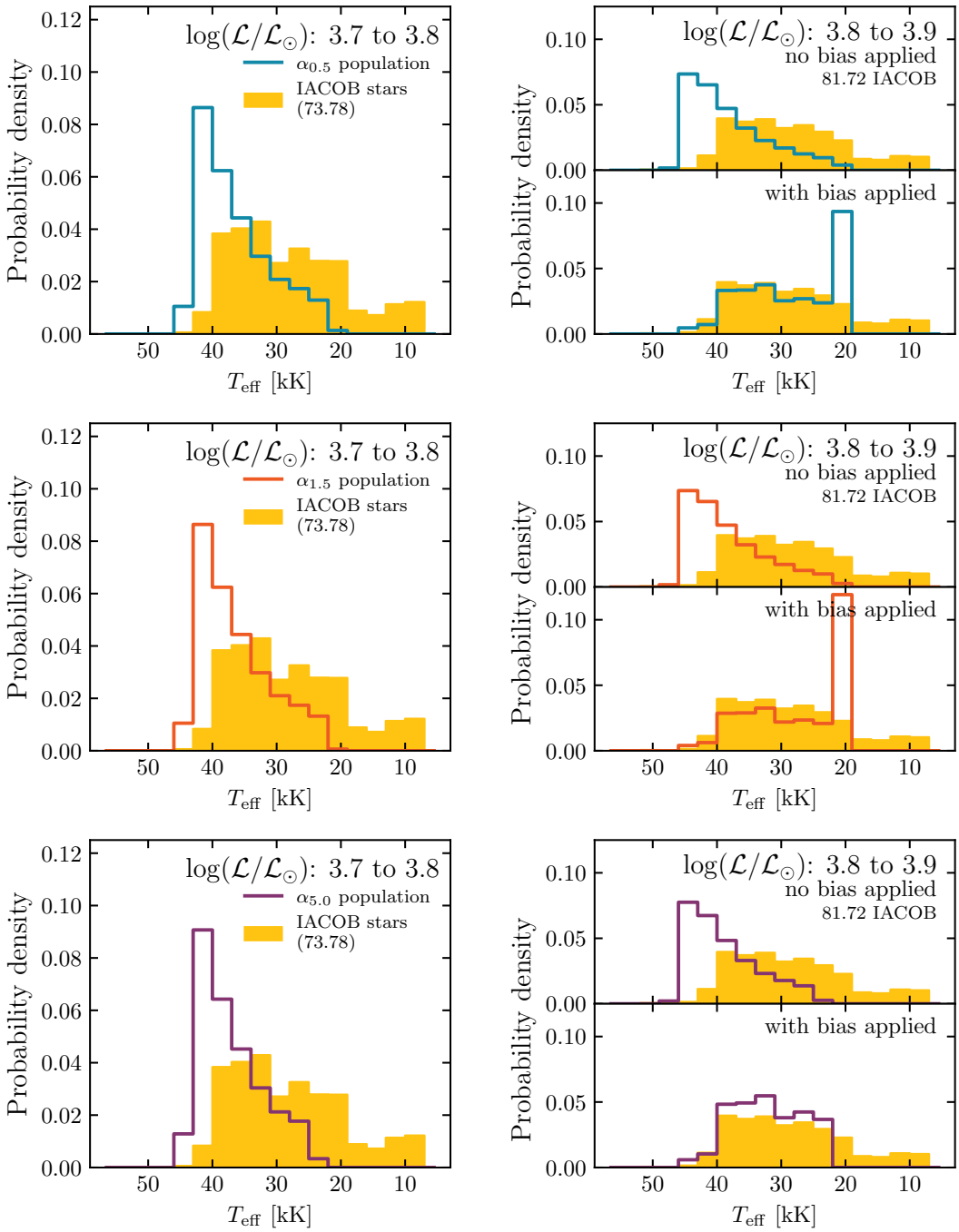

Figure 7.1: Distributions of effective temperature at a fixed spectroscopic luminosity range for the IACOB stars and $\alpha_{\rm MLT}$ populations. The distributions for the range $10^{3.7}\mathcal{L}_\odot$ to $10^{3.8}\mathcal{L}_\odot$ are in the left panel of each figure. The right panel has the distributions for the range $10^{3.8}\mathcal{L}_\odot$ to $10^{3.9}\mathcal{L}_\odot$, with the unaltered distributions on the top and the same IACOB distribution with the simulated star distribution with bias factor on the bottom. The distributions are normalized to have an integral equal to one.

of IACOB effective temperatures. Compared to the simulated stars, the IACOB distribution is shifted to cooler temperatures.

Between $\log(\mathcal{L}/\mathcal{L}_\odot) = 3.7$ and 3.8 the IACOB distribution has three clear portions, each without a clear peak: one from ∼40 kK to ∼30 kK, a second from ∼30 kK to ∼18 kK, and a third from ∼18 kK to ∼5 kK. The distribution flattens out in the $\log(\mathcal{L}/\mathcal{L}_\odot) = 3.8$ to 3.9 range and the ∼40 kK to ∼30 kK and ∼30 kK to ∼18 kK areas have merged together.

Since the simulated star distributions used to calculate the bias factor are very similar, the distributions with an applied bias factor are also very similar. All three altered simulated star distributions shift to become very flat with two groups, as seen in the IACOB distribution. The difference we do see is that the bin at ∼20 kK for the $\alpha_{0.5}$ and $\alpha_{1.5}$ distributions is abnormally tall, while this bin has an amplitude of zero for the $\alpha_{5.0}$ distribution. This is due to the fact that we do not have any post-MS simulated stars, and this effective temperature bin is on the very edge of the MS, meaning it has very few simulated stars in the $10^{3.7}\mathcal{L}_\odot$ to $10^{3.8}\mathcal{L}_\odot$ range. The IACOB stars, however, extend across the full temperature range, so the difference in bin amplitude between the simulated and IACOB stars is large. This leads to a bigger bias factor, so that even a bin with a very low amplitude in the unaltered distribution can become very tall once the bias factor is applied. E.g., for the $\alpha_{0.5}$ simulated stars, this bin has a height of 0.0014 in the $10^{3.7}\mathcal{L}_\odot$ to $10^{3.8}\mathcal{L}_\odot$ bin, while for the IACOB stars it has a height of 0.0278. The bias factor for this bin is therefore 19.9, which is an order of magnitude greater than the next smallest bias factor, which is only 2.2. As stated before, the $\alpha_{5.0}$ simulated stars have a hotter TAMS point, so the bin is empty and therefore has a bias factor of zero, which is why we do not see an abnormally tall bin in the altered distribution.

Spectroscopic luminosity range $10^{3.8}\mathcal{L}_\odot$ to $10^{4.0}\mathcal{L}_\odot$

The next set of spectroscopic luminosity ranges, $10^{3.8}\mathcal{L}_\odot$ to $10^{3.9}\mathcal{L}_\odot$ and $10^{3.9}\mathcal{L}_\odot$ to $10^{4.0}\mathcal{L}_\odot$, also cover a range without strong inflation effects. We can see this in Figure 7.2, which again shows only negligible differences between the unaltered distributions of the different simulated star populations for both spectroscopic luminosity ranges, namely a slightly hotter TAMS point for the $\alpha_{5.0}$ simulated stars.

The IACOB distribution for the $10^{3.9}\mathcal{L}_\odot$ to $10^{4.0}\mathcal{L}_\odot$ range has become flatter, although it still can be clearly divided into two groups. The first group ranges from ∼45 kK to ∼18 kK, and the second is a tail that extends out to ∼7 kK. Again, this does not match the simulated stars' distributions, which are peaked at high temperatures and decrease smoothly.

The altered distributions of the simulated stars are again very similar, except for the abnormally tall bin height for the $\alpha_{5.0}$ simulated stars at ∼22 kK. As previously, this is due to our MS-only simulated star populations. Overall, the altered distributions

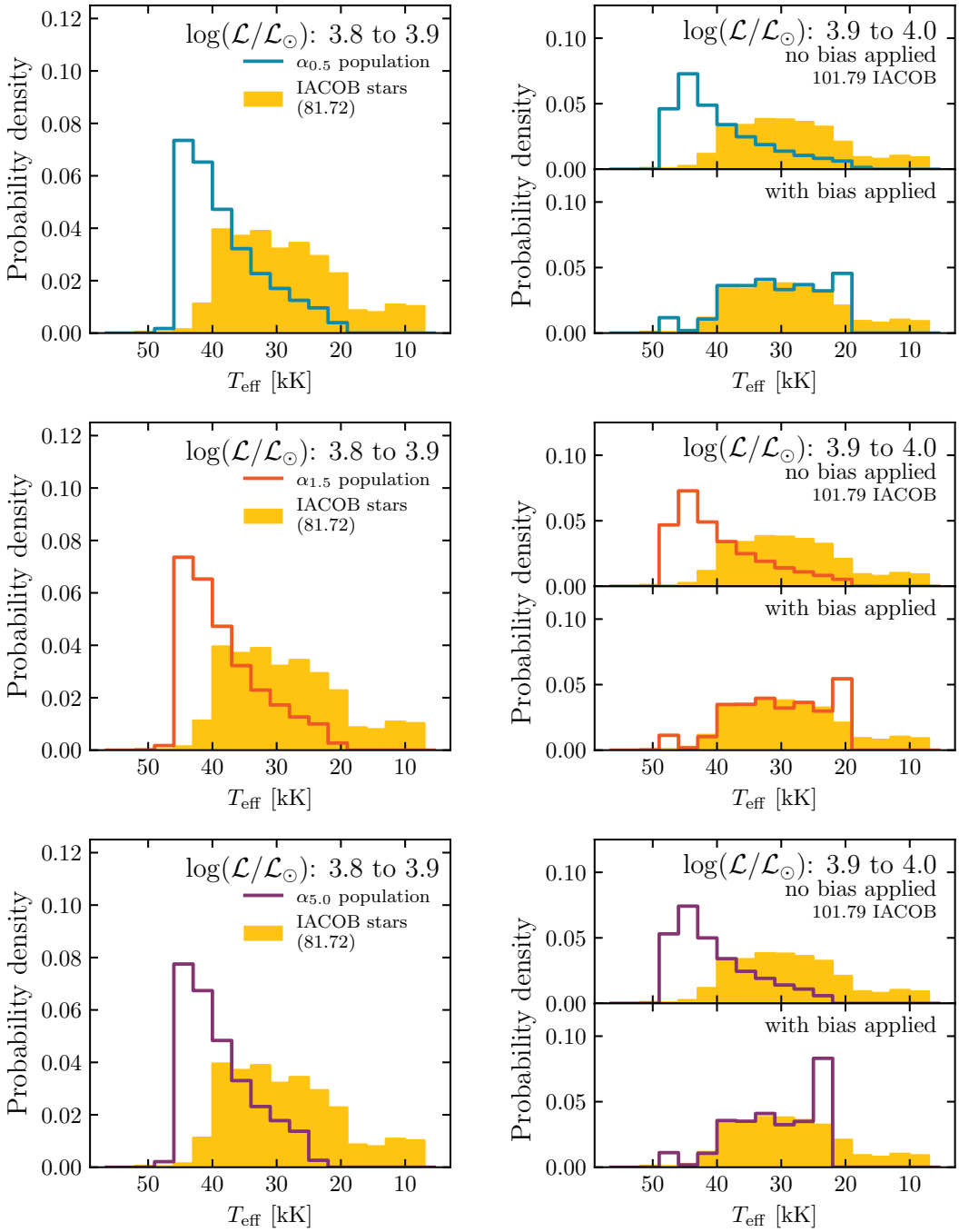

Figure 7.2: Distributions of the effective temperature at a fixed spectroscopic luminosity range for the IACOB stars and the three $\alpha_{\rm MLT}$ populations, in the same format as Figure 7.1. The distributions are for the spectroscopic luminosity range $10^{3.8}\mathcal{L}_\odot$ to $10^{4.0}\mathcal{L}_\odot$.

replicate the IACOB distribution from ∼45 kK to ∼22 kK, but then fail to match the decrease in height at cooler temperatures. The application of the bias factor is also unable to sufficiently reduce the height of the bins for temperatures hotter than ∼45 kK. The $\alpha_{0.5}$ and $\alpha_{1.5}$ distributions end at ∼18 kK, which is the end of the first group in the IACOB distribution, but the $\alpha_{5.0}$ distribution cuts off at ∼22 kK, reflecting the hotter TAMS point.

Spectroscopic luminosity range $10^{3.9}\mathcal{L}_\odot$ to $10^{4.1}\mathcal{L}_\odot$

Figure 7.3 shows the first spectroscopic luminosity range where we can expect to see a change in the ZAMS point between the simulated star populations. Accordingly, the height of the bin at ∼50 kK for the $10^{4.0}\mathcal{L}_\odot$ to $10^{4.1}\mathcal{L}_\odot$ range increases with the α_{MLT} value, as the ZAMS line of the $\alpha_{0.5}$ and $\alpha_{1.5}$ populations is beginning to shift to cooler temperatures.

The IACOB stars in the $10^{4.0}\mathcal{L}_\odot$ to $10^{4.1}\mathcal{L}_\odot$ range no longer have a flat distribution, instead shifting to a pyramid shape with a central peak at ∼30 kK. There is still a clearly separate tail from ∼18 kK to ∼7 kK, which is beyond the effective temperature range covered by the simulated stars. This centrally peaked distribution is difficult for the simulated stars to replicate, and the altered distributions shift to become flat, rather than moving the peak to the center.

The altered $\alpha_{0.5}$ distribution replicates the IACOB distribution most successfully, although it still cannot reproduce the slope on either side of the broad IACOB peak. It also predicts more stars in the ∼18 kK bin, which is due to the previously stated issue with binning on the edge of the MS. While this binning issue only causes a slight abnormality for the altered $\alpha_{0.5}$ distribution, it distorts the altered $\alpha_{1.5}$ distribution entirely, and the bin has a height of 0.18, an order of magnitude taller than any other in the distribution. Even ignoring this effect, we can see that the shape of the altered $\alpha_{1.5}$ distribution is too flat, regardless of overall amplitude. The altered $\alpha_{5.0}$ distribution is even flatter and is completely unable to replicate the shape or extent of the IACOB distribution.

Spectroscopic luminosity range $10^{4.0}\mathcal{L}_\odot$ to $10^{4.2}\mathcal{L}_\odot$

The differences between the simulated star populations grow as we increase in spectroscopic luminosity, and the unaltered distributions for the $10^{4.1}\mathcal{L}_\odot$ to $10^{4.2}\mathcal{L}_\odot$ range in Figure 7.4 shows the ZAMS line moving further to the left for the $\alpha_{0.5}$ and $\alpha_{1.5}$ populations, while moving further to the right for the $\alpha_{5.0}$ population. We see the reverse at the TAMS, with the $\alpha_{5.0}$ population having the hottest TAMS point. The IACOB distribution, however, does not show a major shift between the $10^{4.0}\mathcal{L}_\odot$ to $10^{4.1}\mathcal{L}_\odot$ and $10^{4.1}\mathcal{L}_\odot$ to $10^{4.2}\mathcal{L}_\odot$ ranges, and the distribution shape and peak location stays the same.

The altered $\alpha_{0.5}$ and $\alpha_{1.5}$ distributions of simulated stars are better able to replicate

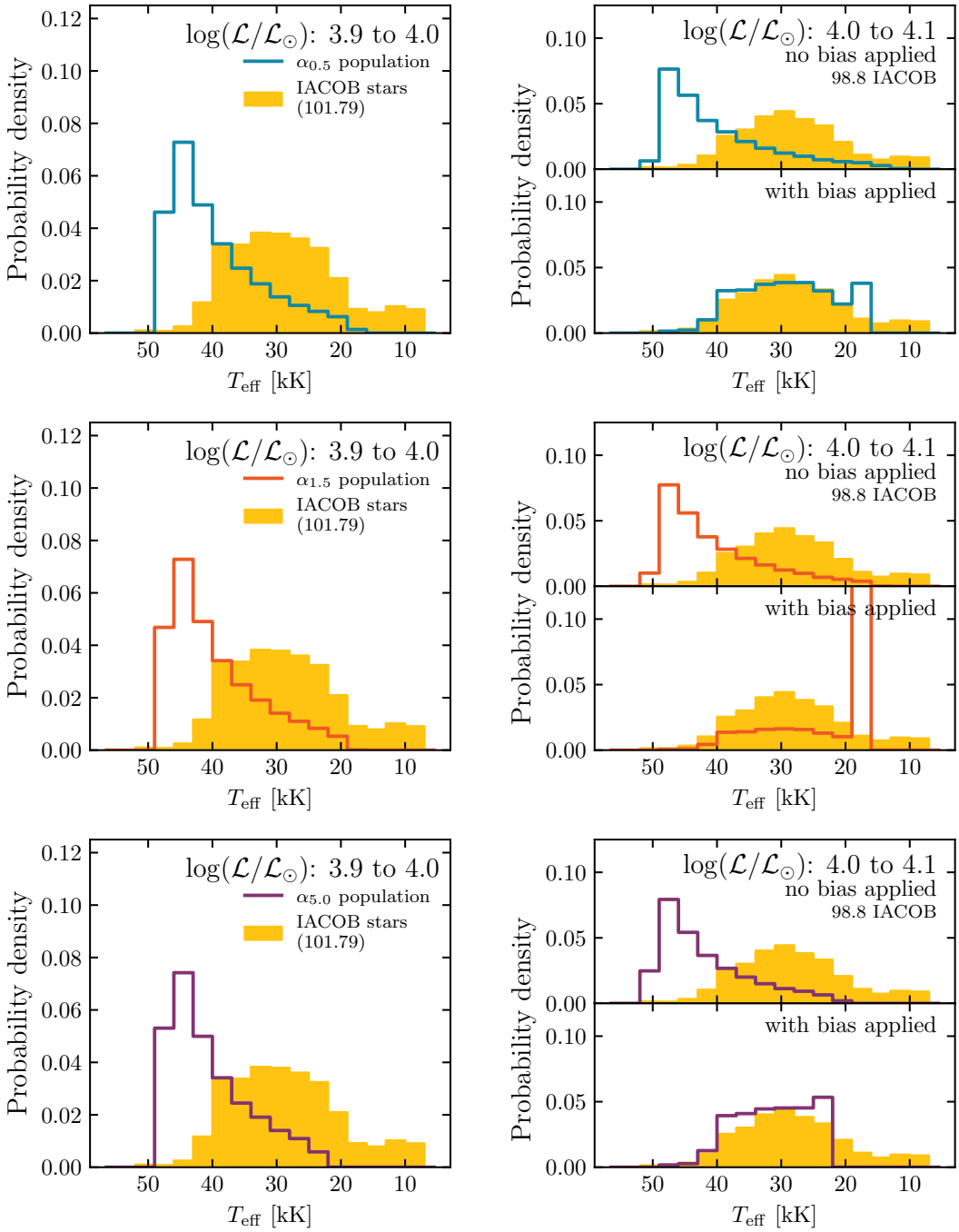

Figure 7.3: Distributions of the effective temperature at a fixed spectroscopic luminosity range for the IACOB stars and the three $\alpha_{\rm MLT}$ populations, in the same format as Figure 7.1. The distributions are for the spectroscopic luminosity range $10^{3.9}\mathcal{L}_\odot$ to $10^{4.1}\mathcal{L}_\odot$.

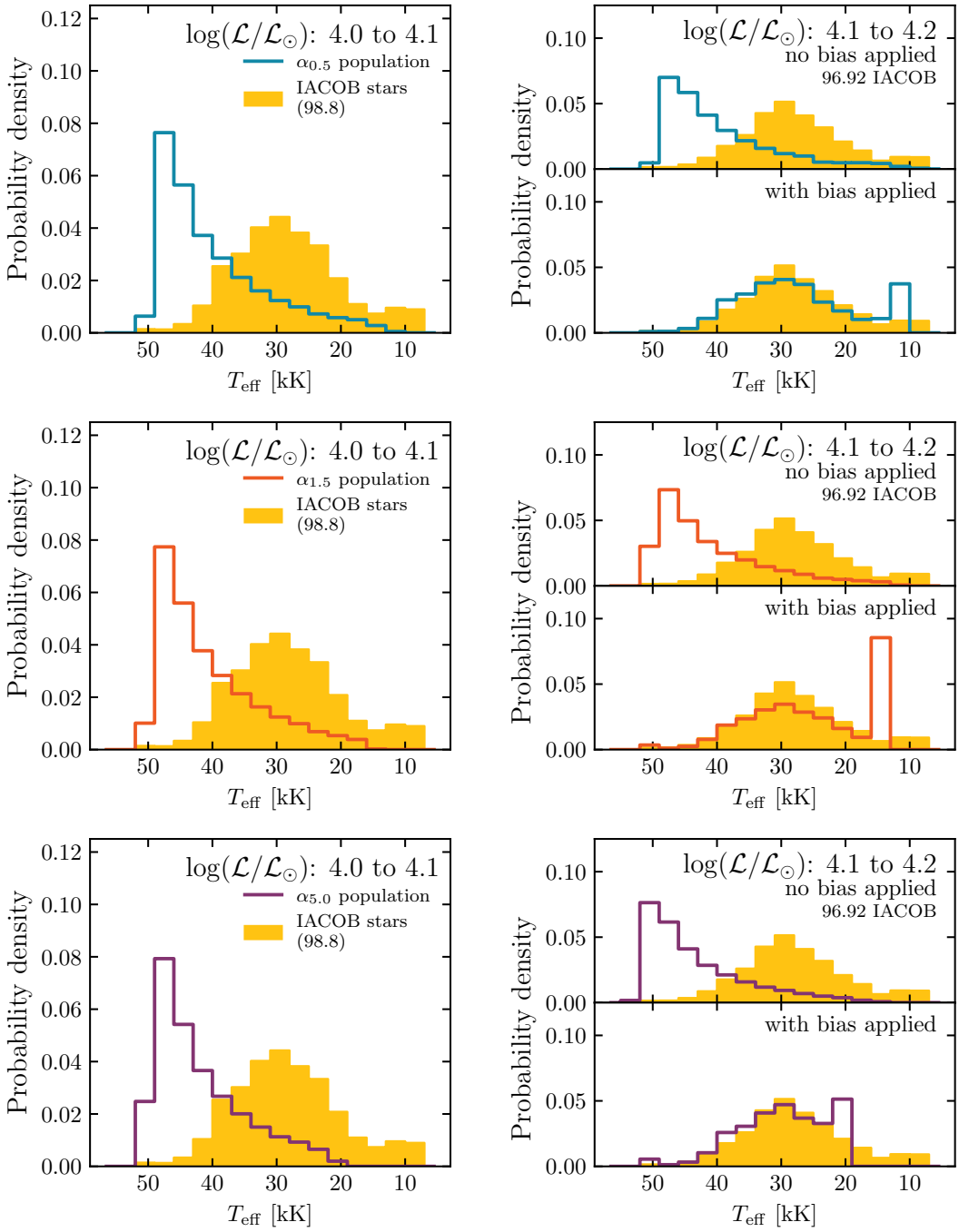

Figure 7.4: Distributions of the effective temperature at a fixed spectroscopic luminosity range for the IACOB stars and the three $\alpha_{\rm MLT}$ populations, in the same format as Figure 7.1. The distributions are for the spectroscopic luminosity range $10^{4.0}\mathcal{L}_\odot$ to $10^{4.2}\mathcal{L}_\odot$.

the shape of the IACOB distribution, with both shifting their peak to the center. The altered $\alpha_{0.5}$ distribution has too steep a slope on the left side of the peak and too shallow a slope on the right side, and the peak amplitude is still too low. The altered $\alpha_{1.5}$ distribution has too shallow a slope on both sides of the peak, consistently underestimating the number of stars per bin after ∼25 kK. The lower amplitudes can be partially explained by binning issues causing the abnormally tall bins at the cool end of the effective temperature range.

The altered $\alpha_{5.0}$ distribution is unable to reproduce the shape of the IACOB distribution. The location of the peak does shift to the center, but the slope on the left side of the peak is not smooth and too shallow and there is no slope on the right side. Instead, the distribution decreases in height for two bins before increasing in height for one bin and then terminating at ∼20 kK. The tall bin can be explained by binning issues, but the shape of the slope on the left and termination at ∼20 kK is due to the models' lack of inflation.

Spectroscopic luminosity range $10^{4.1}\mathcal{L}_\odot$ to $10^{4.3}\mathcal{L}_\odot$

The highest spectroscopic luminosity range considered, $10^{4.1}\mathcal{L}_\odot$ to $10^{4.3}\mathcal{L}_\odot$, is where the effect of the mixing length parameter value is the strongest. Therefore, this range is where we expect to see the largest differences between the simulated star populations. Figure 7.5 reflects this, as the increased width of the peaks in the unaltered $\alpha_{0.5}$ and $\alpha_{1.5}$ distributions for the $10^{4.2}\mathcal{L}_\odot$ to $10^{4.3}\mathcal{L}_\odot$ range is due to the bending of the ZAMS line increasing the range of effective temperatures at the ZAMS. The minimum temperature of the simulated star populations has also decreased, with some $\alpha_{0.5}$ simulated stars cooling down to ∼7 kK while still on the MS.

The IACOB distribution has shifted and the number of stars per bin for effective temperatures above ∼35 kK has markedly decreased, a consequence of the lack of high mass IACOB stars along the ZAMS line. The distribution to the right of the peak has also changed, with a stronger demarcation between the main peak and tail from ∼18 kK to ∼7 kK.

The decrease in minimum effective temperature for the simulated stars means that their distributions now reach into the area occupied by the tail of the IACOB distribution. We can see the effect of this most clearly for the altered $\alpha_{0.5}$ distribution, which now has a second, smaller peak at cool temperatures, resembling the IACOB distribution tail. This extension in minimum effective temperature, however, does not automatically mean a better fit. The altered $\alpha_{0.5}$ distribution is unable to match both the shape and peak location of the IACOB distribution. The bias factor did alter the distribution's shape, but could not create a centrally peaked pyramid like the IACOB distribution. In addition, the peak is located at ∼35 kK, while the IACOB peak is at ∼30 kK. The second peak, while matching the temperature range of the IACOB tail, is too tall and peaked, although this can be explained by binning issues.

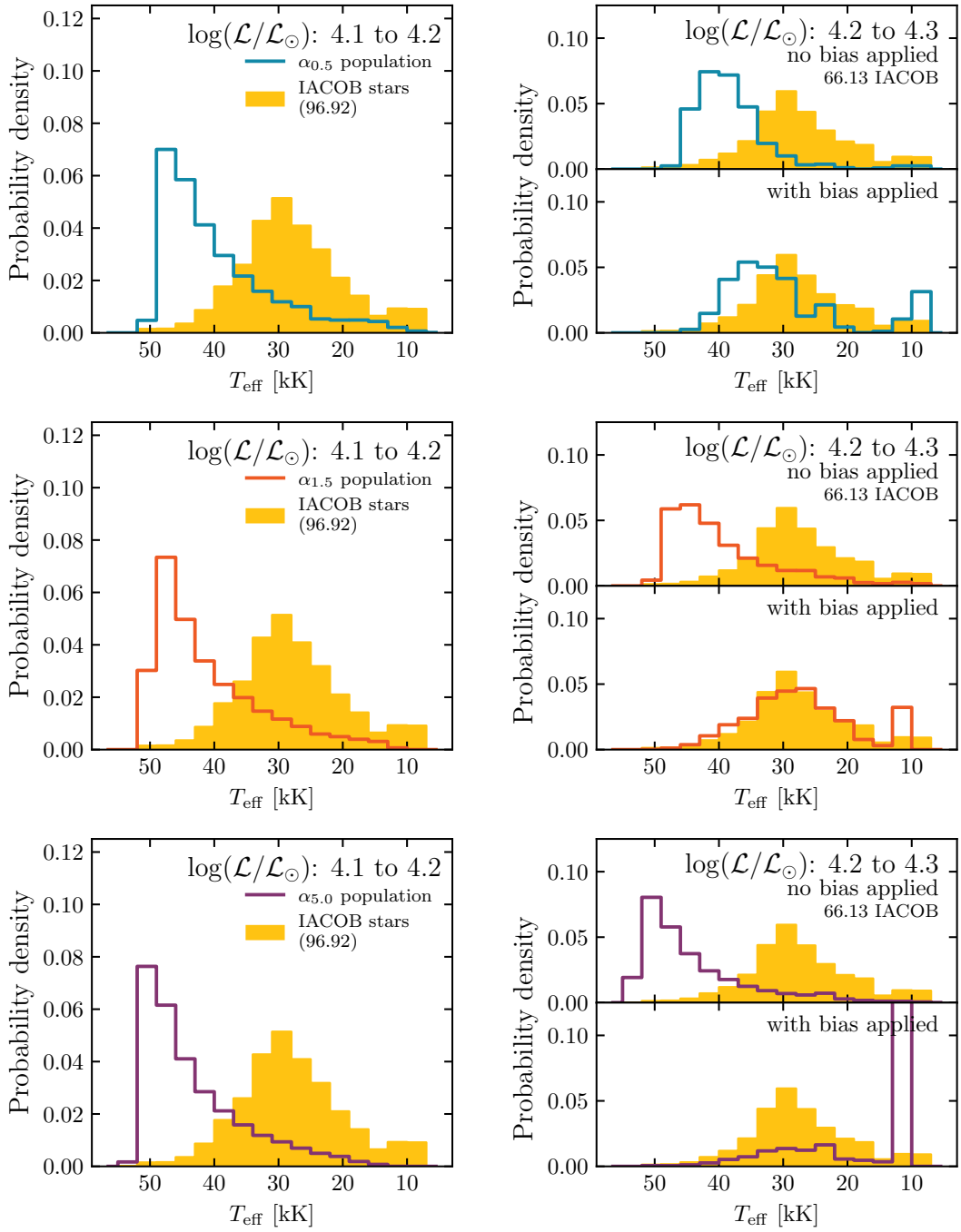

Figure 7.5: Distributions of the effective temperature at a fixed spectroscopic luminosity range for the IACOB stars and the three $\alpha_{\rm MLT}$ populations, in the same format as Figure 7.1. The distributions are for the spectroscopic luminosity range $10^{4.1}\mathcal{L}_\odot$ to $10^{4.3}\mathcal{L}_\odot$.

The altered $\alpha_{1.5}$ distribution is more accurate. While the peak amplitude is too low, it is only shifted one bin cooler than the IACOB peak. The slopes on either side of the peak are a good fit to the IACOB distribution, although on the left slope is slightly too shallow, while the slope on the right is slightly too steep. These simulated stars do not have quite as low a minimum temperature, so the tall bin at the ∼10 kK bin is likely only due to binning issues.

The altered $\alpha_{5.0}$ distribution is distorted by the extremely tall bin at ∼10 kK, which is due to the previously explained binning issues. Just looking at the shape of the distribution, however, we can still see that it is very flat and the peak location is at ∼25 kK, much cooler than the IACOB peak at ∼30 kK. Simulated stars at this spectroscopic luminosity range both start and end the MS at too high an effective temperature to be able to match the IACOB distribution.

We performed χ^2 analysis (Pearson, 1900) on our results and found that with the exception of the $10^{3.8}\mathcal{L}_\odot$ to $10^{3.9}\mathcal{L}_\odot$ range, seen in Figure 7.1, either the $\alpha_{0.5}$ or the $\alpha_{1.5}$ population was a better fit to the IACOB stars in our sample. The result for the $10^{3.8}\mathcal{L}_\odot$ to $10^{3.9}\mathcal{L}_\odot$ range is likely due to the binning issues that caused abnormally tall bins at the low effective temperature bins, creating fit issues that affected the χ^2 value. These fit issues also affected the other spectroscopic luminosity ranges, making it difficult to conclusively state that either the $\alpha_{0.5}$ or $\alpha_{1.5}$ population is a better fit. Instead, all we can say is that the IACOB stars are more consistent with these populations than with the $\alpha_{5.0}$ population and thus show evidence of inflation at high masses.

Chapter 8

Discussion

8.1 Spindown and envelope inflation

If massive stars can have inflated envelopes while on the MS, then inflated massive stars in binaries are likely to overflow their Roche lobes and undergo mass transfer (MT) while still core hydrogen burning, known as Case A mass transfer (Lamers et al., 2017). The companion star accretes both mass and angular momentum, which cause it to spin up. Sana et al. (2012) modeled a population of Galactic massive O-type single and binary stars and estimated that nearly 40 % will spin up while still on the MS due to accretion or merging with their companion. The percentage of spun up stars appears to have a metallicity dependence, as de Mink et al. (2013) modeled a population of massive stars at LMC metallicity and found that only ∼20 % of massive MS stars are expected to spin up due to binary interaction.

As discussed earlier, envelope inflation is metallicity dependent. If inflation occurs at lower masses for higher metallicities, then we would naturally also expect more spun up stars at higher metallicities, as a greater percentage of massive stars will experience Case A MT. As this thesis has shown, sufficiently massive stars can have inflated envelopes even at the ZAMS, so MT could occur as early as the ZAMS. The single star populations in this thesis were unable to replicate the rapidly rotating tail seen in the IACOB projected rotational velocity distribution, and were also unable to match the low spindown rate seen at high masses. Envelope inflation and binary interaction could provide a solution to both of these problems.

Binary interaction is not the only process by which envelope inflation can affect spindown. The most basic consequences of inflation are an increased radius and lowered effective temperature. Conservation of angular momentum demands that an increased radius be compensated for by a decrease in rotation rate. Cooler stars have stronger winds, due to the effect of the iron opacity bump (Sanyal et al., 2017), and these winds will increase the mass loss rate, which will then increase spindown. Additionally, instabilities in inflated envelopes can lead to mass loss, which will also affect spindown (Grassitelli et al., 2016).

Envelope inflation could also play a part in the lack of massive O-type stars near the ZAMS in the IACOB sample. Inflated stars have cooler effective temperatures, and the ZAMS lines of our models with mixing length parameters $\alpha_{\rm MLT} = 0.5$ and

1.5 bend strongly to the right. As an example, the $\alpha_{0.5}$ 200 $M_\odot$ model has a ZAMS effective temperature below 40 kK, while the $\alpha_{5.0}$ 200 $M_\odot$ model is over 50 kK. If we expect the high mass IACOB stars to be inflated at the ZAMS, then the gap between the ZAMS line and the hottest IACOB stars becomes smaller.

8.2 Comparison with previous work

8.2.1 The VLT-FLAMES Survey

The other major spectroscopic study of massive stars is the VLT-FLAMES Tarantula Survey (VFTS), which investigated the physical properties and multiplicity of over 800 OB stars in the Tarantula nebula in the Large Magellanic Cloud (LMC). The survey selected targets on the basis of magnitude, with no color cuts, and then by ability to position the spectrograph fibers, in an attempt to avoid significant selection bias (Evans et al., 2011). So far, Dufton et al. (2013, 2019) and Ramírez-Agudelo et al. (2013, 2017) have analyzed the rotational velocities of single stars in the VFTS sample. Thus far, VFTS studies have focused mainly on measuring projected rotational velocities, constraining the binary fraction, and investigating rotational mixing. The evolution of the rotation rate across the MS is less investigated. Therefore, we will focus on Ramírez-Agudelo et al. (2013) and Dufton et al. (2013) as comparisons for this thesis, as these two studies focused specifically on rotation rates, even if they do not look at spindown.

Ramírez-Agudelo et al. (2013) constructed the distribution of projected rotational velocity for the 216 likely single O-type stars in the Tarantula nebula. Similar to our IACOB sample, they found a clear peak at ∼80 km s^{-1} and a high velocity tail that extended out to ∼600 km s^{-1}. Figure 8.1 shows the distribution. As ∼80 % of their sample consisted of stars with masses below ∼40 $M_\odot$, they conclude that their low velocity peak cannot be explained by stellar wind induced spindown, as these stars' mass loss rates are too low for significant MS spindown. Instead, they suggest that the slow rotators could be explained by magnetic braking. They point out that the existence of a high velocity tail is predicted by de Mink et al. (2013), which studied the influence of binary evolution on the projected rotation rates of massive stars.

Dufton et al. (2013) put together the projected rotational velocity distribution for 237 single early B-type stars and late O-type stars in the Tarantula nebula. They found a strong bimodal distribution, as seen in Figure 8.2. The IACOB data also appears to be bimodal, but the faster peak in the IACOB distribution is much weaker. While approximately 25 % of the Dufton et al. (2013) sample has $v \sin i \leq 80$ km s^{-1}, the slow peak in the distribution is slower than 80 km s^{-1}. They were not able to conclusively determine the source of the bimodality, but agreed with Ramírez-Agudelo et al. (2013) that the low velocity peak could be due to magnetic braking and the high velocity tail could be due to binary interactions.

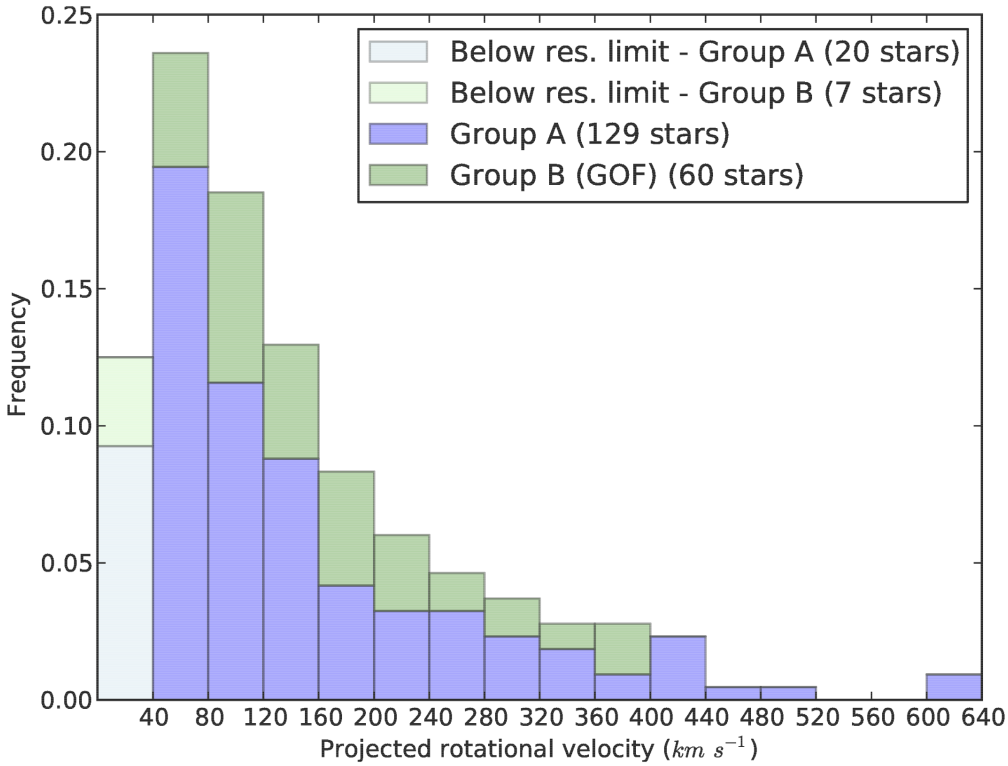

Figure 8.1: The distribution of projected rotational velocity for 216 likely single O2- to O9.7-type stars in the Tarantula nebula. Figure reproduced from Ramírez-Agudelo et al. (2013).

The distribution of projected rotational velocity for the IACOB stars has the $\sim$80 km s^{-1} peak seen in the Ramírez-Agudelo et al. (2013) study and the bimodal distribution seen in Dufton et al. (2013). There is currently no conclusive evidence for the source of either of these features, but it is likely that magnetic braking and binary interaction play a role. Thus far, our single star populations are unable to replicate the rapidly rotating tail seen in the IACOB projected rotational velocity distribution and adding a binary fraction, as in de Mink et al. (2013), is a promising avenue for solving this problem.

8.2.2 Previous inflation studies

Inflation has not been heavily investigated so far, and there are no observational studies focused on testing envelope inflation. Gräfener (2021) also compared the number distributions of effective temperature for inflated models against observations, although for VFTS stars. The results supported the existence of inflated envelopes on the MS for sufficiently massive stars, which can make luminous OB-type stars on

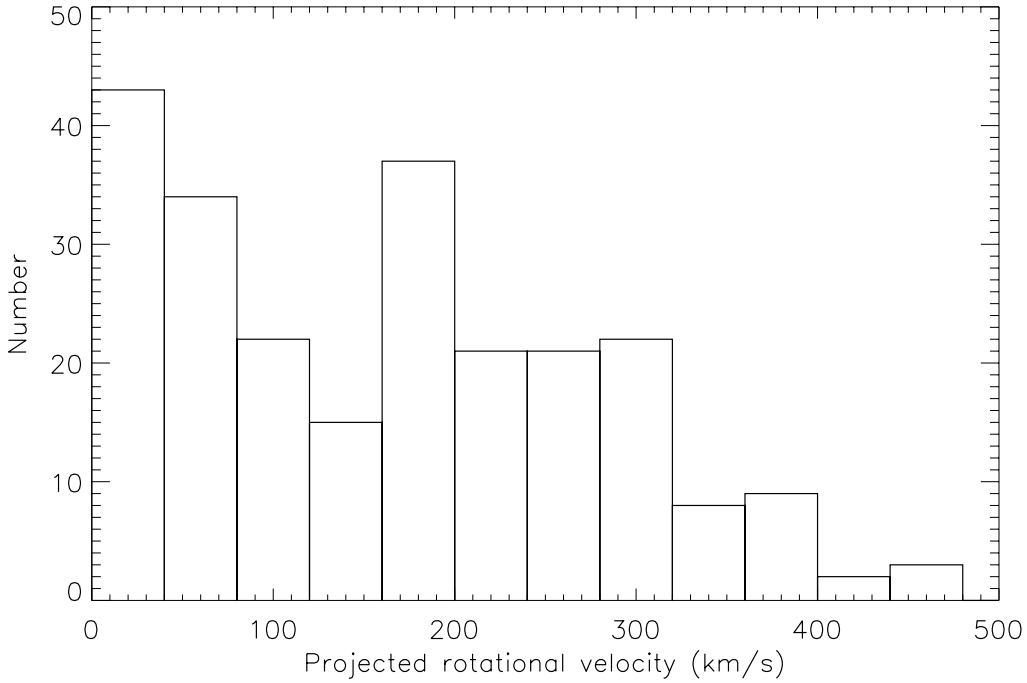

Figure 8.2: The distribution of projected rotational velocity for 274 likely single B3- to O9.5-type stars in the Tarantula nebula. Figure adapted from Dufton et al. (2013).

the MS appear as B-type supergiants.

Sanyal et al. (2015, 2017) determined that envelope inflation has a metallicity dependence, and it is easier for models to reach the Eddington limit at higher metallicities. Galactic metallicity models can inflate with initial masses as low as $30\,M_\odot$, while Population III models (metal-free and hot), require an initial mass of $150\,M_\odot$ for the same effect. Our Galactic metallicity models showed similar behavior, with inflation effects appearing between the $20\,M_\odot$ and $26\,M_\odot$ $\alpha_{0.5}$ models. They also found that higher metallicity models have less mass contained in the inflated envelope and theorized that models with envelope masses above $\sim 1\,M_\odot$ could be be progenitors of violently erupting LBVs.

Both Grassitelli et al. (2016) and Gräfener et al. (2012) studied envelopes of post-MS WRs and luminous blue variable stars (LBVs). Grassitelli et al. (2016) found pulsational instabilities in the inflated envelopes of models corresponding to hydrogen-free WRs between $\sim 9\,M_\odot$ to $\sim 14\,M_\odot$, which caused a corresponding increase in mass loss. Above $14\,M_\odot$, however, strong mass loss stabilized the models' inflated envelopes. Gräfener et al. (2012) found that envelope inflation could explain why LBVs in the LMC have been observed to vary their effective temperatures between $\sim 30\,kK$ to $\sim 8\,kK$ over a time period of years to decades, and why the observed radii of WRs are nearly an order of magnitude greater than models suggest.

The scope of this thesis does not include post-MS evolution or mass loss rates in inflated stars, but Gräfener et al. (2012), Grassitelli et al. (2016), and Sanyal et al. (2017) indicate that this is an interesting avenue for future study.

8.3 Uncertainties

8.3.1 Observed sample

The observation bias in the IACOB sample is by far the most consequential uncertainty in this study. The sample is missing a number of stars, the addition of which will naturally affect our distributions of projected rotational velocity and effective temperature. In addition, the fact that the sample is magnitude limited, with $B \leq 9\,\mathrm{mag}$, means that it is biased towards B-type supergiants, as they are brighter than O-type supergiants at low effective temperatures.

The IACOB project finds the subsample of O-type stars to be complete with respect to all known Galactic O-type stars in the Northern Hemisphere with $B \leq 9\,\mathrm{mag}$ (Simón-Díaz, 2022a), using the Galactic O-star Catalog (Maíz Apellániz et al., 2013) to evaluate completeness. Including Southern Hemisphere O-type stars, the O-type subsample is ∼90 % complete (Holgado, 2019). The subsample of B-type supergiants with $B \leq 9\,\mathrm{mag}$ is ∼95 % for Northern Hemisphere stars and ∼70 % complete for Southern Hemisphere stars (Simón-Díaz, 2022a).

Observations have been failing to find massive O-type stars near the ZAMS for decades now, and the IACOB project is no exception. Holgado et al. (2020) estimates that these missing stars are ∼O4 to ∼O6.5 type, but have so far been unable to find them within the current magnitude limit. They propose several reasons for this. It is possible that the method they use to calculate the surface gravity may be producing estimates below the actual value, thereby artificially increasing the spectroscopic luminosity. However, the lack of massive Galactic O-type stars near the ZAMS has been reported in the literature since Garmany et al. (1982), making this possibility unlikely. The stars could be dimmer than previously thought, due to extinction from the dense and optically thick material that can surround baby stars while they evolve off the ZAMS. This explanation would require evidence of a correlation between high extinction and newborn stars.

Adding these missing stars to the IACOB database, if they do exist, will have far-reaching consequences. These massive O-type stars would be located in the first quarter of the MS for our $50\,\mathrm{M}_\odot$ to $100\,\mathrm{M}_\odot$ bin, which would allow us to study how the distribution of projected rotational velocity changes across the whole MS, rather than just the second half. The IACOB distributions of effective temperature would also change, as Figure 4.1 shows that the missing stars would have $T_{\mathrm{eff}} \gtrsim 40\,\mathrm{kK}$. Including these stars would increase the mean effective temperature, shifting the

distributions to higher temperatures.

If there truly are no massive O-type stars near the theoretical ZAMS line, then perhaps the theoretical ZAMS line needs to be adjusted. Newly born stars accrete material from their parental cloud until the cloud is exhausted or dissolves, at which point they become visible in the optical spectrum. If the accretion rate is slow enough, these stars can ignite their hydrogen cores while still surrounded by an optically thick cloud. This would move the ZAMS line to cooler temperatures. Holgado et al. (2020) suggests that this is the most likely explanation and a promising avenue for future study, although a lack of data prevents them from reaching firm conclusions.

The B0- to B9-type supergiants are included in the fourth quarter of the MS for our $50\,M_\odot$ to $100\,M_\odot$ bin and have effective temperatures under $\sim$30 kK. B-type supergiants are thought to rotate slowly (Hunter et al., 2008), so the addition of missing stars will shift the relevant distributions of projected rotational velocity to slower rotation rates. In addition, the $v \sin i$ measurements for the existing B-type supergiants in the sample need to be further iterated (Simón-Díaz, 2022a), which could also change the distribution. As seen in Figure 6.8, the current IACOB distribution of projected rotational velocity in the fourth quarter of the MS has a much lower proportion of slow rotators than seen in the simulated star distribution. The discrepancy between the two distributions could be resolved with the addition of the missing B-type supergiants. In terms of our inflation study, $\sim$30 kK is in the center of our effective temperature range and more than half of the stars in the IACOB sample have an effective temperature below 30 kK. More B-type supergiants will shift the distributions to cooler effective temperatures.

The B0- to B1.5-type dwarfs are only from the Northern Hemisphere, and the subsample is biased towards slow rotators, $v \sin i \lesssim 80\,\mathrm{km\,s^{-1}}$, and stars with $B < 6$ mag. In terms of spindown, these stars comprise the majority of our $9\,M_\odot$ to $30\,M_\odot$ bin. Increasing the number of rapid rotators will shift the distribution towards higher velocities, which would explain why the simulated stars predict a lower proportion of slow rotators than observed. It is also possible that the bias in this subsample could be responsible for the bimodality we assumed in the distribution of projected rotational velocity. If this is true, then further observations could smooth out the second peak at $\sim$180 km s^{-1}. These stars have a maximum spectroscopic luminosity of $\sim 10^{3.7} \mathcal{L}_\odot$, so they are not included in our effective temperature distributions.

The observables used in this thesis also have their own uncertainties, separate from the observational bias. The uncertainties are assumed to be within a 1σ confidence interval. The effective temperature measurement has an uncertainty of $\pm 5\,\%$ and the spectroscopic luminosity measurement has an uncertainty of ± 0.15 dex. Projected rotational velocity measurements of $200\,\mathrm{km\,s^{-1}}$ and below have an uncertainty of $\pm 10\,\mathrm{km\,s^{-1}}$ and measurements above have an uncertainty of $\pm 5\,\%$ (Simón-Díaz, 2022b). Due to the effects of microturbulence, projected rotational

velocity measurements below $\sim$40 km s^{-1} are only an upper limit (Simón-Díaz and Herrero, 2014).

8.3.2 Uncertainties in modeling

The most obvious uncertainty in our evolutionary models is the application of angular momentum corrections to the Brott grid. As mentioned before, modifying the stellar code and recalculating the Brott grid would be the most correct approach, as angular momentum loss is a complex process that can interact with many different parameters. As an example, the surface abundances of our models are not altered by the corrections, even though we know that rotational mixing and angular momentum transport both play a part in bringing material to the stellar surface. However, the corrections to the angular momentum loss rate are relatively small, on the order of $\sim$10 % to $\sim$30 %, and they do not affect the models' evolutionary pathway. Therefore, a full recalculation of the grid was not required for the purposes of this thesis.

Another important uncertainty is the mass loss treatment, as mass loss rates have a strong influence on spindown. Our models use the stellar wind mass loss prescriptions of Hamann et al. (1995), Nieuwenhuijzen and de Jager (1990), and Vink et al. (2000, 2001), using linear interpolation for smooth transitions. These prescriptions use the optically thin micro-clumping approach, which assumes that the wind mass is contained in small clumps on the stellar surface and the wind between the clumps has no mass. This obviously an unphysical approximation, and Hawcroft et al. (2021) showed that the micro-clumping approach used in Vink et al. (2000) overestimates the mass loss rate by a factor of $\sim$3.6 for a sample of 8 early-type O supergiants. The mass loss rates for stars near the Eddington limit, however, may be underestimated. Vink (2021) found a sharp increase in the slope of the mass loss rate vs. Eddington limit relation, jumping from $\dot{M} \propto \Gamma^2$ for stars with $\Gamma \lesssim 0.7$ to $\dot{M} \propto \Gamma^5$ for higher Γ. Our models do not take the findings of Hawcroft et al. (2021) or Vink et al. (2011) into account, so non-inflated models may be spinning down too much, while inflated models may not be spinning down enough.

The overshooting parameter for the models was calibrated against stars in the LMC, using data from VLT-FLAMES survey (Evans et al., 2005). This is a lower metallicity environment than the Milky Way, so the calibration might have resulted in a too-low overshooting parameter, due to a possible metallicity dependence (Cordier et al., 2002). A greater overshooting parameter means more material is mixed into the stellar core, causing a longer MS lifetime and cooler TAMS point. However, Brott et al. (2011) tested their assumption that the overshooting parameter does not depend on metallicity by comparing their models to the VLT-FLAMES Galactic sample and found that any change was within the measurement uncertainty.

The initial distribution functions in Hōkū are another source of uncertainty. Our flat IMF overestimates the number of high mass simulated stars, which means that we

cannot compare number distributions across broad luminosity ranges. Our simulated star populations cover a broad mass range from $3\,M_\odot$ to $200\,M_\odot$ and using a Salpeter IMF (Salpeter, 1955) would have required a population of millions, which is not computationally feasible. We chose a flat IMF in order to generate enough high mass stars for meaningful statistics. While this means that our populations are biased towards massive stars, the existing bias in the IACOB sample means that the impact is minimal.

We chose a ZAMS velocity of $200\,\mathrm{km\,s^{-1}}$ for the simulated stars in the Brott single v_{ZAMS} population. As the IACOB stars are not from a single cluster, instead located all over the Northern and Southern Hemispheres, a single v_{ZAMS} velocity was only ever intended as a simple approximation. The Brott distribution v_{ZAMS} population used the initial velocity PDF discussed in Section 3.2.1, which we fit to the distribution of current IACOB projected rotational velocities. We assumed a bimodal distribution in the fitting process, and we have already discussed the possibility that this feature is due to observational bias rather than a true increase in the number of stars with $v \sin i \sim 180\,\mathrm{km\,s^{-1}}$. Lastly, fitting our PDF to the IACOB distribution of current velocities means that it is not surprising that the resulting simulated star velocity distributions resemble the said IACOB distribution. However, as we do not have estimates of intrinsic or initial velocity for the IACOB stars, any choice of initial velocity PDF will be inherently speculative.

The incomplete portions of the IACOB sample are very obvious in our inflation analysis, and we can clearly see where the sample is missing stars. We attempted to correct for the observational bias by calculating a bias factor that we then applied to the simulated star distributions of effective temperature. We describe the bias factor calculation in Section 3.3. It goes without saying that results using this technique are preliminary and require further iteration with a larger observational sample.

Chapter 9

Conclusions

9.1 This thesis

We use grids of single star evolutionary models, population synthesis, and observations to study spindown and envelope inflation in Galactic massive main sequence stars. We use the Brott et al. (2011) grids to study spindown and calculate our own models using MESA to study inflation. We also develop the stellar population synthesis code Hōkū to interpolate large populations of single stars, which we then use to compare distributions of rotation rate and effective temperature with a sample of stars from the IACOB project.

The implementation of angular momentum loss in the Brott grid is unphysical, so we first discuss the proper treatment and apply it to the Brott grid, recalculating the rate of angular momentum loss, total angular momentum, surface specific angular momentum, and rotation rate in the process. As expected, the corrections have a negligible effect on low mass models, because their rates of angular momentum loss are already small. However, the corrections make an increasingly large difference for models above $30\,M_\odot$. We find that corrected models above $30\,M_\odot$ spin down more completely and at a more consistent rate. We also find that while that uncorrected models gain surface specific angular momentum throughout the main sequence, even for the $100\,M_\odot$ model, the corrected models do not show surface specific angular momentum gain past an initial mass of $40\,M_\odot$.

We find that our simulated star populations are unable to replicate the projected rotational velocity distribution of the IACOB sample, which is characterized by a bimodal shape and tail of rapidly rotating stars that extends out to $\sim$450 km s^{-1}. While the location of the simulated stars' velocity distribution peak moves to lower velocities as initial mass increases, the IACOB stars have fewer slow rotators at high masses. In addition, the high mass IACOB stars do not show a strong braking mechanism in the second half of the MS, which contradicts the strong spindown seen in the simulated stars. This is perhaps due to MS binary interaction.

The IACOB stars in our sample show projected rotation rates above 300 km s^{-1}, even in the fourth quarter of the MS. This implies that the neutron star or black hole formed post-supernova will be rapidly rotating, due to the large amount of angular momentum left in the core during core-collapse.

In order to understand the effect of inflation on stellar evolution, we calculate new evolutionary models, varying the efficiency of convective energy transport. We find, in agreement with previous work, that inflation lowers a star's effective temperature, moving the ZAMS and TAMS lines redward. The point at which inflation takes effect has a dependence on mass, as a $26\,M_\odot$ model is inflated at the TAMS, while a $72\,M_\odot$ model can already be inflated at the ZAMS, given sufficiently inefficient convective energy transport.

We use distributions of effective temperature at fixed spectroscopic luminosity ranges to investigate inflation in the IACOB sample and calculate a crude bias factor in an attempt to compensate for observational bias. We find that the IACOB stars show evidence of inflation at high masses, although these results are preliminary.

9.2 Outlook

Continuing the work begun in this thesis requires a better understanding of the IACOB biases, as well as a more complete sample with more observables. The IACOB project is currently working on further iterating the observables used in this thesis, as well as estimating bolometric luminosity and surface abundances. They are further expanding the database with a new survey starting in fall of 2022, which will use the WHT Enhanced Area Velocity Explorer (WEAVE) instrument, a new multi-object survey spectrograph for the William Herschel Telescope at the Observatorio del Roque de los Muchachos, on La Palma in the Canary Islands (Dalton, 2016). Using WEAVE will allow the IACOB project to observe much dimmer stars, going from their current magnitude limit of $B \leq 9\,\text{mag}$ up to $B \leq 16\,\text{mag}$, increasing the size of the database from ∼1000 OB stars to over 5000.

As previously discussed, inflation has wide-ranging consequences for stellar evolution. A star's position in the HR diagram and its rotational velocity can both be affected by envelope inflation. For example, two stars with the same effective temperature, one inflated and one not, could have very different spindown histories. This is an interesting avenue for future study. In addition, it is possible that the stellar wind mass loss recipes used in our evolutionary models may be underestimating the impact of clumping. Implementing mass loss recipes that update the treatment of clumping would increase the reliability of our spindown analysis.

Hōkū provides a solid foundation for future analysis of stars from the IACOB project and the work done in this thesis is only the beginning of what will be possible. Further investigation of spindown, studying the impact of inflation, examining the effect of updated mass loss recipes, adding a binary fraction to our population synthesis, and using surface abundances as a probe of rotational mixing are just some of the areas of potential study we can explore using the power of Hōkū combined with the IACOB project database.

Appendix A

Isochrones

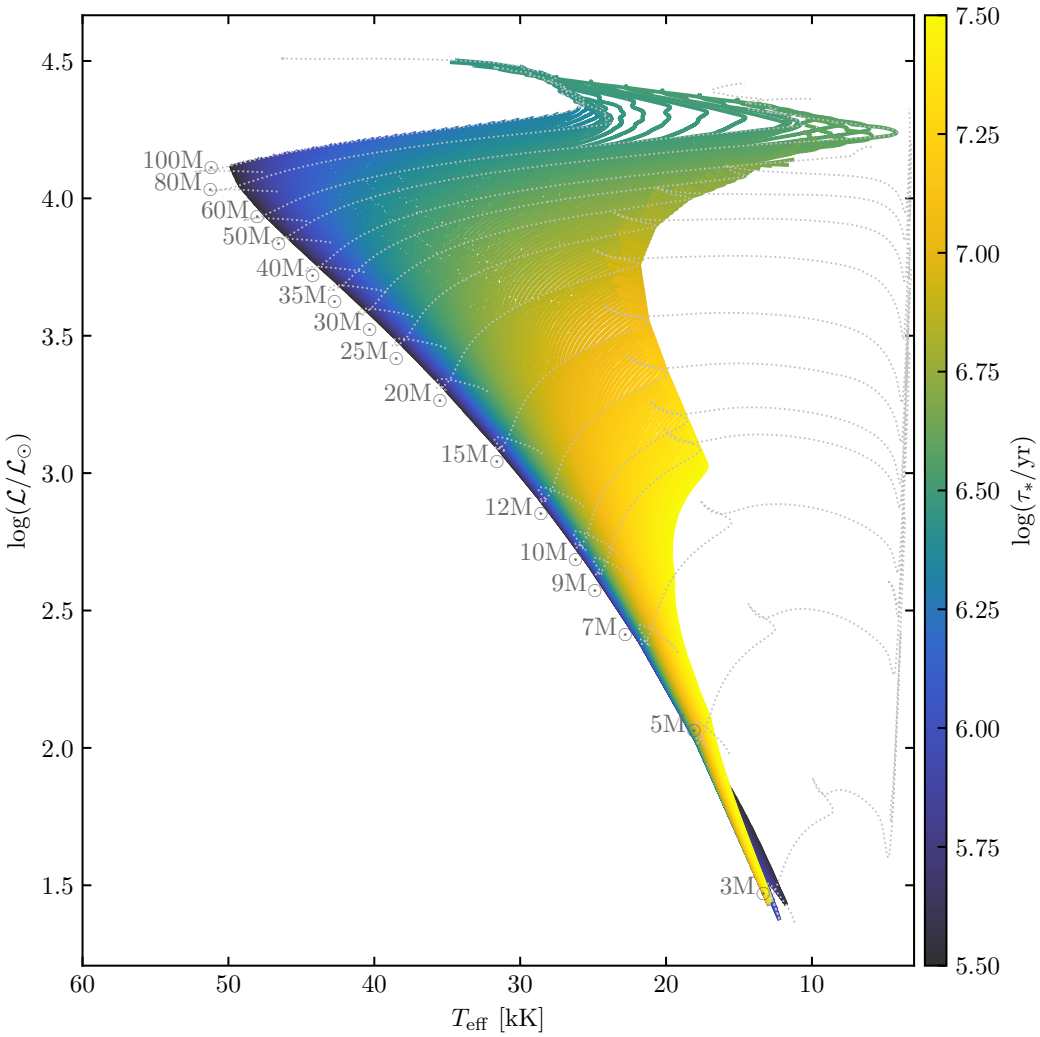

Figure A.1: Isochrones at $\log(\tau_*/\mathrm{yr}) = 5.5$ to 7.5 (0.32 Myr to 32 Myr), spaced 0.01 in logspace. Hōkū interpolated the isochrones in mass from $3\,\mathrm{M}_\odot$ to $100\,\mathrm{M}_\odot$ using the non-rotating Brott grid evolutionary tracks, which are plotted as gray dotted lines.

Bibliography

Abbott, B. P. et al. (Oct. 2017). "Multi-Messenger Observations of a Binary Neutron Star Merger". In: *The Astrophysical Journal* 848, p. L12. DOI: 10.3847/2041-8213/aa91c9.

Abbott, B. P. et al. (Jan. 2019). "Properties of the Binary Neutron Star Merger GW170817". In: *Physical Review X* 9, p. 011001. DOI: 10.1103/PhysRevX.9.011001.

Abbott, B. P. et al. (n.d.). "GW151226: Observation of Gravitational Waves from a 22-Solar-Mass Binary Black Hole Coalescence". In: ().

Abbott, R. et al. (July 2021). "Observation of Gravitational Waves from Two Neutron Star-Black Hole Coalescences". In: *The Astrophysical Journal* 915, p. L5. DOI: 10.3847/2041-8213/ac082e.

Barbá, Rodolfo H. et al. (Nov. 2017). "OWN Survey: A Spectroscopic Monitoring of Southern Galactic O and WN-Type Stars". In: 329, pp. 89–96. DOI: 10.1017/S1743921317003258.

Baym, Gordon et al. (May 2018). "From Hadrons to Quarks in Neutron Stars: A Review". In: *Reports on Progress in Physics* 81, p. 056902. DOI: 10.1088/1361-6633/aaae14.

Benjamin, Robert A. et al. (Aug. 2003). "GLIMPSE. I. An SIRTF Legacy Project to Map the Inner Galaxy". In: *Publications of the Astronomical Society of the Pacific* 115, pp. 953–964. DOI: 10.1086/376696.

Bromm, Volker et al. (May 2009). "The Formation of the First Stars and Galaxies". In: *Nature* 459, pp. 49–54. DOI: 10.1038/nature07990.

Brott, I. et al. (June 2011). "Rotating Massive Main-Sequence Stars: I. Grids of Evolutionary Models and Isochrones". In: *Astronomy & Astrophysics* 530, A115. DOI: 10/dc79xx.

Burbidge, E. Margaret et al. (Jan. 1957). "Synthesis of the Elements in Stars". In: *Reviews of Modern Physics* 29, pp. 547–650. DOI: 10.1103/RevModPhys.29.547.

Burrows, A. and D. Vartanyan (Jan. 2021). "Core-Collapse Supernova Explosion Theory". In: *Nature* 589, pp. 29–39. DOI: 10.1038/s41586-020-03059-w.

Burrows, Adam et al. (Sept. 1995). "On the Nature of Core-Collapse Supernova Explosions". In: *The Astrophysical Journal* 450, p. 830. DOI: 10.1086/176188.

Carroll, J. A. (May 1933). "The Spectroscopic Determination of Stellar Rotation and Its Effect on Line Profiles". In: *Monthly Notices of the Royal Astronomical Society* 93, pp. 478–507. DOI: 10/gn8pq5.

Celotti, A. et al. (Nov. 1999). "Astrophysical Evidence for the Existence of Black Holes". In: *Classical and Quantum Gravity* 16 (12A), A3–A21. DOI: 10.1088/0264-9381/16/12A/301.

Chiappini, Cristina et al. (Apr. 2011). "Imprints of Fast-Rotating Massive Stars in the Galactic Bulge". In: *Nature* 472, pp. 454–457. DOI: 10.1038/nature10000.

Cordier, D. et al. (Sept. 2002). "Convective Core Mixing: A Metallicity Dependence?" In: *Astronomy and Astrophysics, v.392, p.169-180 (2002)* 392, p. 169. DOI: 10.1051/0004-6361:20020934.

Cox, J. P. and R. T. Giuli (1968). *Principles of Stellar Structure*. 1st Ed. New York, NY: Gordon and Breach. ISBN: 978-0-677-01950-5.

Crowther, Paul A. (Nov. 2019). "Massive Stars in the Tarantula Nebula: A Rosetta Stone for Extragalactic Supergiant HII Regions". In: *Galaxies* 7, p. 88. DOI: 10.3390/galaxies7040088.

Dalton, G. (Oct. 2016). "WEAVE: The Next Generation Spectroscopy Facility for the WHT". In: 507, p. 97. URL: https://ui.adsabs.harvard.edu/abs/2016ASPC..507...97D (visited on 05/11/2022).

De Mink, S. E. et al. (Feb. 2013). "The Rotation Rates of Massive Stars: The Role of Binary Interaction through Tides, Mass Transfer, and Mergers". In: *The Astrophysical Journal* 764, p. 166. DOI: 10.1088/0004-637X/764/2/166.

De Rossi, M. E. et al. (Sept. 2010). "Impact of Supernova Feedback on the Tully-Fisher Relation". In: *Astronomy and Astrophysics* 519, A89. DOI: 10.1051/0004-6361/201014058.

Dufton, P. L. et al. (Feb. 2013). "The VLT-FLAMES Tarantula Survey. X. Evidence for a Bimodal Distribution of Rotational Velocities for the Single Early B-Type Stars". In: *Astronomy and Astrophysics* 550, A109. DOI: 10.1051/0004-6361/201220273.

Dufton, P. L. et al. (June 2019). "A Census of Massive Stars in NGC 346. Stellar Parameters and Rotational Velocities". In: *Astronomy and Astrophysics* 626, A50. DOI: 10.1051/0004-6361/201935415.

Eddington, A. S. (Sept. 1920). "The Internal Constitution of the Stars". In: *Science* 52.1341, pp. 233–240. DOI: 10.1126/science.52.1341.233.

Endal, A. S. and S. Sofia (Nov. 1976). "The Evolution of Rotating Stars. I - Method and Exploratory Calculations for a 7-Solar-Mass Star". In: *The Astrophysical Journal* 210, p. 184. DOI: 10/cph8p6.

Evans, C. J. et al. (July 2005). "The VLT-FLAMES Survey of Massive Stars: Observations in the Galactic Clusters NGC 3293, NGC 4755 and NGC 6611". In: *Astronomy and Astrophysics* 437.2, pp. 467–482. DOI: 10/cvjwjc.

Evans, C. J. et al. (June 2011). "The VLT-FLAMES Tarantula Survey. I. Introduction and Observational Overview". In: *Astronomy and Astrophysics* 530, A108. DOI: 10.1051/0004-6361/201116782.

Garmany, C. D. et al. (Dec. 1982). "The Initial Mass Function for Massive Stars." In: *The Astrophysical Journal* 263, pp. 777–790. DOI: 10.1086/160548.

Gräfener, G. et al. (Feb. 2012). "Stellar Envelope Inflation near the Eddington Limit - Implications for the Radii of Wolf-Rayet Stars and Luminous Blue Variables". In: *Astronomy & Astrophysics* 538, A40. DOI: 10.1051/0004-6361/201117497.

Gräfener, Götz (Mar. 2021). "Physics and Evolution of the Most Massive Stars in 30 Doradus. Mass Loss, Envelope Inflation, and a Variable Upper Stellar Mass Limit". In: *Astronomy and Astrophysics* 647, A13. DOI: 10.1051/0004-6361/202040037.

Grassitelli, L. et al. (May 2016). "Diagnostics of the Unstable Envelopes of Wolf-Rayet Stars". In: *Astronomy and Astrophysics* 590, A12. DOI: 10.1051/0004-6361/201527873.

Gray, David F. (Jan. 1976). *The Observation and Analysis of Stellar Photospheres*. 1st Ed. New York, NY: Wiley. ISBN: 978-0-471-32380-8.

– (Sept. 2005). *The Observation and Analysis of Stellar Photospheres*. 3rd Ed. UK: Cambridge University Press. ISBN: 0-521-85186-6.

Gritschneder, Matthias et al. (Aug. 2006). "Triggered Star Formation in the Environment of Young Massive Stars". In: *Proceedings of the International Astronomical Union* 2.S237, pp. 246–250. DOI: 10.1017/S174392130700155X.

Hamann, W.-R. et al. (July 1995). "Spectral Analyses of the Galactic Wolf-Rayet Stars: Hydrogen-Helium Abundances and Improved Stellar Parameters for the WN Class". In: *Astronomy and Astrophysics* 299, p. 151. ISSN: 0004-6361.

Hastings, Ben (Aug. 2021). *Angular Momentum Loss in Brott Models*. E-mail.

Hawcroft, C. et al. (Nov. 2021). "Empirical Mass-Loss Rates and Clumping Properties of Galactic Early-Type O Supergiants". In: *Astronomy & Astrophysics* 655, A67. DOI: 10.1051/0004-6361/202140603.

Heger, A. et al. (Jan. 2000). "Presupernova Evolution of Rotating Massive Stars. I. Numerical Method and Evolution of the Internal Stellar Structure". In: *The Astrophysical Journal* 528, pp. 368–396. DOI: 10/cz859h.

Heger, A. et al. (July 2003). "How Massive Single Stars End Their Life". In: *The Astrophysical Journal* 591.1, p. 288. DOI: 10.1086/375341.

Hertzsprung, Ejnar (Jan. 1911). "Ueber Die Verwendung Photographischer Effektiver Wellenlaengen Zur Bestimmung von Farbenaequivalenten". In: *Publikationen des Astrophysikalischen Observatoriums zu Potsdam* 63. URL: https://ui.adsabs.harvard.edu/abs/1911POPot..63.....H (visited on 04/20/2022).

Holgado, G. (Dec. 2019). "Spectroscopic and Physical Characterization of the Galactic O-Type Stars Targeted by the IACOB & OWN Surveys". PhD thesis. Santa Cruz de Tenerife, Spain: Universidad de La Laguna. 311 pp. URL: https://cloud.iac.es/index.php/s/KtLgT0z8mMBkqVn (visited on 02/13/2022).

Holgado, G. et al. (June 2020). "The IACOB Project - VI. On the Elusive Detection of Massive O-Type Stars Close to the ZAMS". In: *Astronomy & Astrophysics* 638, A157. DOI: 10/gphnmz.

Hunter, I. et al. (Feb. 2008). "The VLT-FLAMES Survey of Massive Stars: Atmospheric Parameters and Rotational Velocity Distributions for B-Type Stars in the Magellanic Clouds". In: *Astronomy and Astrophysics* 479, pp. 541–555. DOI: 10.1051/0004-6361:20078511.

Iglesias, Carlos A. and Forrest J. Rogers (June 1996). "Updated Opal Opacities". In: *The Astrophysical Journal* 464, p. 943. DOI: 10/b39f2d.

Kajino, T. et al. (July 2019). "Current Status of R-Process Nucleosynthesis". In: *Progress in Particle and Nuclear Physics* 107, pp. 109–166. DOI: 10.1016/j.ppnp.2019.02.008.

Kasen, Daniel et al. (Nov. 2017). "Origin of the Heavy Elements in Binary Neutron-Star Mergers from a Gravitational-Wave Event". In: *Nature* 551, pp. 80–84. DOI: 10.1038/nature24453.

Kato, M. (Feb. 1986). "Steady Mass-Loss from Supermassive Stars". In: *Astrophysics and Space Science, Volume 119, Issue 1, pp.57-59* 119.1, p. 57. DOI: 10.1007/BF00648812.

Kippenhahn, Rudolph and H. -C. Thomas (Jan. 1970). "A Simple Method for the Solution of the Stellar Structure Equations Including Rotation and Tidal Forces". In: *Proceedings of the IAU Colloquium Held at the Ohio State University, Columbus, OH., U.S.A., September 8–11, 1969*. IAU Colloq. 4: Stellar Rotation. Ohio State University, Columbus, OH: Springer, Dordrecht, pp. 20–29. ISBN: 978-94-010-3299-5.

Kippenhahn, Rudolph and Alfred Weigert (1990). *Stellar Structure and Evolution*. 1st Ed. Springer-Verlag. 192 pp. ISBN: 3-540-50211-4.

Koter, Alex de et al. (Mar. 1997). "On the Evolutionary Phase and Mass Loss of the Wolf-Rayet–like Stars in R136a". In: *The Astrophysical Journal* 477.2, pp. 792–816. DOI: 10/db869v.

Lamers, Henny J. G. L. M et al. (2017). *Understanding Stellar Evolution*. ISBN: 978-0-7503-1278-3.

Langer, N. (Jan. 1998). "Coupled Mass and Angular Momentum Loss of Massive Main Sequence Stars". In: *Astronomy and Astrophysics, v.329, p.551-558 (1998)* 329, p. 551. ISSN: 0004-6361.

– (Sept. 2012). "Presupernova Evolution of Massive Single and Binary Stars". In: *Annual Review of Astronomy and Astrophysics* 50, pp. 107–164. DOI: 10.1146/annurev-astro-081811-125534.

Langer, N. and R. P. Kudritzki (Apr. 2014). "The Spectroscopic Hertzsprung-Russell Diagram". In: *Astronomy & Astrophysics* 564, A52. DOI: 10/ggsj7s.

Langer, N. et al. (Sept. 1983). "Semiconvective Diffusion and Energy Transport". In: *Astronomy and Astrophysics* 126.1, p. 207. ISSN: 0004-6361.

Mac Low, Mordecai-Mark and Ralf S. Klessen (Jan. 2004). "Control of Star Formation by Supersonic Turbulence". In: *Reviews of Modern Physics* 76, pp. 125–194. DOI: 10.1103/RevModPhys.76.125.

Maeder, A. and G. Meynet (Sept. 2005). "Stellar Evolution with Rotation and Magnetic Fields. III. The Interplay of Circulation and Dynamo". In: *Astronomy and Astrophysics* 440.3, pp. 1041–1049. DOI: 10.1051/0004-6361:20053261.

Maíz Apellániz, J. et al. (June 2013). "First Whole-Sky Results from the Galactic O-Star Spectroscopic Survey". In: Massive Stars: From α to Ω. Rhodes, Greece, p. 198. URL: https://ui.adsabs.harvard.edu/abs/2013msao.confE.198M/abstract (visited on 04/22/2022).

Marchant, Pablo (2016a). *MESA Input Data: 2016 Binary Models*. URL: https://github.com/orlox/mesa_input_data/tree/master/2016_binary_models.

– (2016b). "The Impact of Tides and Mass Transfer on the Evolution of Metal-Poor Massive Binary Stars". PhD thesis. Bonn, Germany: University of Bonn. 169 pp.

Martins, F. et al. (June 2013). "Evidence of Quasi-Chemically Homogeneous Evolution of Massive Stars up to Solar Metallicity". In: *Astronomy and Astrophysics* 554, A23. DOI: 10.1051/0004-6361/201321282.

Meynet, G. and A. Maeder (Sept. 2000). "Stellar Evolution with Rotation. V. Changes in All the Outputs of Massive Star Models". In: *Astronomy and Astrophysics* 361, pp. 101–120. ISSN: 0004-6361.

Miller-Jones, James C. A. et al. (Mar. 2021). "Cygnus X-1 Contains a 21-Solar Mass Black Hole—Implications for Massive Star Winds". In: *Science* 371, pp. 1046–1049. DOI: 10.1126/science.abb3363.

Nieuwenhuijzen, H. and C. de Jager (May 1990). "Parametrization of Stellar Rates of Mass Loss as Functions of the Fundamental Stellar Parameters M, L, and R." In: *Astronomy and Astrophysics* 231, pp. 134–136. ISSN: 0004-6361.

Paxton, Bill et al. (Jan. 2011). "Modules for Experiments in Stellar Astrophysics (MESA)". In: *The Astrophysical Journal Supplement Series* 192.1, p. 3. DOI: 10/b42mx4.

Paxton, Bill et al. (Aug. 2013). "Modules for Experiments in Stellar Astrophysics (MESA): Planets, Oscillations, Rotation, and Massive Stars". In: *The Astrophysical Journal Supplement Series* 208.1, p. 4. DOI: 10/gdk28r.

Paxton, Bill et al. (Sept. 2015). "Modules for Experiments in Stellar Astrophysics (MESA): Binaries, Pulsations, and Explosions". In: *The Astrophysical Journal Supplement Series* 220.1, p. 15. DOI: 10/gfsvk5.

Paxton, Bill et al. (Feb. 2018). "Modules for Experiments in Stellar Astrophysics (MESA): Convective Boundaries, Element Diffusion, and Massive Star Explosions". In: *The Astrophysical Journal Supplement Series* 234.2, p. 34. DOI: 10/gfsvnd.

Paxton, Bill et al. (July 2019). "Modules for Experiments in Stellar Astrophysics (MESA): Pulsating Variable Stars, Rotation, Convective Boundaries, and Energy Conservation". In: *The Astrophysical Journal Supplement Series* 243.1, p. 10. DOI: 10/gn8qg3.

Pearson, Karl (July 1900). "On the Criterion That a given System of Deviations from the Probable in the Case of a Correlated System of Variables Is Such That It Can Be Reasonably Supposed to Have Arisen from Random Sampling". In: *The London, Edinburgh, and Dublin Philosophical Magazine and Journal of Science* 50.302, pp. 157–175. DOI: 10.1080/14786440009463897.

Petrovic, J. et al. (May 2005). "Which Massive Stars Are Gamma-Ray Burst Progenitors?" In: *Astronomy and Astrophysics* 435.1, pp. 247–259. DOI: 10/d8kzw3.

Pignatari, M. et al. (Feb. 2010). "The Weak S-Process in Massive Stars and Its Dependence on the Neutron Capture Cross Sections". In: *The Astrophysical Journal* 710, pp. 1557–1577. DOI: 2010020204130300.

Pols, Onno (Sept. 2011). "Stellar Structure and Evolution". Lecture notes. Astronomical Institute, Utrecht University. URL: https://www.astro.ru.nl/~onnop/education/stev_utrecht_notes/.

Ramírez-Agudelo, O. H. et al. (Dec. 2013). "The VLT-FLAMES Tarantula Survey. XII. Rotational Velocities of the Single O-Type Stars". In: *Astronomy and Astrophysics* 560, A29. DOI: 10.1051/0004-6361/201321986.

Ramírez-Agudelo, O. H. et al. (Apr. 2017). "The VLT-FLAMES Tarantula Survey - XXIV. Stellar Properties of the O-Type Giants and Supergiants in 30 Doradus". In: *Astronomy & Astrophysics* 600, A81. DOI: 10.1051/0004-6361/201628914.

Remillard, Ronald A. and Jeffrey E. McClintock (Sept. 2006). "X-Ray Properties of Black-Hole Binaries". In: *Annual Review of Astronomy and Astrophysics* 44, pp. 49–92. DOI: 10.1146/annurev.astro.44.051905.092532.

Russell, Henry Norris (June 1914). "Relations Between the Spectra and Other Characteristics of the Stars". In: *Popular Astronomy* 22, pp. 331–351. ISSN: 0197-7482.

Salpeter, Edwin E. (Jan. 1955). "The Luminosity Function and Stellar Evolution." In: *The Astrophysical Journal* 121, p. 161. DOI: 10/dqrfgf.

Sana, H. et al. (July 2012). "Binary Interaction Dominates the Evolution of Massive Stars". In: *Science* 337.6093, pp. 444–446. DOI: 10.1126/science.1223344. pmid: 22837522.

Sanyal, D. et al. (Aug. 2015). "Massive Main-Sequence Stars Evolving at the Eddington Limit". In: *Astronomy & Astrophysics* 580, A20. DOI: 10.1051/0004-6361/201525945.

Sanyal, D. et al. (Jan. 2017). "Metallicity Dependence of Envelope Inflation in Massive Stars". In: *Astronomy & Astrophysics* 597, A71. DOI: 10/gg7mww.

Simón-Díaz, S. and A. Herrero (Feb. 2014). "The IACOB Project. I. Rotational Velocities in Northern Galactic O- and Early B-Type Stars Revisited. The Impact of Other Sources of Line-Broadening". In: *Astronomy and Astrophysics* 562, A135. DOI: 10/gdk29q.

Simón-Díaz, S. et al. (Aug. 2010). "Observational Evidence for a Correlation between Macroturbulent Broadening and Line-Profile Variations in OB Supergiants". In: *The Astrophysical Journal* 720.2, pp. L174–L178. DOI: 10/dg6w26.

Simón-Díaz, S. et al. (May 2011). "The IACOB Project: Synergies for the Gaia Era". In: *Stellar Clusters & Associations: A RIA Workshop on Gaia*. Stellar Clusters & Associations: A RIA Workshop on Gaia. Granada, Spain, pp. 255–259. arXiv: 1109.2665.

Simón-Díaz, S. et al. (July 2020). "The IACOB Spectroscopic Database. New Interface and Second Data Release". XIV.0 Scientific Meeting (Virtual) of the Spanish Astronomical Society. URL: https://ui.adsabs.harvard.edu/abs/2020sea..confE.187S (visited on 01/17/2022).

Simón-Díaz, Sergio (Apr. 2022a). *Biases in IACOB Sample*. E-mail.

– (Feb. 2022b). *IACOB Data Identifiers*. E-mail.

Spruit, H. C. (Sept. 1999). "Differential Rotation and Magnetic Fields in Stellar Interiors". In: *Astronomy and Astrophysics, v.349, p.189-202 (1999)* 349, p. 189. ISSN: 0004-6361.

– (Jan. 2002). "Dynamo Action by Differential Rotation in a Stably Stratified Stellar Interior". In: *Astronomy and Astrophysics, v.381, p.923-932 (2002)* 381, p. 923. DOI: 10.1051/0004-6361:20011465.

Thielemann, F. -K. et al. (Apr. 2011). "What Are the Astrophysical Sites for the R-Process and the Production of Heavy Elements?" In: *Progress in Particle and Nuclear Physics* 66, pp. 346–353. DOI: 10.1016/j.ppnp.2011.01.032.

Vink, Jorick S. (Sept. 2021). "Theory and Diagnostics of Hot Star Mass Loss". In: *arXiv e-prints*. URL: https://ui.adsabs.harvard.edu/abs/2021arXiv210908164V (visited on 05/09/2022).

Vink, Jorick S. et al. (Oct. 2000). "New Theoretical Mass-Loss Rates of O and B Stars". In: *Astronomy and Astrophysics* 362, pp. 295–309. ISSN: 0004-6361.

– (Apr. 2001). "Mass-Loss Predictions for O and B Stars as a Function of Metallicity". In: *Astronomy and Astrophysics* 369, pp. 574–588. DOI: 10/bv8fj5.

Vink, Jorick S. et al. (July 2011). "Wind Modelling of Very Massive Stars up to 300 Solar Masses". In: *Astronomy and Astrophysics* 531, A132. DOI: 10.1051/0004-6361/201116614.

Webster, B. Louise and Paul Murdin (Jan. 1972). "Cygnus X-1-a Spectroscopic Binary with a Heavy Companion ?" In: *Nature* 235, pp. 37–38. DOI: 10.1038/235037a0.

Yoon, S.-C. and N. Langer (Nov. 2005). "Evolution of Rapidly Rotating Metal-Poor Massive Stars towards Gamma-Ray Bursts". In: *Astronomy and Astrophysics* 443.2, pp. 643–648. DOI: 10/dk38vd.